DISS. ETH NO. 19772

OPTICAL AND THERMAL ANALYSES OF AN AIR-BASED SOLAR TROUGH CONCENTRATING SYSTEM

A dissertation submitted to
ETH ZURICH

for the degree of
Doctor of Sciences

presented by
ROMAN BADER
MSc ETH ME
born June 28, 1983
citizen of Basel (BS)

accepted on the recommendation of
Prof. Dr. Aldo Steinfeld, examiner
Prof. Dr. Robert Pitz-Paal, co-examiner

2011

Abstract

An innovative concept for fabricating solar trough concentrators based on pneumatic polymer mirrors supported on precast concrete frames is presented. The 2-stage version of the concentrator uses circular-cylindrical primary mirrors in tandem with secondary mirrors to correct for optical aberration. An integral method is formulated and solved to derive the optimal secondary mirror shape for maximum solar flux concentration. The 1-stage version of the concentrator avoids the secondary mirrors by using a multilayer polymer mirror membrane to generate a multi-circular primary concentrator profile that approaches the trough parabolic shape. The integral design method is further applied to derive the profiles of trough concentrators that generate a pill-box radiative flux distribution on the target area, suitable for concentrated photovoltaics.

Analytical models of the statics of the membrane mirror construction, including the concrete support structure, are formulated for both 1-stage and 2-stage concentrators, and coupled to a Monte Carlo ray-tracing simulation. The models are experimentally validated with measurements on 45m-long prototype concentrator sections. The validated models are applied for design and optimization purposes, and to elucidate the concentrator's sensitivity to typical manufacturing and operational imperfections, such as reflective surface errors, deformations of the support structure due to gravity forces and tensile forces exerted by the membranes, errors of the mirror membrane widths, and membrane inflation pressure deviations.

The highest measured peak solar flux concentration at the focus of the 2-stage concentrator prototype is 55 (measured at 8.6° solar incidence angle), corresponding to 36% of the predicted value for the ideal concentrator of 151. Performance reducing factors were: 1) flat instead of ideally curved secondary mirrors, 2) average mirror reflectivity of 0.92, 3) attenuation of incoming solar radiation by the transparent envelope by 9 to 19% for solar incidence angles in the range of 0° to 60°, and 4) additional 10% attenuation due to dust on the transparent envelope. Highest measured peak solar flux

concentration at the focus of the 1-stage concentrator prototype is 18.9 (measured at 62.6° solar incidence angle), corresponding to 39% of the predicted value for the ideal concentrator of 47.9. The performance of the 1-stage prototype concentrator is reduced by: 1) transmission and reflection losses (same as in the case of the 2-stage concentrator), 2) errors of the widths of the intalled mirror membranes, and 3) inaccurate inflation pressures applied to the membranes.

A cylindrical cavity-receiver that uses air as the heat transfer fluid (HTF) is proposed for the concentrator. A numerical heat transfer model is developed to determine the receiver's absorption efficiency and pumping power requirement. The 2D energy equation, coupling radiative, convective, and conductive heat transfer is formulated, and solved with finite-volume techniques. The Monte Carlo ray-tracing and radiosity methods are applied to establish the solar radiation distribution and radiative exchange within the receiver. Experimental model validation is accomplished via comparison of measured and simulated receiver and air temperatures. Measurements are taken on a 42m-long full-scale prototype receiver section, installed on the prototype trough concentrator.

The performance of the prototype receiver is predicted with the validated heat transfer model. At summer solstice, solar noon, with HTF inlet temperature of 120°C, and HTF outlet temperature in the range of 250÷450°C, the predicted receiver absorption efficiency ranges from 45% to 29%. One third of the solar radiation incident on the prototype receiver is lost by spillage at the aperture and reflection inside the cavity. Main heat losses from the prototype receiver are by natural convection (9.9÷9.7% of solar power input) and reradiation (6.1÷17.6%) through the open cavity aperture, and by natural convection from the cavity insulation (5.6÷9.1%). The pressure drop in the HTF flow through the receiver is in the range of 4÷206 mbar, resulting in isentropic pumping power requirements of 27W÷16.3kW, corresponding to 0.01%÷5.8% of the solar power input.

Zusammenfassung

Ein innovatives Konzept zur Herstellung von Rinnen-Solarkonzentratoren wird vorgestellt, basierend auf pneumatischen Polymer-Spiegeln, die von Beton-Fertigbauteilgerüsten getragen werden. Die 2-stufige Variante des Konzentrators verwendet kreiszylindrische Primärspiegel in Kombination mit Sekundärspiegeln zur Korrektur der optischen Aberration. Eine Integrationsmethode wird formuliert und gelöst, zur Herleitung der optimalen Sekundärspiegelform für maximale Konzentration des solaren Strahlungsflusses. In der 1-stufigen Variante des Konzentrators werden die Sekundärspiegel vermieden, indem eine mehrschichtige Polymer-Spiegelmembran verwendet wird, welche ein mehrfach kreisförmig gekrümmtes Primärspiegelprofil erzeugt, das der Parabolrinnenform nahe kommt. Die integrale Designmethode wird zudem angewandt, um die Profile von Rinnen-Konzentratoren herzuleiten, welche auf der bestrahlten Oberfläche eine rechteckige Strahlungsflussverteilung erzeugen, geeignet für konzentrierende Photovoltaik.

Analytische Modelle der Statik der Membranspiegelkonstruktion, inklusive Beton-Tragwerk, werden sowohl für den 1-stufigen, wie auch für den 2-stufigen Konzentrator formuliert und mit einer Monte Carlo Strahlverfolgungssimulation verknüpft. Die Modelle werden anhand von Messungen an 45m langen Prototyp-Konzentratorabschnitten experimentell validiert. Die validierten Modelle werden zu Entwicklungs- und Optimierungszwecken verwendet, sowie zur Untersuchung der Empfindlichkeit des Konzentrators auf typische Herstellungs- und Betriebsfehler, wie Spiegeloberflächenfehler, Deformationen des Tragwerks aufgrund von Gravitationskräften und Zugkräften durch die gespannten Membranen, Fehler der Spiegelmembranbreiten und Abweichungen der Membran-Spanndrücke.

Die höchste gemessene Spitzenkonzentration des solaren Strahlungsflusses im Fokus des 2-stufigen Konzentrator-Prototyps beträgt 55, was 36% des berechneten Wertes für den idealen Konzentrator von 151

entsprecht. Folgende Faktoren haben negativen Einfluss auf die Messergebnisse: 1) planare anstelle von ideal gekrümmten Sekundärspiegeln, 2) mittlere Spiegelreflektivität von 0.92, 3) Abschwächung der einfallenden Solarstrahlung durch die transparente Hülle um 9 bis 19% für solare Einfallswinkel im Bereich von 0 bis 60°; and 4) zusätzliche 10% Abschwächung der Solarstrahlung durch Staub auf der transparenten Hülle. Die höchste gemessene Spitzenkonzentration des solaren Strahlungsflusses des 1-stufigen Konzentrator-Prototyps beträgt 18.9 (gemessen bei einem solaren Einfallswinkel von 62.6°), was 39% des berechneten Wertes für den idealen Konzentrator von 47.9 entspricht. Die Messergebnisse für den 1-stufigen Konzentrator- Prototypen werden vermindert durch: 1) Transmissions- und Reflektionsverluste (wie im Fall des 2-stufigen Konzentrators), 2) fehlerhafte Breiten der installierten Spiegelmembranen und 3) Anwendung von fehlerhaften Membran-Spanndrücken.

Ein zylindrischer Hohlraum-Strahlungsempfänger (im Folgenden nur „Empfänger" genannt), welcher Luft als Wärmeübertragungsfluid (HTF) verwendet, wird für den Konzentrator vorgeschlagen. Ein numerisches Wärmeübergangsmodell wird erstellt, um die Absorptionseffizienz und die benötigte Pumpleistung des Empfängers zu bestimmen. Die 2D-Energiegleichung, welche Wärmeübertragung durch Strahlung, Konvektion und Wärmeleitung verknüpft, wird formuliert und mit Finite-Volumen-Methoden gelöst. Die Monte Carlo Strahlverfolgungsmethode und die Radiosity-Methode werden angewandt, um die Verteilung der Solarstrahlung und den Strahlungsaustausch im Empfänger zu ermitteln. Experimentelle Modellvalidierung erfolgt durch Vergleich gemessener und simulierter Empfänger- und Lufttemperaturen. Messungen werden an einem 42m-langen original-massstäblichen Prototyp-Empfänger vorgenommen, welcher auf dem Rinnen-Konzentrator-Prototypen installiert ist.

Die Effizienz des Prototyp-Empfängers wird mittels validierten Wärmeübergangsmodells berechnet. Zur Sommersonnenwende, mit der Sonne im Zenith, mit 120°C HTF-Eingangstemperatur und mit HTF-Ausgangstemperatur im Bereich 250÷450°C, liegt die berechnete Absorptionseffizienz des Empfängers zwischen 45% und 29%. Ein Drittel

der auf den Empfänger einfallenden Solarstrahlung verfehlt die Empfänger-Öffnung, oder geht durch Reflexionen im Empfänger verloren. Die grössten Wärmeverluste des Empfängers entstehen durch natürliche Konvektion (9.9÷9.7% der einfallenden Solarenergie) und Rückstrahlung (6.1÷17.6%) durch die Hohlraum-Öffnung, sowie durch natürliche Konvektion an der Hohlraum-Isolation (5.6÷9.1%). Der Druckverlust in der HTF-Strömung durch den Empfänger liegt im Bereich 4÷206mbar und erfordert eine isentrope Pumpleistung von 27W÷16.3kW, was 0.01%÷5.8% der einfallenden Solarenergie entspricht.

Acknowledgments

I'd like to thank Prof. Aldo Steinfeld for entrusting me with this interesting project and for supervising my thesis. I thank Prof. Robert Pitz-Paal for acting as co-examiner.

Contents

Nomenclature

Latin characters

A	area $\left[\mathrm{m}^2\right]$
A_b	absorptance
dA	surface segment area $\left[\mathrm{m}^2\right]$
a	coefficient
C	solar flux concentration ratio
ΔC_{mean}	mean relative difference of C-distributions $\left[\%\right]$
c	coefficient; placeholder for A_b, E_m, R_e, T_r; specific heat $\left[\mathrm{J}/(\mathrm{kg}\cdot\mathrm{K})\right]$
$c_{\mathrm{meas.,sim.}}$	standard covariance coefficient of C-distributions
c_p	specific heat at constant pressure $\left[\mathrm{J}/(\mathrm{kg}\cdot\mathrm{K})\right]$
D	diameter $\left[\mathrm{m}\right]$
DNI	direct normal solar irradiance $\left[\mathrm{W}/\mathrm{m}^2\right]$
d	thickness $\left[\mathrm{m}\right]$
E	Young's modulus $\left[\mathrm{W}/\mathrm{m}^2\right]$
E_m	emittance
e	surface roughness $\left[\mathrm{m}\right]$
$\hat{\boldsymbol{e}}_{M_{\mathrm{bending}}}$	directional unit vector of bending moment, $\hat{\boldsymbol{e}}_{M_{\mathrm{bending}}} = \left(e_{M_{\mathrm{bending}},2}, e_{M_{\mathrm{bending}},3}\right)$
$e_{\lambda b}$	blackbody spectral emissive power $\left[\mathrm{W}/\mathrm{m}\right]$
F	point on focal line, $F = \left(F_x, F_y, f\right)$ $\left[\mathrm{m}\right]$; force (scalar) $\left[\mathrm{N}\right]$
$\boldsymbol{F}$	force (vector), $\boldsymbol{F} = \left(F_x, F_y, F_z\right)$ $\left[\mathrm{N}\right]$
F'	force per unit of concentrator length (scalar) $\left[\mathrm{N}/\mathrm{m}\right]$
$\boldsymbol{F}'$	force per unit of concentrator length (vector), $\boldsymbol{F}' = \left(F_x', F_y, F_z'\right)$ $\left[\mathrm{N}/\mathrm{m}\right]$
$F_{0-\lambda}$	fractional function
F_{k-i}	view factor
f	focal length $\left[\mathrm{m}\right]$; probability density function $\left[1/\mathrm{deg}\right]$
f_{Moody}	Moody friction factor
G	center of gravity $\left[\mathrm{m}\right]$
g	gravitation constant, $9.81 \mathrm{\ m/s}^2$
$\hat{\boldsymbol{g}}$	direction vector of gravitational force
h	convective heat transfer coefficient $\left[\mathrm{W}/(\mathrm{m}^2\cdot\mathrm{K})\right]$

I	geometrical moment of inertia $\left[\mathrm{m}^4\right]$
i, j	indexes
$\hat{\boldsymbol{i}}, \hat{\boldsymbol{j}}, \hat{\boldsymbol{k}}$	unit vectors in x, y, z-directions
K	pressure loss coefficient
k	thermal conductivity $\left[\mathrm{W}/(\mathrm{m}\cdot\mathrm{K})\right]$; scaling function $\left[\mathrm{m}\right]$; index
l	length $\left[\mathrm{m}\right]$
l_{girder}	length of longitudinal beam section $\left[\mathrm{m}\right]$
$\boldsymbol{M}$	moment, $\boldsymbol{M} = \left(M_x, M_y, M_z\right)$ $\left[\mathrm{Nm}\right]$
M	molar weight $\left[\mathrm{kg/mol}\right]$
$m_{\mathrm{<subscript>}}$	number
m_{HTF}	HTF mass flow rate $\left[\mathrm{kg/s}\right]$
m_i	slope of arc-spline at node i
N	number
$\boldsymbol{N}$	prestressing force $\left[\mathrm{N}\right]$
Nu	Nusselt number
n	refractive index
$\hat{\boldsymbol{n}}$	unit normal vector
$n_{\mathrm{<subscript>}}$	number
n_{arc}	number of arcs/membranes per arc-spline
O	center point, $O = \left(O_x, O_y, O_z\right)$ $\left[\mathrm{m}\right]$
P	point $\left[\mathrm{m}\right]$; perimeter $\left[\mathrm{m}\right]$
$P_{0,i}$	center point of arc i of arc-spline, $P_{0,i} = \left(x_{0,i}, z_{0,i}\right)$ $\left[\mathrm{m}\right]$
$P_{0,S,j}$	center point of suspended section S_j, $P_{0,S,j} = \left(x_{0,S,j}, z_{0,S,j}\right)$ $\left[\mathrm{m}\right]$
$P_{1,j}$	support membrane inner clamping point, $P_{1,j} = \left(x_{1,j}, z_{1,j}\right)$ $\left[\mathrm{m}\right]$
P_{AS}	point on arc-spline surface, $P_{\mathrm{AS}} = \left(x_{\mathrm{AS}}, y_{\mathrm{AS}}, z_{\mathrm{AS}}\right)$ $\left[\mathrm{m}\right]$
P_i	node i of arc-spline, $P_i = \left(x_i, z_i\right)$ $\left[\mathrm{m}\right]$
P_{parabola}	point on parabolic surface, $P_{\mathrm{parabola}} = \left(x_{\mathrm{parabola}}, y_{\mathrm{parabola}}, z_{\mathrm{parabola}}\right)$ $\left[\mathrm{m}\right]$
Pe	Péclet number
$\boldsymbol{P}_{\mathrm{i}}\boldsymbol{P}_{\mathrm{o}}$	vector $P_{\mathrm{o}} - P_{\mathrm{i}}$ $\left[\mathrm{m}\right]$
Pr	Prandtl number
p	pressure $\left[\mathrm{Pa}\right]$
p_i	membrane pressure $\left[\mathrm{Pa}\right]$
p_i^{design}	design membrane pressure $\left[\mathrm{Pa}\right]$

$\Delta p_{\mathrm{arc},i}$	pressure difference over arc i of arc-spline $[\mathrm{Pa}]$
Δp_{HTF}	HTF pressure drop in receiver $[\mathrm{Pa}]$
Δp_i	pressure difference over mirror membrane i $[\mathrm{Pa}]$
$\Delta p_{\mathrm{rms},1}$	rms-difference between calculated and prescribed membrane pressures $[\mathrm{Pa}]$
$\Delta p_{\mathrm{rms},2}$	rms-difference between calculated and measured membrane pressures $[\mathrm{Pa}]$
δp	deviation of membrane pressure from design value $[\mathrm{Pa}]$
Q_{HTF}	heat gain by HTF $[\mathrm{W}]$
Q_{loss}	heat loss from receiver $[\mathrm{W}]$
Q_{min}	minimization criterion
Q_{solar}	solar radiation incident on receiver $[\mathrm{W}]$
ΔQ	relative difference of incident radiative power $[\%]$
q	energy flux $\left[\mathrm{W/m^2}\right]$; scaling factor $[\mathrm{m}]$
R	radius $[\mathrm{m}]$; point on reflector profile, $R = \left(R_x, R_y\right)$ $[\mathrm{m}]$
$\Re$	random number $\in [0,1]$
R_e	reflectance
$R_{\mathrm{HTF\,(air)}}$	specific gas constant of HTF (air) $\left[\mathrm{J/(kg \cdot K)}\right]$
R_i	radius of arc i of arc-spline $[\mathrm{m}]$
$R_{S,j}$	radius of section S_j $[\mathrm{m}]$
$\Delta R_{\mathrm{absorber}}$	absorber radius change at interconnections, $[\mathrm{mm}]$
Ra	Rayleigh number
Re	Reynolds number
r	radial coordinate $[\mathrm{m}]$
$\hat{\boldsymbol{r}}$	ray direction unit vector
Δr	radial mesh size $[\mathrm{m}]$
S	point on secondary reflector, $S = \left(S_x, S_y\right)$ $[\mathrm{m}]$
S_j	suspended section of support membrane j, $S_j = \left(x_{S,j}, y_{S,j}, z_{S,j}\right)$ $[\mathrm{m}]$
T	temperature $[\mathrm{K}]$; point on target area, $T = \left(T_x, T_y\right)$ $[\mathrm{m}]$
T_r	transmittance
T_{sky}	apparent sky temperature $[\mathrm{K}]$
ΔT_{HTF}	temperature change between receiver inlet and outlet $[\mathrm{K}]$
t	time $[\mathrm{s}]$
$\boldsymbol{t}$	tangential vector $[\mathrm{m}]$
U	mean flow velocity $[\mathrm{m/s}]$; uniformity
U_{receiver}	inner energy of receiver solid domains $[\mathrm{J}]$

u	local flow velocity [m/s]
$\boldsymbol{u}$	displacement vector of longitudinal beams $[\mathrm{m}]$
u^*	friction velocity [m/s]
V	volume flow rate $\left[\mathrm{m}^3/\mathrm{h}\right]$
v	specific volume $\left[\mathrm{m}^3/\mathrm{kg}\right]$
$\boldsymbol{v}$	set of free arc-spline parameters
W	mechanical power $[\mathrm{W}]$
w	width $[\mathrm{m}]$
$w_{\mathrm{membrane}}^{\mathrm{nominal}}$	membrane width in operation $[\mathrm{m}]$
$w_{\mathrm{membrane}}^{\mathrm{nominal,design}}$	design value for membrane width in operation ..
$w_{\mathrm{membrane}}^{\mathrm{reference}}$	non-stretched membrane width at reference conditions $[\mathrm{m}]$
$w_{\mathrm{membrane}}^{\mathrm{reference,design}}$	design value for non-stretched membrane width at reference conditions $[\mathrm{m}]$
w_{ray}	weighting function; energy per ray bundle $[\mathrm{W}]$
$w_{z/\alpha}$	weighting factors of z - / α - differences
Δw	deviation of membrane width from design value $[\mathrm{m}]$
$\Delta w_{\mathrm{rms,1}}$	rms-difference between calculated and prescribed membrane widths $[\mathrm{m}]$
$\Delta w_{\mathrm{rms,2}}$	rms-difference between calculated and average calculated membrane widths $[\mathrm{m}]$
x, y, z	Cartesian coordinates
x_2, x_3	principal directions of girder profile
x_{steam}	molar fraction of steam
Δx	incremental distance in x -direction $[\mathrm{m}]$
y^*	dummy variable $[\mathrm{m}]$
Z	compressibility factor
$\Delta z_{\mathrm{AS,rms}}$	rms- z -difference between calculated and measured arc-spline $[\mathrm{m}]$
Δz_{max}	maximum z -difference between arc-spline and parabola $[\mathrm{m}]$
Δz_{rms}	rms- z -difference between arc-spline and parabola $[\mathrm{m}]$

Greek characters

α	slope angle $[\mathrm{rad}]$; absorption coefficient $[1/\mathrm{m}]$; thermal diffusivity $\left[\mathrm{m}^2/\mathrm{s}\right]$; angular coordinate $[\mathrm{rad}]$
$\Delta\alpha_{\mathrm{max}}$	maximum α -difference between arc-spline and parabola $[\mathrm{rad}]$

$\Delta\alpha_{rms}$	rms-α-difference between arc-spline and parabola $[\text{rad}]$
β	volumetric thermal expansion coefficient $[\text{1/K}]$
$\beta_{inclination}$	concentrator tilt angle $[\text{deg}]$
δ	ray directional error at CPC inlet
δ_{ki}	Kronecker delta
ε	eccentricity $[\text{m}]$; emissivity
ε_{th}	thermal membrane expansion
$\Delta\varepsilon_{th}$	membrane's thermal expansion coefficient $[\text{m}/(\text{m}\cdot\text{K})]$
ε_φ	hygroscopic membrane expansion
$\Delta\varepsilon_\varphi$	membrane's hygroscopic expansion coefficient $[\text{m}/(\text{m}\cdot\%)]$
ϕ_{rim}	rim angle $[\text{deg}]$
φ	angular coordinate $[\text{rad}]$; relative humidity $[\%]$
γ	intercept factor: fraction of rays intercepted by target
η	efficiency
$\eta_{absorption}$	receiver absorption efficiency
κ	specific heat ratio; extinction coefficient
λ	wavelength $[\text{m}]$
μ	dynamic viscosity $[\text{Pa}\cdot\text{s}]$
ν	kinematic viscosity $[\text{m}^2/\text{s}]$
θ	incidence angle $[\text{rad}]$
θ_{skew}	solar incidence angle on concentrator aperture $[\text{deg}]$
θ_{sun}	solid angle subtended by incident solar radiation, $\theta_{sun}=6.72\cdot10^{-5}$ sr
$\Delta\theta$	circumferential mesh size $[\text{rad}]$
ρ	reflectivity; density $[\text{kg/m}^3]$
σ	mode of Bivariate Chi Squared error distribution $[\text{mrad}]$; standard deviation of C; Stefan-Boltzmann constant $[\text{W}/(\text{m}^2\cdot\text{K}^4)]$
τ	transmissivity
ζ	integration boundary $[\text{deg}]$
ζ^*	integration variable $[\text{deg}]$

Superscript

d	diffuse
s	specular
sat	saturated

$\dots'$	derivative; per unit length; directional
$\overline{\dots}$	average

Subscripts

1,2,…	surface number
a	annulus
ave	average
i	in
in	inlet
inc	incident
m	measurement
max	maximum
n	normal
o	out
out	outlet
p	pump
r	reflected
s	simulation; isentropic
w	window
λ	spectral
∞	ambient

Abbreviations

AM	air mass
AS	arc-spline
CFD	computational fluid dynamics
CPC	compound parabolic concentrator
CPV	concentrated photovoltaics
CSP	concentrated solar power
CSR	circumsolar ratio $[\%]$
CV	control volume
ETFE	Ethylene tetrafluoroethylene
FS	full scale value
HTF	heat transfer fluid
LEC	levelized electricity costs

MC	Monte Carlo
max	maximum
PM	primary mirror
ROI	region of interest
rms	root-mean-square
SEGS	Solar Electric Generating Station
SM	secondary mirror
TC	thermocouple

1 Introduction

Concentrated solar thermal power generation (CSP) is a promising technology for cheap large-scale renewable electricity production with minimal negative impacts (greenhouse gas emissions, land use, hazard, noise, toxic waste) on present or future life on Earth. Electricity is a high-value form of energy that can fuel most devices. Exceptions are private means of transportation, for which solar fuels are expected to become a more practicable source of clean energy. In contrast to electricity produced by photovoltaics, with CSP it is possible to store large amounts of solar energy in the intermediate form of heat. Hence, CSP not only offers the possibility of supplying constant (24/7) base-load electricity, but also of covering the peaks in the demand curve, thereby greatly enhancing the value of the produced electricity.

Today, parabolic trough power plants are the most mature CSP technology. The first commercial parabolic trough plant, the Solar Electric Generating Station I (SEGS I) in the Californian Mojave Desert, started operation in 1984. By 1990, another 8 SEGS plants were completed, reaching the total of 354MW$_{el}$ of installed capacity. All 9 SEGS plants are still operational to date. Currently, parabolic trough power plants with a total capacity of 1.2GW$_{el}$ are operational worldwide, with plant sizes ranging from 1MW$_{el}$ (Saguaro Power Plant) to 80MW$_{el}$ (SEGS VIII and IX). Another 1.2GW$_{el}$ of capacity are under construction, and 2.7GW$_{el}$ of capacity are under development, with plant sizes ranging from 50MW$_{el}$ to 1GW$_{el}$ (Blythe Solar Power Project). Most of these plants are (or will be) located in the Southwestern USA (California, Arizona, Nevada), Florida, Spain, and the MENA region (UAE, Morocco, Algeria, Egypt).

Today's parabolic trough power plants use back-surface coated glass mirrors, supported by steel trusses to focus solar radiation onto the receiver. The receiver consists of a stainless steel absorber pipe and uses a thermo-oil (e.g. Therminol VP-1) as the heat transfer fluid (HTF), which limits the receiver operating temperature to about 400°C. [1] A cermet selective

surface coating on the absorber provides high solar absorptivity (>95%) and low infrared emissivity (<10% at 400°C surface temperature). [2] The absorber is surrounded by a glass tube that features antireflective coatings on both surfaces (solar transmittance >96%), with a vacuum (<0.1Pa) in the annulus to minimize convective heat losses. The vacuum-tight enclosure requires glass-to-metal seals and bellows, to account for differing thermal expansion of the glass and steel tubes. To maintain the vacuum, metallic plates ("getters") are employed inside the vacuum annulus, which remove gas molecules (mainly hydrogen) that separate from the HTF and diffuse through the absorber pipe wall into the vacuum. [3]

Beside mass production and plant scale-up, further reductions of the levelized electricity costs (LEC) of parabolic trough power plants are to be achieved through the use of cheaper components and higher plant efficiency. The solar field constitutes 30% of the total investment costs of parabolic trough power plants (Figure 1-1). Hence the use of cheaper mirror support structures, mirror materials, and receivers could have a large impact on the overall plant costs, and consequently on the LEC. Higher plant efficiency is achievable by increasing the top temperature of the steam turbine power cycle, which requires heat transfer fluids that can be heated to above 500°C.

In this thesis, a novel solar trough concentrating system for CSP is investigated. The concentrator is based on pneumatic polymer membrane mirrors, mounted on precast concrete frames. Its major advantages are fourfold: 1) the concrete structure is more durable, rigid, and stronger than a conventional metallic frame; 2) wind induced vibrations are eliminated; 3) small structural deformations and continuous mirror alignment by differential pressure control allow for aperture widths of up to 10m; and 4) self-cleaning, scratch-resistant, and UV-resistant transparent ETFE-envelopes can be applied to protect the high-quality mirror membranes from soiling. Furthermore, preliminary economic analyses indicate the potential of lower costs per square meter, as cheaper and less structural materials are employed, the inflatable polymer membranes are easily transported in rolls, and the concrete frames are cast on site.
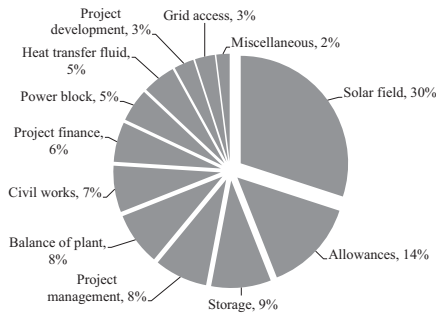
Figure 1-1: Investment cost splitting of a 50MW$_{el}$ parabolic trough plant with 7h storage. [4]

Pneumatically spanned membrane mirrors for solar concentrators have been used before for solar dishes [5] and for heliostats [6], and are currently being investigated by [7] for solar trough concentrators. Concrete structures have been used for heliostats by [8].

The concentrator focuses direct sunlight onto a cylindrical cavity-receiver that uses air as the heat transfer fluid (HTF). Air has many advantages over other HTFs that have hitherto been considered (e.g. thermo-oil, molten salt, water/steam): i) no costs, ii) no relevant operating temperature constraints, iii) no HTF degradation, iv) non-corrosive, v) non-toxic, vi) near-ambient operating pressure, avoiding leakage concerns and allowing for thin duct walls, and vii) direct heating of a packed-bed thermal storage [9], eliminating the need for a heat exchanger between HTF and thermal storage medium. On the other hand, when the heat transfer fluid (HTF) has low volumetric heat capacity and thermal conductivity, as it is usually the case for gases, large HTF volume flow rate and receiver heat transfer area are needed, which may translate into excessive pressure drops and concomitant energy penalties. Therefore, cavity-receivers are an interesting alternative to conventional receivers when air is used as the HTF, as they allow for larger flow cross-section, and larger and more uniformly irradiated heat transfer area. Cavity-receivers further enable the application of CPC secondary concentrators, which increase the solar flux

3

concentration at the target area up to 4 times compared to existing receivers, thus minimizing the area for reradiation losses – the dominant mode of heat loss from the receiver. Finally, by using common materials of construction and avoiding cost drivers like surface coatings, vacuum insulation jackets, and getters, cavity-receivers promise substantial fabrication cost reductions per unit receiver length compared to conventional receivers. Cylindrical cavity-receivers have been proposed previously for an annular flow absorber [10], and to enclose a single absorber tube or an array of absorber tubes [11]-[13].

Chapters 2 and 3 describe the design, modeling, testing, and performance results of two different versions of the proposed concentrator for CSP. Alternatively, the concentrator can be adapted for the use with photovoltaic cells instead of the thermal receiver. For this reason, the shapes of 1-stage and 2-stage trough concentrators suitable for concentrated photovoltaics are derived and analysed in chapter 4. Chapter 5 describes the receiver design, the receiver heat transfer model, and performance predictions obtained with the model. Chapter 6 documents the design, testing, and modeling of a prototype cavity-receiver, the experimental heat transfer model validation, and performance predictions for the prototype receiver, obtained with the validated model.

2   Two-Stage Solar Trough Concentrator[1]

2.1   Concept

Figure 2-1 depicts the conceptual design. By applying a few millibar overpressure over an inflatable elastic enclosure, two opposing cylindrical curved surfaces are obtained, encompassing a transparent foil on one side and a silicone coated fiberglass fabric with an aluminized mirror sheet on the other side. These gas-tight polymer membranes are supported on their edges with a simple precast and prestressed concrete frame of rectangular shape. A 49.4 m-long, 7.9 m-wide prototype has been fabricated and is shown in Figure 2-2, as installed perpendicularly to the meridian in Biasca, Switzerland. The four aforementioned advantages have been corroborated with this prototype. The major drawback, however, concerns the optics. The cylindrically-shaped concentrating mirrors suffer from optical aberration, which reduces the achievable solar flux concentration. Figure 2-3 shows the path of sun rays after reflection on perfect parabolic and circular trough concentrators. To correct for this optical imperfection of the image, a tailor-made secondary specular reflector is incorporated in tandem with the primary cylindrical mirror, as schematically shown in Figure 2-1. The target is a tubular solar receiver carrying the heat transfer medium, which is positioned at the focal plane of the combined primary and secondary mirrors. The secondary reflector is designed for maximum solar concentration ratio at the target plane. The Monte Carlo (MC) ray-tracing methodology is applied and experimentally validated by measuring the performance of the sun-tracking prototype system.
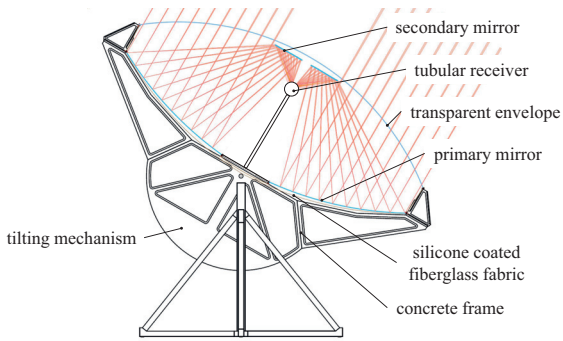

Figure 2-1: Conceptual design of the 2-stage solar trough concentrator based on pneumatic polymer mirrors supported on precast concrete frames (source: Airlight Energy SA).
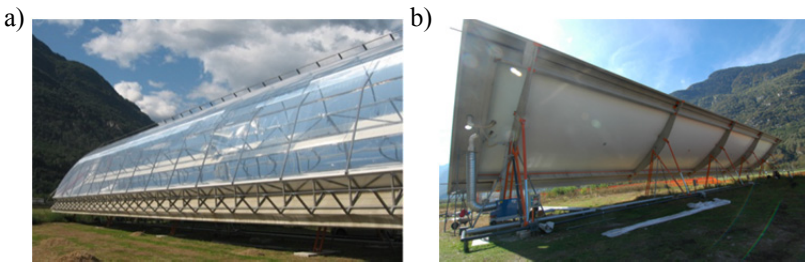

Figure 2-2: Photograph of the 49.4 m-long 7.9 m-wide sun-tracking 2-stage solar trough concentrator prototype: a) front view; b) rear view.
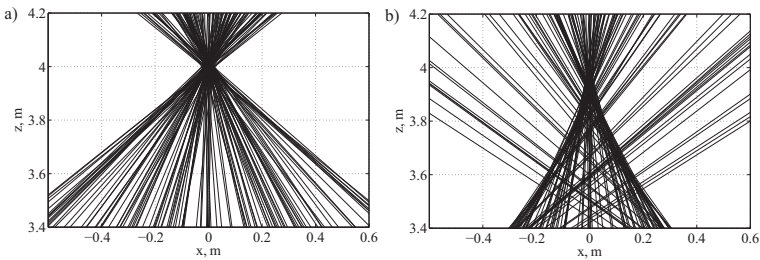

Figure 2-3: Ray paths after reflection on a) perfect parabolic trough concentrator, and b) perfect circular trough concentrator; parameters: w_{PM} =8m, ϕ_{rim} =53.1°.

2.2 Optical Analysis

Figure 2-4 shows a perspective view of the optical components of the solar concentrator system, comprising two symmetric primary trough mirrors, denoted as *PM*, and two symmetric secondary mirrors, denoted as *SM*, on-axis with *PM*. Indicated is the target area that matches the tubular solar receiver. The y-z-plane is the plane of symmetry. Both *PM* and *SM* are enclosed by a transparent cylindrical envelope. The *PM* profile consists of a sector of a circle of radius R_{PM} and center O_{PM} at a distance 0.44 m from the z-axis; i.e., each branch of *PM* is slightly tilted toward the z-axis to reduce the height of the system. The rim angle of *PM* is defined as: [14]

$$\phi_{\mathrm{rim}} = \tan^{-1}\left(\frac{8\left(R_{PM}/2w_{PM}\right)}{16\left(R_{PM}/2w_{PM}\right)^2 - 1}\right), \tag{2.1}$$

by setting for the focal length $f = R_{PM}/2$. The mechanical structure of the system, shown in the photograph of Figure 2-2b, consists of two longitudinal beams supported by five equally distanced transversal beams. Due to their own weight, the longitudinal beams bend, which in turn leads to a variation of the magnitude of R_{PM} and of the location of O_{PM}.
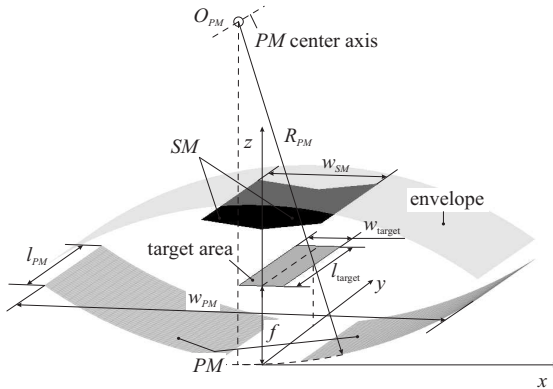

Figure 2-4: Optical components of the solar concentrator system comprising two symmetric primary trough mirrors, denoted *PM*, and two symmetric secondary mirrors, denoted *SM*, on-axis with *PM*. Indicated is the target area of width w_{target} and length l_{target} that matches the tubular solar receiver, at $z = f$.

The forces and moments acting on the beam section are shown in Figure 2-5 and Figure 2-6. G denotes the center of gravity of the beam profile, $\boldsymbol{F}_{\text{gravitation}}$ the gravitational force, and $\beta_{\text{inclination}}$ the concentrator tilt angle. The mechanical strains are assumed to be identical in each of the four longitudinal sections. The beam section is clamped at the ends and the gravitational force is uniformly distributed along its length.
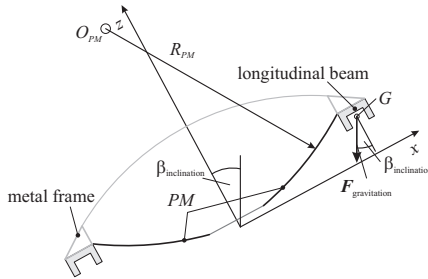

Figure 2-5: Scheme of PM mounted on the two longitudinal beams.
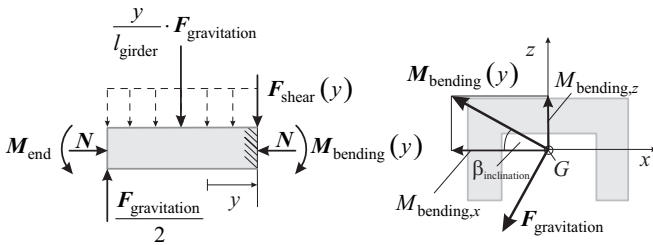
Figure 2-6: a) Forces and moments acting on one of the prestressed beam sections, cut free at y; b) gravitational force acting on the longitudinal beam and resulting bending moment; $\beta_{\text{inclination}}$: concentrator slope.

Using the Cartesian system of coordinates as indicated in Figure 2-6 ($\hat{\boldsymbol{i}}$, $\hat{\boldsymbol{j}}$, and $\hat{\boldsymbol{k}}$ are unit vectors in x-, y-, and z-directions, respectively), the bending moment at position y along one of the PM sections is:

$$M_{\text{bending}}(y) = \left(\left| M_{\text{end}} \right| + \frac{\left| F_{\text{gravitation}} \right| y^2}{2l_{\text{girder}}} - \frac{\left| F_{\text{gravitation}} \right| y}{2} \right) \cdots$$
$$\left(-\cos \beta_{\text{inclination}} \cdot \hat{\boldsymbol{i}} + \sin \beta_{\text{inclination}} \cdot \hat{\boldsymbol{k}} \right) \tag{2.2}$$

The differential equations for the displacements of the beam in x- and z-directions are, respectively:

$$u_x''(y) = -\frac{M_{\text{bending},z}(y)}{EI_z} \tag{2.3}$$

$$u_z''(y) = \frac{M_{\text{bending},x}(y)}{EI_x} \tag{2.4}$$

with boundary conditions:

$$y = 0: \ u_x = u_x' = u_z = u_z' = 0 \tag{2.5}$$

$$y = l_{\text{girder}}/2: \ u_x' = u_z' = 0 \tag{2.6}$$

Integration yields the displacements of the longitudinal beams within one *PM* section,

$$u_x(y) = -\frac{\left| F_{\text{gravitation}} \right|}{24 l_{\text{girder}} EI_z} y^2 \left(l_{\text{girder}} - y \right)^2 \cdot \sin \beta_{\text{inclination}} \tag{2.7}$$

$$u_z(y) = -\frac{\left| F_{\text{gravitation}} \right|}{24 l_{\text{girder}} EI_x} y^2 \left(l_{\text{girder}} - y \right)^2 \cdot \cos \beta_{\text{inclination}} \tag{2.8}$$

with maximum beam displacements:

$$u_{x,\max} = \left| u_x \left(y = l_{\text{girder}}/2, \beta_{\text{inclination}} = 90° \right) \right| \tag{2.9}$$

$$u_{z,\max} = \left| u_z \left(y = l_{\text{girder}}/2, \beta_{\text{inclination}} = 0° \right) \right| \tag{2.10}$$

and maximum total beam deformation:

$$\left| \boldsymbol{u}_{\max} \right| = \left| \boldsymbol{u} \left(y = l_{\text{girder}}/2 \right) \right| = \left(\left(u_{x,\max} \sin \beta_{\text{inclination}} \right)^2 + \left(u_{z,\max} \cos \beta_{\text{inclination}} \right)^2 \right)^{1/2} \tag{2.11}$$

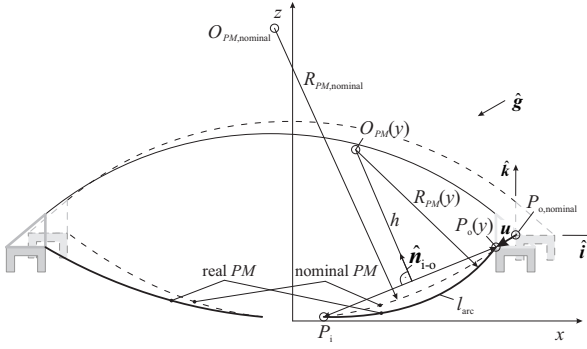The influence of this beam deformation on the *PM* profile is illustrated in Figure 2-7.

Figure 2-7: Variation of *PM* as a consequence of the deformation of the longitudinal beams caused by gravitational forces; the dashed lines indicate the undistorted system and $\hat{g}$ indicates the direction of gravitation.

Point P_o is translated by $\boldsymbol{u} = u_x \cdot \hat{\boldsymbol{i}} + u_z \cdot \hat{\boldsymbol{k}}$, while point P_i is assumed to be fixed. Hence, the distance between inner and outer clamping points P_i and P_o is reduced on the right side and increased on the left side, leading to variations of the mirror radii and, consequently, of their focal lengths. The variation of $R_{PM}(y)$ along y is found from the implicit equation:

$$l_{arc} = 2R_{PM}(y)\sin^{-1}\left(\frac{|\boldsymbol{P_i P_o}(y)|}{2R_{PM}(y)}\right) \tag{2.12}$$

where the arc length l_{arc} is constant along y; $\boldsymbol{P_o P_i}$ is the vector from points P_i to P_o. For $|\boldsymbol{u}_{max}| = 5\text{mm}$ (at $\beta_{inclination} = 30°$), R_{PM} changes by 6%, and the focal length is proportional to R_{PM}. The center point of the right *PM* profile at position y is found from:

$$O_{PM}(y) = P_i + \frac{1}{2}\boldsymbol{P_i P_o}(y) + h(y)\cdot\hat{\boldsymbol{n}}_{i\text{-}o}(y) \tag{2.13}$$

where

$$h(y) = \sqrt{R_{PM}^2(y) - \left(|\boldsymbol{P_i P_o}(y)|/2\right)^2}, \tag{2.14}$$

and $\hat{\boldsymbol{n}}_{i\text{-}o}$ is perpendicular to the direction of $\boldsymbol{P_i P_o}$ (Figure 2-7).

10

The *SM* profile is derived in the analysis that follows. Since it is invariant along *y,* it can be formulated in 2D. *SM* is designed to correct the optical aberration by directing sunrays – incident parallel to the y-z-plane and reflected on the ideal (undistorted) *PM* – onto the focal line described by $F + q \cdot \hat{\boldsymbol{j}}$, with $F = (0, 0, f)$. The situation is shown in Figure 2-8. The nominal *PM* profile (right-side wing, with symmetry axis z) is given by:

$$PM(\varphi) = \begin{pmatrix} O_{PM,x} \\ R_{PM} \end{pmatrix} + R_{PM} \begin{pmatrix} \sin\varphi \\ -\cos\varphi \end{pmatrix} \qquad (2.15)$$

where $O_{PM} = (O_{PM,x}, R_{PM})$ is the right *PM* profile center point. The right-side *SM* profile can be described by:

$$SM(\varphi) = PM(\varphi) + k(\varphi) \cdot \hat{\boldsymbol{r}}_{r,PM} \qquad (2.16)$$

where

$$\hat{\boldsymbol{r}}_{r,PM} = \begin{pmatrix} -\sin 2\varphi \\ \cos 2\varphi \end{pmatrix} \qquad (2.17)$$
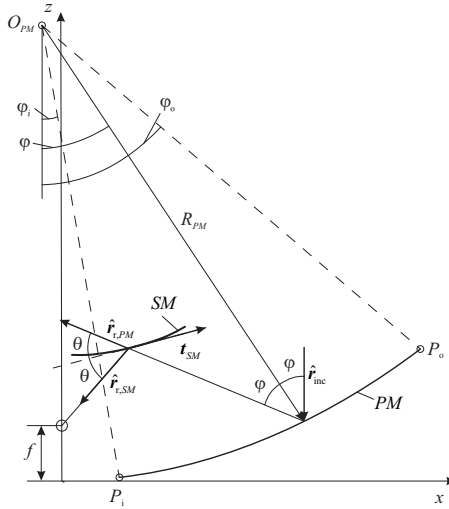

Figure 2-8: Derivation of *SM* designed to correct the optical aberration by directing sunrays $(\hat{\boldsymbol{r}}_{inc})$ that are reflected by the circular-cylindrical *PM* onto the focal line parallel to the y-axis, described by $F + q \cdot \hat{\boldsymbol{j}}$.

is the vector along the direction of the sunray after specular reflection on PM, and $k(\varphi)$ is yet to be determined. The tangential vector on SM is:

$$\boldsymbol{t}_{SM}(\varphi) = \frac{d(SM)}{d\varphi} = R_{PM}\begin{pmatrix}\cos\varphi \\ \sin\varphi\end{pmatrix} + \frac{dk}{d\varphi}\begin{pmatrix}-\sin 2\varphi \\ \cos 2\varphi\end{pmatrix} - 2k\begin{pmatrix}\cos 2\varphi \\ \sin 2\varphi\end{pmatrix} \quad (2.18)$$

and the vector along the direction of the sunray after specular reflection on SM is:

$$\hat{\boldsymbol{r}}_{\mathrm{r},SM} = \frac{F - SM}{|F - SM|} \quad (2.19)$$

The condition for specular reflection is fulfilled when:

$$\boldsymbol{t}_{SM} \cdot \hat{\boldsymbol{r}}_{\mathrm{r},PM} = \boldsymbol{t}_{SM} \cdot \hat{\boldsymbol{r}}_{\mathrm{r},SM} \quad (2.20)$$

Inserting Eqs. (2.17) to (2.19) into Eq. (2.20) yields:

$$\boldsymbol{t}_{SM} \cdot \hat{\boldsymbol{r}}_{\mathrm{r},PM} = -R_{PM}\sin\varphi + \frac{dk}{d\varphi} \quad (2.21)$$

and:

$$\boldsymbol{t}_{SM} \cdot \hat{\boldsymbol{r}}_{\mathrm{r},SM} = \left[R_{PM}\begin{pmatrix}\cos\varphi \\ \sin\varphi\end{pmatrix} + \frac{dk}{d\varphi}\begin{pmatrix}-\sin 2\varphi \\ \cos 2\varphi\end{pmatrix} - 2k\begin{pmatrix}\cos 2\varphi \\ \sin 2\varphi\end{pmatrix}\right]\dots$$
$$\dots \frac{1}{|F - SM|}\left[\begin{pmatrix}0 \\ F_z\end{pmatrix} - \begin{pmatrix}O_{PM,x} \\ R_{PM}\end{pmatrix} - R_{PM}\begin{pmatrix}\sin\varphi \\ -\cos\varphi\end{pmatrix} - k\begin{pmatrix}-\sin 2\varphi \\ \cos 2\varphi\end{pmatrix}\right] \quad (2.22)$$

Solving (2.22) for $dk/d\varphi$ yields (sin and cos abbreviated by s and c):

$$\frac{dk}{d\varphi} = \frac{R_{PM}\,\mathrm{s}\varphi|F - SM| + (R_{PM}\,\mathrm{c}\varphi - 2k\,\mathrm{c}2\varphi)(-O_{PM,x} - R_{PM}\,\mathrm{s}\varphi + k\,\mathrm{s}2\varphi)}{|F - SM| + \mathrm{s}2\varphi(-O_{PM,x} - R_{PM}\,\mathrm{s}\varphi + k\,\mathrm{s}2\varphi)}\dots$$
$$\dots \frac{+(R_{PM}\,\mathrm{s}\varphi - 2k\,\mathrm{s}2\varphi)(F_z + R_{PM}(\mathrm{c}\varphi - 1) - k\,\mathrm{c}2\varphi)}{-\mathrm{c}2\varphi(F_z + R_{PM}(\mathrm{c}\varphi - 1) - k\,\mathrm{c}2\varphi)}$$

$$(2.23)$$

Eq. (2.23) is a first-order ordinary differential equation that is numerically integrated from φ_i to φ_o (see Figure 2-8), with initial value $k(\varphi_i) = k_i$. Inserting the resulting function $k(\varphi)$ into Eq. (2.16) finally gives the SM profile. For the nominal prototype (baseline) parameters of Table 2-1, SM is shown in Figure 2-9. The SM profile shape is close to a straight line, with an average distance from the regression line $z = 0.1273x + 2.3915$ (indicated

by the dashed line in Figure 2-9) of 2.09 mm. Concluding, the right *SM* surface is expressed in 3D by:

$$SM(\varphi) = \begin{pmatrix} O_{PM,x} \\ 0 \\ R_{PM} \end{pmatrix} + R_{PM} \cdot \begin{pmatrix} \sin\varphi \\ 0 \\ -\cos\varphi \end{pmatrix} + k(\varphi) \cdot \begin{pmatrix} -\sin 2\varphi \\ 0 \\ \cos 2\varphi \end{pmatrix} + q \cdot \begin{pmatrix} 0 \\ 1 \\ 0 \end{pmatrix} \quad (2.24)$$

where $0 \le q \le l_{SM}$.

O_{PM}, $[\mathrm{m}]$	(-0.444, 8.0)
R_{PM}, $[\mathrm{m}]$	8.0
P_{i}, $[\mathrm{m}]$	(0.730, 0.0865)
P_{o}, $[\mathrm{m}]$	(3.970, 1.327)
f, $[\mathrm{m}]$	1.44
ϕ_{rim}, $[\mathrm{deg}]$	52.8
w_{PM}, $[\mathrm{m}]$	7.94
w_{SM}, $[\mathrm{m}]$	1.92

Table 2-1: Nominal prototype (baseline) concentrator parameters used in the derivation of *SM*.
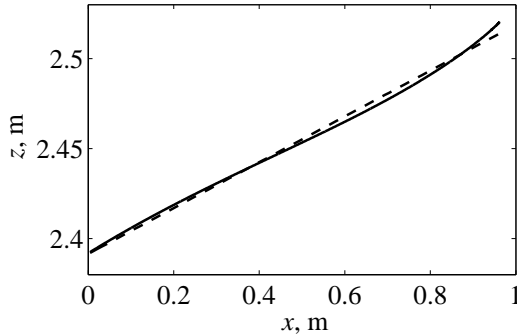
Figure 2-9: Right-hand side *SM* profile for the baseline parameters of Table 2-1 (solid line), and linear regression $z = 0.1273x + 2.3915$ (dashed line); the average distance between the *SM* profile and the regression line is 2.09 mm.

2.3 The Monte Carlo Simulation

The Monte Carlo (MC) ray-tracing technique is applied. [15] It consists of following a large number of stochastic sunrays of solid angle $\theta_{sun} = 6.72 \cdot 10^{-5}$ sr and uniformly incident on the solar trough concentrating system. The system is defined as the combined PM and SM reflectors and the transparent top foil. The analysis is carried out in 3 dimensions to account for skew rays. The wavelength λ assigned to a generic random sunray is found by solving

$$\Re_\lambda = F_{0-\lambda} \qquad (2.25)$$

where $F_{0-\lambda}$ is the fractional function of the reference solar spectrum and $\Re_\lambda$ is a random number chosen from a uniform set $0 \div 1$. Other random choices determine whether the incident ray is transmitted through the transparent envelope and reflected by PM and SM, depending on $T_{r,\lambda}(\theta)$ and ρ_{mirror}. Bivariate Chi Squared probability density distributions with mode σ are assumed for the local surface errors of PM and SM. [16] The skew angle θ_{skew}, formed by the incident sunray and the normal to the PM aperture area, is evidently determined for a specific location, day of the year, and time of the day. [14] Sun-tracking is around the y-axis.

Samples of 10^7 rays were used for each MC run. The baseline case uses the dimensions of Table 2-1, $l_{target} = l_{PM} = 49.4$ m, $\theta_{skew} = 0°$, perfect transparent envelope, perfect specular reflection on both PM and SM, and no mirror surface errors ($\sigma_{PM} = \sigma_{SM} = 0$ mrad). All results are calculated with respect to the unshaded PM aperture of width $w_{PM} - w_{SM}$. Two indicators characterize the overall optical performance of the system. The system's solar concentration ratio C is defined as the radiative flux at the focal plane, normalized by the direct normal solar irradiance, DNI. The system's intercept factor γ is defined as the percentage of solar radiation incident on the focal plane that is intercepted by a rectangular target of length l_{target} and width w_{target}, located at the focal plane and aligned along the x- and y-axes of the system, as shown in Figure 2-4.

Figure 2-10a and Figure 2-10b show the influence of PM's surface errors on C and γ. C peaks at 151 for the ideal case. For $\sigma_{PM} = 10$ mrad, the peak C decreases by 86% from its ideal case value to 22, while γ is re-
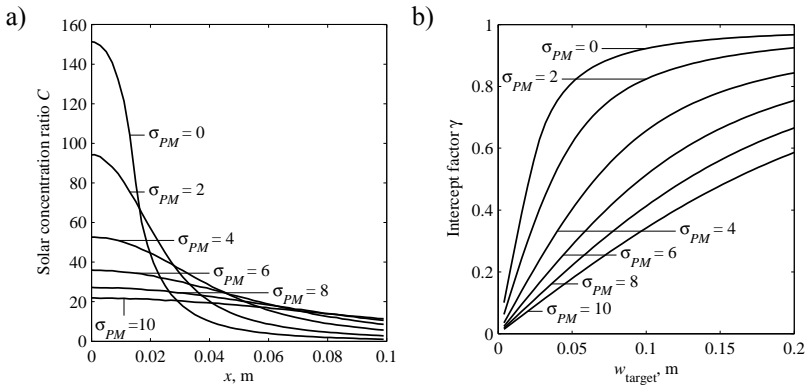
Figure 2-10: a) Distribution of the solar concentration ratio on the target plane along the x-axis; b) intercept factor as a function of the target's width; the parameter is the *PM*'s surface error mode σ_{PM} in the range 0÷10 mrad.

duced by 63% from its ideal case value to 34% for a target of width 0.1 m. Interestingly, even a 0.2 m-wide target is not able to intercept spilled radiation completely for all cases where $\sigma_{PM} \geq 2$ mrad. Note that the asymptote of the γ-curve for the ideal case is at $\gamma = 0.977$, as 2.3% of the incident solar radiation misses *SM* after reflection on *PM*. These losses increase approximately linearly with increasing *PM* surface errors, reaching 8.1% at $\sigma_{PM} = 10$ mrad. Typically, $\sigma = 2.5$ mrad for parabolic trough concentrators. [17]

Figure 2-11a shows the distribution of C along the x-axis for various *SM*'s surface errors with σ_{SM} in the range of 0÷10 mrad. For $\sigma_{SM} = 10$ mrad, the peak C decreases by 52% to 73 as compared with the ideal case. Figure 2-11b shows γ as a function of w_{target} for various *SM*'s surface errors with σ_{SM} in the range 0÷10 mrad. A 0.2 m-wide target is able to intercept practically all radiation even for a *SM*'s surface error $\sigma_{SM} = 10$ mrad. As w_{target} is reduced from 0.2 to 0.05 m, γ decreases by 44% because of the spilled radiation. There is evidently a stronger influence on the system performance by the *PM*'s surface errors as compared to that by the *SM*'s surface errors, as sunrays travel a longer optical path from *PM* the target than from *SM* to the target.
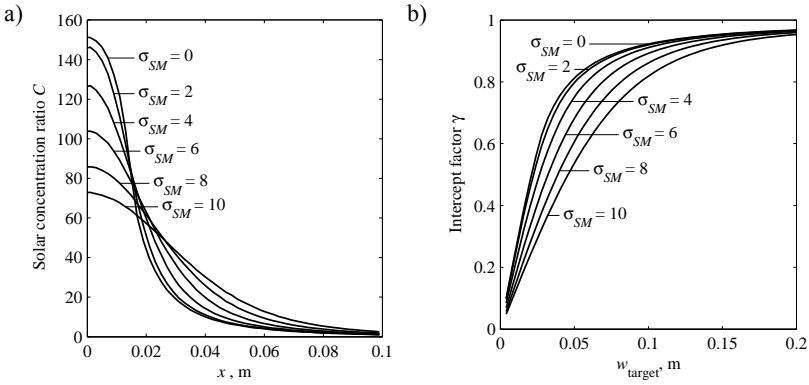
Figure 2-11: a) Distribution of the solar concentration ratio on the target plane along the x-axis; b) intercept factor as a function of the target's width; the parameter is the SM's surface error mode σ_{SM} in the range 0÷10 mrad.

A contour map distribution of the solar concentration ratio at the focal plane is shown in Figure 2-12 for a system with $\left|\boldsymbol{u}_{\max}\right| = 3$ mm, inclined by $\beta_{\text{inclination}} = 30°$. Figure 2-13 shows the corresponding C-profiles along the x-axis at various y-positions. A strong variation along the y-axis is observed, with peak C-values ranging from 52 to 151. Note that the curves are slightly asymmetric. C becomes more uniform as the beam deformation increases (i.e. towards $y = 18.53$ m). Figure 2-14a and b show the C-profiles along the x-axis for various maximum beam displacements, averaged over the concentrator length, and the corresponding γ-curves. For $\left|\boldsymbol{u}_{\max}\right| = 5$ mm, the peak C reaches 60 – a drop of about 60% as compared to the case with no beam deformation. On a 0.1 m wide target, γ decreases from 92% to 63% as $\left|\boldsymbol{u}_{\max}\right|$ increases from 0 to 5 mm.
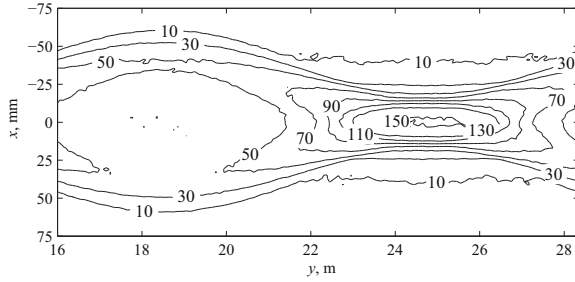
16

Figure 2-12: Contour map of the solar concentration ratio at the focal plane for a system with a maximum beam deformation $\left| \boldsymbol{u}_{\max} \right| = 3$ mm (at $\beta_{\text{inclination}} = 30°$).
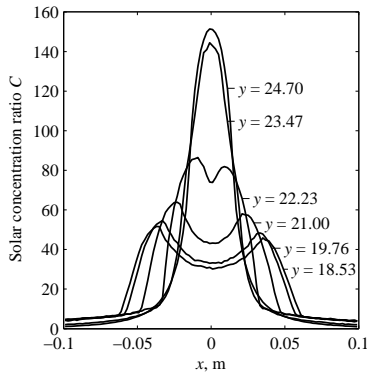

Figure 2-13: Distribution of the solar concentration ratio on the target along the x - axis for a system with a maximum beam deformation $\left| \boldsymbol{u}_{\max} \right| = 3$ mm (at $\beta_{\text{inclination}} = 30°$); the parameter is the axial position in the range $y = 18.53 \div 24.70$ m (half of one *PM* section).
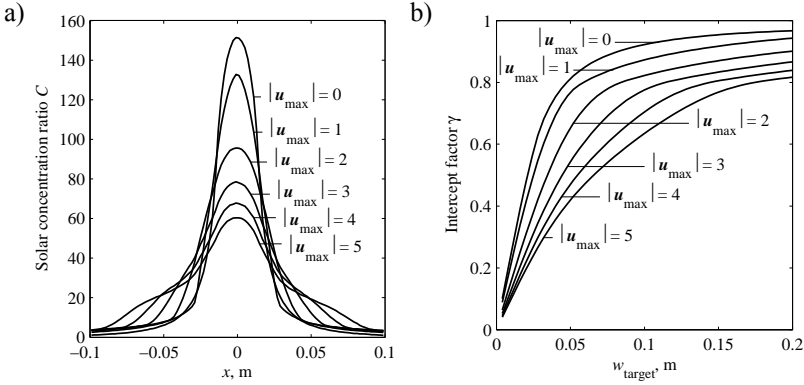
a)

b)

Figure 2-14: Distribution of the solar concentration ratio on the target along the x - axis (a), and the system's intercept factor as a function of the target width (b), for various maximum beam deformations $|u_{max}|$ (in [mm], at $\beta_{inclination} = 30°$, distribution averaged over the concentrator length).

2.4 Experimental Validation

The MC simulation model was validated in terms of the measured solar concentration ratio C on the prototype system. Optical measurements were performed on a 610x410 mm² water-cooled Lambertian target, made of ZrO_2 and plasma coated with Al_2O_3, which was mounted at the focal plane. The diffusely reflected radiation was recorded with a charge coupled (CCD) camera (Basler progressive scan, 1392x1040 pixels resolution) equipped with neutral density glass filters. The resulting grayscale images of the target underwent offset and distortion corrections and were calibrated using two absolute heat flux gauges (Vatell TG 1000-0, calibration accuracy $\pm3\%$, water cooled), incorporated in the target. Direct normal insolation was measured with a pyrheliometer (Kip and Zonen, 5° acceptance angle). The measurements were taken in Biasca, Switzerland (latitude = 46°22'N, longitude = 8°58'E).

The spectral normal reflectivity $\rho_{mirror,\lambda,n}$ of *PM* and *SM* is shown in Figure 2-15a, as measured with a spectrometer (Ocean Optics). Directional dependence of the reflectivity is neglected and the hemispherical total reflectivity ρ_{mirror} is calculated from:

18

$$\rho_{\text{mirror}} = \frac{\int_0^\infty \rho_{\text{mirror},\lambda,\text{n}} \cdot DNI_\lambda \, d\lambda}{\int_0^\infty DNI_\lambda \, d\lambda} \tag{2.26}$$

where DNI_λ is the spectral direct normal solar irradiance (beam + circumsolar). Assuming AM = 1.5 with ASTM G173-03 reference spectrum for DNI_λ, as shown in Figure 2-15b, Eq. (2.26) yields $\rho_{\text{mirror}} = 0.92$, which is consistent with the solar-weighted values for polished aluminium $\rho = 0.91$ [14] and $\rho = 0.90$ [18]. Figure 2-16 shows the measured spectral normal transmittance $T_{r,\lambda,\text{n}}$ and reflectance $R_{e,\lambda,\text{n}}$ of the transparent envelope for normal incidence solar radiation. For a single-layer semi-transparent envelope [15],

$$R_e = \rho\left(1 + \tau T_r\right) \tag{2.27}$$

$$T_r = \tau \frac{\left(1-\rho\right)^2}{1+\rho^2\tau^2} \tag{2.28}$$

$$\rho_{\text{n}} = \frac{\left(n-1\right)^2}{\left(n+1\right)^2} \tag{2.29}$$

where ρ, τ, and n denote the surface reflectivity, medium transmissivity, and refractive index of the envelope, respectively. Using the measured $T_{r,\lambda,\text{n}}$ and $R_{e,\lambda,\text{n}}$, Eqs. (2.27) to (2.29) are solved for $\rho_{\lambda,\text{n}}$, $\tau_{\lambda,\text{n}}$, and n_λ. Further applying Snell,
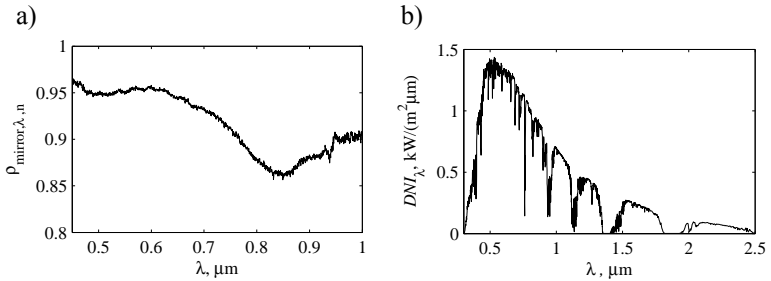

Figure 2-15: a) Measured spectral normal reflectivity $\rho_{\text{mirror},\lambda,\text{n}}$ of *PM* and *SM* (data source: Airlight Energy SA); b) ASTM G173-03 reference solar spectrum [19], used to calculate the total mirror reflectivity ρ_{mirror}.
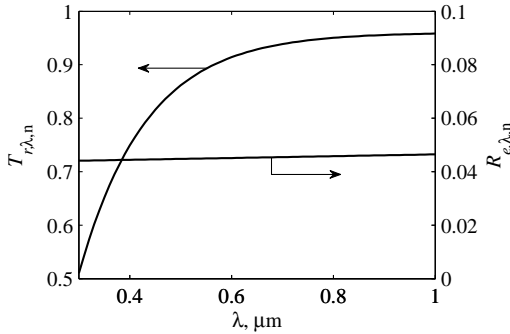
Figure 2-16: Measured spectral normal transmittance $T_{r,\lambda,n}$ and reflectance $R_{e,\lambda,n}$ of the transparent envelope (data source: Airlight Energy SA).

Fresnel, and Bouguer laws for solar radiation incident at an angle θ, the envelope directional reflectivity $\rho_\lambda(\theta)$ and transmissivity $\tau_\lambda(\theta)$ are calculated, which, after inserting into Eq. (2.28), yield $T_{r,\lambda}(\theta)$. The percentage of incident solar radiation transmitted through the envelope as a function of the skew angle θ_{skew} is shown in Figure 2-17.
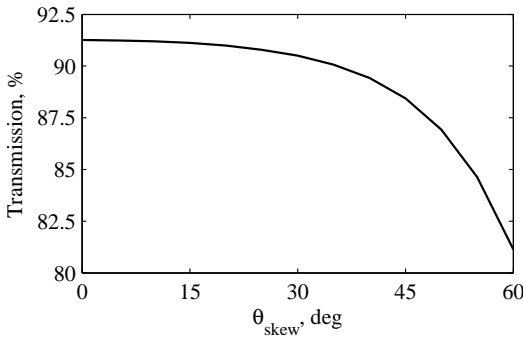

Figure 2-17: Percentage of incident solar radiation transmitted through the transparent envelope as a function of the skew angle θ_{skew}.

All solar flux measurements were performed with flat SM, mounted at z = 2.41 m outer rim height, descending with a slope angle of 1.3° towards the center. Maximum measured peak solar concentration ratio was 55. A

20

rectangular region of interest (ROI) of 100x240 mm^2, devided into 100x20 segments, was considered. Numerically simulated (solid curve) and experimentally measured (dashed curve) local C-distributions at two arbitrary y-positions on the target ($y = 18.88$ and 19.03 m) are shown in Figure 2-18.
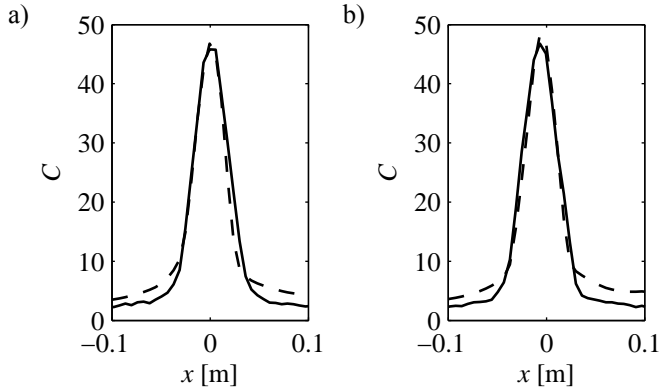

Figure 2-18: Numerically simulated (solid curve) and experimentally measured (dashed curve) local C-distributions at a) $y = 18.88$ m, b) $y = 19.03$ m; the insolation data and validation results are given in Table 2-2, case 1.

case	1	2	3
date	25/09/08	25/09/08	25/09/08
local time	11:56:17	12:23:39	13:13:43
DNI , $\left[\text{W/m}^2 \right]$	814	883	869
θ_{skew} , $\left[\text{deg}\right]$	-19.8	-12.7	-0.420
$c_{\text{meas.,sim.}}\big|_{\text{ROI}}$	0.983	0.988	0.985
$\Delta C_{\text{mean}}\big|_{\text{ROI}}$, $\left[\%\right]$	16.0	13.3	10.1
$\Delta Q\big|_{\text{ROI}}$, $\left[\%\right]$	-2.71	5.75	4.78

Table 2-2: MC model validation results for 3 cases ($\theta_{\text{skew}} < 0°$: before solar noon)

A 10% radiation loss was introduced in all simulations to account for the reduced envelope transmittance due to dust. This value resulted in the best match between simulated and measured peak solar concentration ratios. The agreement between simulations and measurements inside the ROI was examined with respect to the standard covariance coefficient

$$c_{\text{meas.,sim.}}\big|_{\text{ROI}} = \left(\frac{\text{cov}\left(C_{\text{meas.}}, C_{\text{sim.}}\right)}{\sigma_{\text{meas.}} \sigma_{\text{sim.}}} \right)\bigg|_{\text{ROI}} , \quad -1 \le c_{\text{meas.,sim.}}\big|_{\text{ROI}} \le 1 \quad (2.30)$$

mean relative difference of the solar concentration ratio

$$\Delta C_{\text{mean}}\big|_{\text{ROI}} = \frac{1}{m_{\text{seg}} \cdot n_{\text{seg}}} \sum_{j=1}^{n_{\text{seg}}} \sum_{i=1}^{m_{\text{seg}}} \left(\left| 1 - \frac{C_{\text{sim.}}^{i,j}}{C_{\text{meas.}}^{i,j}} \right| \right) \cdot 100 , \left[\% \right] \quad (2.31)$$

and total incident radiative power

$$\Delta Q\big|_{\text{ROI}} = DNI \cdot \sum_{j=1}^{n_{\text{seg}}} \sum_{i=1}^{m_{\text{seg}}} \left(1 - \frac{C_{\text{sim.}}^{i,j}}{C_{\text{meas.}}^{i,j}} \right) \cdot \Delta x_{\text{seg}} \cdot \Delta y_{\text{seg}} \cdot 100 , \left[\% \right] \quad (2.32)$$

where m_{seg} and n_{seg} are the numbers of segments on the ROI in x - and y -directions, $C_{\text{meas.}}^{i,j}$ and $C_{\text{sim.}}^{i,j}$ are the measured and simulated local solar concentration ratios on ROI-segment (i, j), and Δx_{seg} and Δy_{seg} are the segment edge lengths. The data comparisons between the numerically simulated and experimentally measured results are listed in Table 2-2 for 3 different measurements (denoted by case 1 to 3). For all three cases, the mirror surface errors were set to zero. In general, the MC model predicts the radiative power incident on the ROI within 6% of the measured values, with mean deviation of $\Delta C_{\text{mean}}\big|_{\text{ROI}} < 18\%$. The relatively high values of $\Delta C_{\text{mean}}\big|_{\text{ROI}}$ are mainly due to the discrepancy at the branches of the C -distributions (Figure 2-18). These outer regions of low solar concentration play a minor role in high-temperature applications as they are only partly intercepted by the receiver. In contrast, the peaks match well. $c_{\text{meas.,sim.}}\big|_{\text{ROI}}$ is used to find the relative position of two corresponding C -distributions (measured vs. simulated) that lead to the best agreement.

In all cases considered, surface errors lead to broader C -distributions. This is observed in Figure 2-19, where the measured and simulated C -distributions are plotted for case 1 (Table 2-2) with $\sigma_{PM} = 2$ mrad; all other

baseline parameters were kept unchanged. The corresponding quantitative results are listed in Table 2-3.
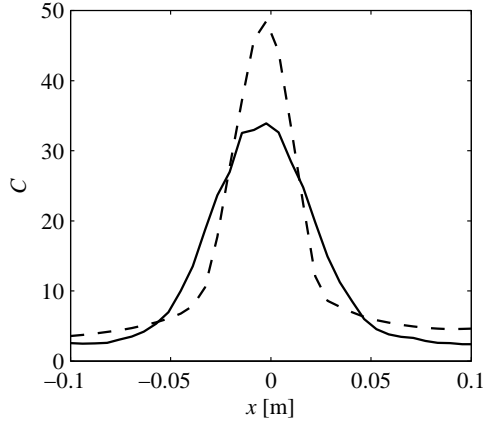

Figure 2-19: C-distribution for case 1 (Table 2-3) with $\sigma_{PM} = 2$ mrad (dashed line: measurement, solid line: simulation).

$c_{\text{meas.,sim}}\big|_{\text{ROI}}$	0.9279
$\Delta C_{\text{mean}}\big|_{\text{ROI}}$, $\left[\%\right]$	26.4
$\Delta Q\big|_{\text{ROI}}$, $\left[\%\right]$	6.96

Table 2-3: Comparison of simulation and measurement for case 1 with $\sigma_{PM} = 2$ mrad.

The measured C-distribution for case 1 at $y = 18.88\,\text{m}$ is compared to that obtained numerically (MC simulation) for an equivalent parabolic trough concentrator (i.e. $\phi_{\text{rim}} = 55.8°$, 5.78 m unshaded aperture width, $\rho = 0.92$, $\sigma_{PM} = 2.5\,\text{mrad}$). Results are shown in Figure 2-20. The differences are mainly due to the additional transmission losses through the envelope, reflection losses at *SM*, and spilled radiation caused by the flat *SM* installed during the measurements.
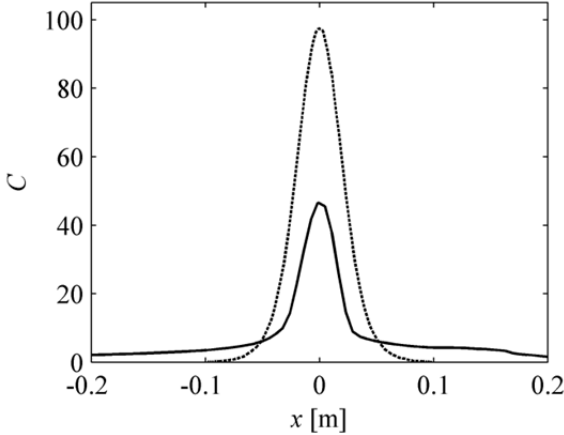
Figure 2-20: Measured C-distribution for case 1 (solid line) and for a parabolic trough concentrator with $\sigma_{PM} = 2.5$ mrad (dashed line).

2.5   Summary and Conclusions

We have presented a novel design for a solar trough concentrator system that features pneumatic polymer mirrors supported on precast concrete frames. Optical aberration caused by the circular primary mirrors (*PM*) is corrected by tailor-designed secondary mirrors (*SM*) for maximum solar concentration. Ideal peak solar concentration ratio is 151. Measured peak solar concentration ratio on a 50x8 m² prototype system with flat *SM* was 55, measured at 8.6° solar incidence angle. Performance reducing factors were: 1) flat instead of ideally curved *SM*, 2) average mirror reflectivity of 0.92, 3) attenuation of incoming solar radiation through the transparent envelope by 9 to 19% for θ_{skew} varying from 0 to 60°, and 4) additional 10% attenuation due to dust on the transparent envelope. A Monte Carlo ray-tracing simulation indicated that surface errors of the PM have a strong influence on the concentrator performance, reducing the peak C to 22 (-86%) for $\sigma_{PM} = 10$ mrad. In contrast, same surface errors of the *SM* reduce C to 73 (-52%) as the optical path of the sunray between reflection and target is shorter. Similarly, the intercept factor for a concentrator with a 0.1 m wide target area is reduced from 92% to 34% (-63%) for $\sigma_{PM} = 10$ mrad,

and to 82% (-11%) for $\sigma_{SM} = 10$ mrad. Nevertheless, comparisons of experimentally measured and numerically simulated C-distributions indicate that mirror surface errors can be neglected. Deformations of the *PM* supporting structure caused by its own weight lead to nonlinear C-distributions along the concentrator axis. For example, a 5mm maximum deformation at a concentrator slope $\beta_{\text{inclination}} = 30°$ reduces the peak C (averaged along the concentrator length) to 60.

3 Arc-Spline Solar Trough Concentrator[1]

The initial concentrator design used tailor-made secondary mirrors to correct for optical aberrations introduced by the circular-cylindrical primary mirrors, which however caused additional reflection and spillage losses (chapter 2). This chapter describes a substantially improved optical design, which avoids the secondary mirrors by overlapping multiple mirror membranes to form a multi-circular primary mirror profile that closely approximates the parabolic shape. A 45m-long, 10m-wide concentrator test section has been built and installed perpendicularly to the meridian in Biasca, Switzerland. Radiative flux measurements are presented. A Monte Carlo (MC) ray-tracing simulation of the concentrator is formulated, experimentally validated, and further applied to elucidate the concentrator's sensitivity to typical manufacturing and operational imperfections, such as errors of the mirror membrane widths, membrane inflation pressure deviations, and deformations of the support structure due to tensile forces exerted by the membranes and gravity forces.

3.1 Optical Design

The concentrator design is depicted in Figure 3-1. Its 1-axis tracking precast concrete structure consists of 11m-long thin-walled longitudinal girders that are supported at their ends by semicircular transversal trusses (Figure 3-1a). The transversal elements are supported by over-ground concrete foundations via roller-bearings to enable rotation with chain drives. The center of mass is maintained close to the rotation axis to minimize transmission forces. The receiver is mounted on the central girders via steel posts. An inflated air tube (1-2 mbar overpressure), formed by a transparent

---

[1] The material in this chapter has been published in: Bader R., Pedretti A., Steinfeld A., "A 9m-Aperture Solar Parabolic Trough Concentrator Based on a Multilayer Polymer Mirror Membrane Mounted on a Concrete Structure", *ASME Journal of Solar Energy Engineering*, Vol. 133, pp. 031016, 2011.

ETFE-membrane and a silicone-coated fiberglass fabric, is installed on the concrete structure, enclosing central girder, receiver, and mirrors (Figure 3-1b). The mirrors are made up of 4 stacked Mylar polymer membranes per mirror wing, with the two top membranes being aluminized and acting as the reflector. These very light membranes are attached to the concrete structure along their edges, and subdivide the air tube into 8 different pressure zones. Air blowers generate small vacuums of a few Pa underneath each membrane, causing the top membranes' profiles to form arrays of 4 tangentially adjacent circular arcs, referred to as arc-spline. One arc is added to the arc-spline per installed mirror membrane. The mirror setup is designed such that the arc-spline approximates a parabola. A photograph of the 45m-long, 9m-aperture prototype is shown in Figure 3-1c.
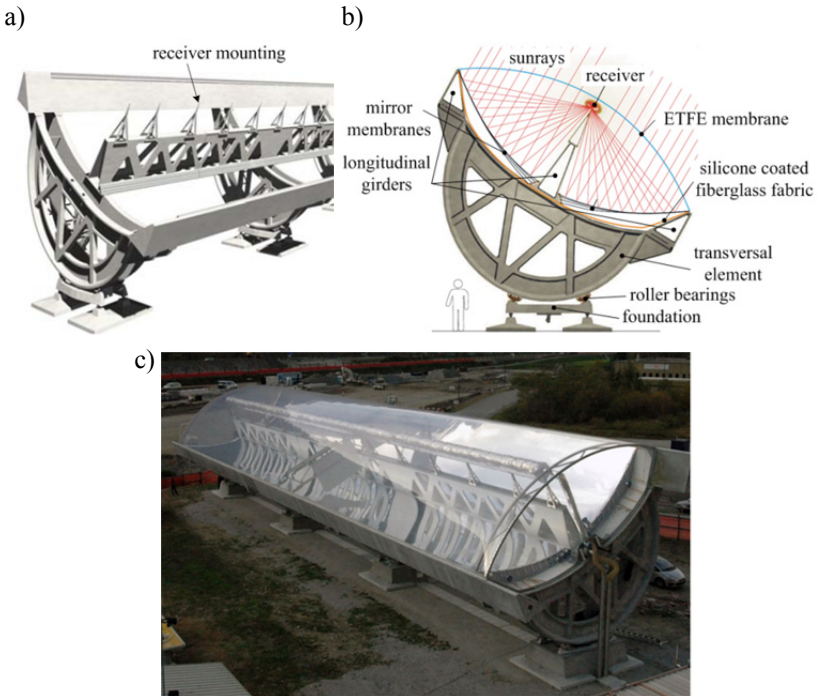
a)   b)

c)

Figure 3-1: a) Concrete support structure and foundation, receiver posts; b) inflated air tube, formed by ETFE-membrane and fiberglass fabric, containing pneumatically spanned mirror membranes and receiver; c) photograph of the 45m-long, 10m-wide prototype (source: Airlight Energy SA).

The geometry of an arc-spline with $n_{\text{arc}} = 4$ arcs is shown in Figure 3-2 as a black solid line. This geometry is to be fitted to a parabola, described by $z_{\text{parabola}} = x_{\text{parabola}}^2 / 4f$, where f denotes the focal length. Arc i ($i = 1, 2, ..., n_{\text{arc}}$) of the arc-spline is defined by its center point $P_{0,i} = (x_{0,i}, z_{0,i})$, radius R_i, and boundary points $P_i = (x_i, z_i)$, $P_{i+1} = (x_{i+1}, z_{i+1})$, referred to as nodes of the arc-spline. The coordinates of $P_{0,i}$ and the magnitude of R_i are calculated from the set of equations:

$$\left(x_i - x_{0,i}\right)^2 + \left(z_i - z_{0,i}\right)^2 = R_i^2 \tag{3.1}$$

$$\left(x_{i+1} - x_{0,i}\right)^2 + \left(z_{i+1} - z_{0,i}\right)^2 = R_i^2 \tag{3.2}$$

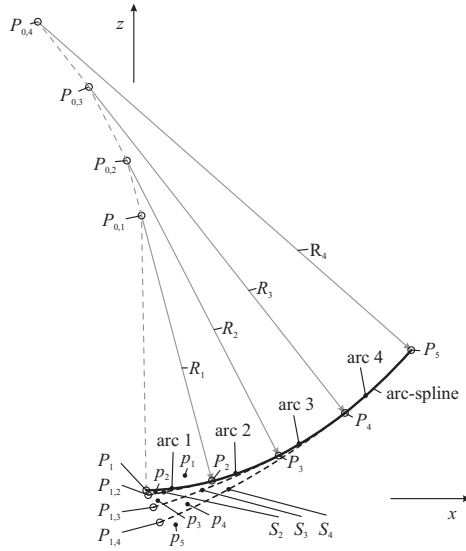$$m_i = \frac{x_i - x_{0,i}}{z_{0,i} - z_i} \tag{3.3}$$

Figure 3-2: Geometry of the arc-spline (black solid line) with $n_{\text{arc}} = 4$ arcs per wing, running from P_1 to P_5; the profile of support membrane j ($j = 2, 3, ..., n_{\text{arc}}$, black dashed lines) consists of a circular section S_j running from inner clamping point $P_{1,j}$ to node $P_{i=j}$, and a tangentially adjacent section running from $P_{i=j}$ to outer clamping point P_5, which is coincident with the arc-spline profile; membrane pressures are indicated by p_1 to p_5.

yielding:

$$x_{0,i} = \frac{m_i \left(x_i^2 - x_{i+1}^2 - \left(z_i - z_{i+1} \right)^2 \right) + 2x_i \left(z_{i+1} - z_i \right)}{2 \left(m_i \left(x_i - x_{i+1} \right) + z_{i+1} - z_i \right)} \tag{3.4}$$

$$z_{0,i} = \frac{\left(x_i - x_{i+1} \right)^2 + 2m_i \left(x_i - x_{i+1} \right) z_i + z_{i+1}^2 - z_i^2}{2 \left(m_i \left(x_i - x_{i+1} \right) + z_{i+1} - z_i \right)} \tag{3.5}$$

$$R_i = \frac{1}{2} \left[\frac{\left(1 + m_i^2 \right)\left(\left(x_i - x_{i+1} \right)^2 + \left(z_i - z_{i+1} \right)^2 \right)^2}{\left(m_i \left(x_i - x_{i+1} \right) + z_{i+1} - z_i \right)^2} \right]^{\frac{1}{2}} \tag{3.6}$$

Continuity of slope m_i at node P_i, for $i = 2, 3, ..., n_{\text{arc}}$, yields:

$$m_i = \frac{x_i - x_{0,i-1}}{z_{0,i-1} - z_i}, \text{ for } i = 2, 3, ..., n_{\text{arc}} \tag{3.7}$$

Thus, the 3D arc-spline mirror surface is described by:

$$\begin{cases} x_1 \leq x_{\text{AS}} \leq x_{n_{\text{arc}}+1} \\ 0 \leq y_{\text{AS}} \leq l_{\text{concentrator}} \\ z_{\text{AS}} \left(x_{\text{AS}} \right) = z_{0,i} - \sqrt{R_i^2 - \left(x_{\text{AS}} - x_{0,i} \right)^2}, \ i = 1, 2.., n_{\text{arc}} \end{cases} \tag{3.8}$$

with parameters $P_{0,i}$ and R_i given by Eqs. (3.4) to (3.7), valid within the intervals $\left[x_i, x_{i+1} \right]$. Prescribing x_1 and $x_{n_{\text{arc}}+1}$ (which define the arc-spline width), the set $\boldsymbol{v}$ of $2n_{\text{arc}}+1$ free parameters m_1, z_1, x_i, z_i, for $i = 2, 3, ... n_{\text{arc}}$, and $z_{n_{\text{arc}}+1}$, is determined by the least-squares optimization which minimizes slope angle (α) and positional (z) differences between arc-spline and underlying parabola at n_{ref} equidistant reference locations, $x_{i_{\text{ref}}}$, between x_1 and $x_{n_{\text{arc}}+1}$: [20]

$$\begin{aligned} Q_{\min} = \sum_{i_{\text{ref}}=1}^{n_{\text{ref}}} \Big\{ & w_\alpha \cdot w_{\text{ray}} \left(x_{i_{\text{ref}}} \right) \cdot \left[\alpha_{\text{parabola}} \left(x_{i_{\text{ref}}} \right) - \alpha_{\text{AS}} \left(x_{i_{\text{ref}}} \right) \right]^2 \dots \\ & + w_z \cdot \left[z_{\text{parabola}} \left(x_{i_{\text{ref}}} \right) - z_{\text{AS}} \left(x_{i_{\text{ref}}} \right) \right]^2 \Big\} \to 0 \end{aligned} \tag{3.9}$$

where w_α and w_z are weighting factors. The weighting function $w_{\text{ray}} \left(x \right)$:

$$w_{\text{ray}} \left(x \right) = \frac{1}{f} \sqrt{x^2 + \left(f - z_{\text{parabola}} \left(x \right) \right)^2} \cdot \left[\cos \left(2\alpha_{\text{parabola}} \left(x \right) \right) \right]^{-1} \tag{3.10}$$

takes into account the variation of the ray's travel distance between reflection on the mirror and incidence point on the target plane, and the ray's incidence angle onto the target plane described by $z_{target} = f$. The baseline concentrator dimensions and the optimized arc-spline parameters for $n_{arc} = 4$ are listed in Table 3-1. The resulting arc-spline profile is shown in Figure 3-3.

		arc-spline parameters		
baseline dimensions		i/j	$R_i,[\mathrm{m}]$	$R_{S,j},[\mathrm{m}]$	$p_i^{design},[\mathrm{Pa}]$
focal length $f,[\mathrm{m}]$	3.5	1	7.37	-	33.23
inner boundary $x_1,[\mathrm{m}]$	0.5	2	8.50	10.1	19.66
outer boundary $x_{n_{arc}+1},[\mathrm{m}]$	5	3	10.1	16.2	9.71
rim angle $\phi_{rim},[\mathrm{deg}]$	71	4	12.0	28.4	3.52

Table 3-1: Baseline concentrator dimensions, and best-fit arc-spline parameters for $n_{arc} = 4$: arc-spline radii R_i, radii $R_{S,j}$ of sections S_j, and membrane pressures p_i^{design} relative to $p_{n_{arc}+1}^{design} = 0$.
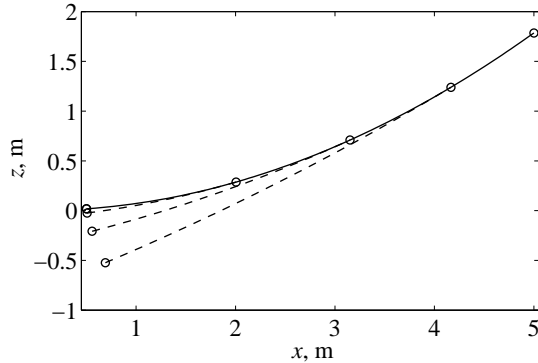

Figure 3-3: Best-fit arc-spline profile (solid line), suspended sections of support membrane profiles (dashed lines) for $n_{arc} = 4$; circles indicate clamping points (prescribed) and arc boundaries (nodes); the baseline concentrator dimensions and the arc-spline parameters are listed in Table 3-1.

Figure 3-4 compares arc-spline profile and reference parabola with respect to z- and α- differences. Maximum and root-mean-square -differences are, respectively: $\Delta z_{max} = 0.33$ mm, $\Delta z_{rms} = 0.18$ mm, $\Delta\alpha_{max} = 1.98$ mrad, $\Delta\alpha_{rms} = 0.8$ mrad. The z- and α-errors decrease with increasing x-coordinate as a result of their higher weighting by w_{ray}.
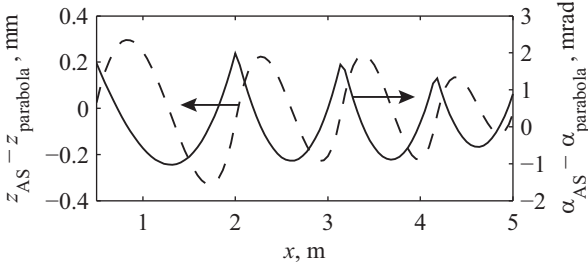

Figure 3-4: z-coordinate difference (dashed line) and slope angle α-difference (solid line) between arc-spline (AS) with $n_{arc} = 4$ arcs (Figure 3-3) and reference parabola. The arc-spline parameters in Table 3-1 apply.

While the top mirror membrane assumes the arc-spline profile, the profile of support mirror membrane j ($j = 2,3,...,n_{arc}$) consists of arcs $i = j, j+1,...,n_{arc}$ of the arc-spline, and a circular section S_j, which is suspended from the arc-spline and runs from inner clamping point $P_{1,j} = (x_{1,j}, z_{1,j})$ to node $P_{i=j}$, where it is tangentially adjacent to the arc-spline (Figure 3-2). Center point $P_{0,S,j}$ and radius $R_{S,j}$ of S_j are calculated from:

$$x_{0,S,j} = x_i - \frac{m_i \cdot \left[\left(x_{1,j} - x_i\right)^2 + \left(z_{1,j} - z_i\right)^2 \right]}{2 \cdot \left[z_{1,j} - z_i - m_i \left(x_{1,j} - x_i\right) \right]} \tag{3.11}$$

$$z_{0,S,j} = z_i + \frac{\left[\left(x_{1,j} - x_i\right)^2 + \left(z_{1,j} - z_i\right)^2 \right]}{2 \cdot \left[z_{1,j} - z_i - m_i \left(x_{1,j} - x_i\right) \right]} \tag{3.12}$$

$$R_{S,j} = \frac{\sqrt{1 + m_i^2} \cdot \left[\left(x_{1,j} - x_i\right)^2 + \left(z_{1,j} - z_i\right)^2 \right]}{2 \cdot \left[z_{1,j} - z_i - m_i \left(x_{1,j} - x_i\right) \right]} \tag{3.13}$$

where $i = j$. Thus, once the arc-spline geometry and clamping points $P_{1,j}$ are given, the support membrane geometries are fully determined. Finally, section S_j is described in 3D by:

$$\begin{cases} x_{1,j} \leq x_{S,j} \leq x_{i=j} \\ 0 \leq y_{S,j} \leq l_{\text{concentrator}} \\ z(x_{S,j}) = z_{0,S,j} - \sqrt{R_{S,j}^2 - (x_{S,j} - x_{0,S,j})^2} \end{cases} \quad , \ j = 2,3,...,n_{\text{arc}} \quad (3.14)$$

The resulting radii $R_{S,j}$ of sections S_j are given in Table 3-1. The support membrane profiles are shown in Figure 3-3 as dashed lines.

Final width of the top mirror membrane in operation is given by:

$$w_{\text{membrane},1}^{\text{nominal,design}} = \sum_{i=1}^{n_{\text{arc}}} l_{\text{arc},i} \quad (3.15)$$

with arc length $l_{\text{arc},i}$:

$$l_{\text{arc},i} = R_i \cdot \left[\sin^{-1}\left(\frac{x_{i+1} - x_{0,i}}{R_i} \right) - \sin^{-1}\left(\frac{x_i - x_{0,i}}{R_i} \right) \right] \quad (3.16)$$

Final width of support membrane j is given by:

$$w_{\text{membrane},j}^{\text{nominal,design}} = l_{S,j} + \sum_{i=j}^{n_{\text{arc}}} l_{\text{arc},i} \quad , \ j = 2,3,...,n_{\text{arc}} \quad (3.17)$$

with length of section S_j:

$$l_{S,j} = R_{S,j} \cdot \left[\sin^{-1}\left(\frac{x_{i=j} - x_{0,S,j}}{R_{S,j}} \right) - \sin^{-1}\left(\frac{x_{1,j} - x_{0,S,j}}{R_{S,j}} \right) \right] \quad (3.18)$$

Clamping points $P_{1,j}$, $j = 2,3,...,n_{\text{arc}}$, are selected such that all membranes have the same width, $w_{\text{membrane}}^{\text{nominal,design}}$. Membranes are elongated reversibly during operation due to tensile forces and thermal/hygroscopic expansion. Hence, the design membrane width at reference ambient temperature $T_{\text{ambient}}^{\text{reference}}$ and relative humidity $\varphi_{\text{ambient}}^{\text{reference}}$ and in the absence of tensile forces (e.g. during manufacturing) is calculated from:

$$w_{\text{membrane}}^{\text{reference,design}} = w_{\text{membrane}}^{\text{nominal,design}} \cdot \left[\left(1 + \Delta\varepsilon_{\text{th}} \left(T_{\text{ambient}}^{\text{nominal}} - T_{\text{ambient}}^{\text{reference}} \right) \right) \cdots \right.$$

$$\left. \cdot \left(1 + \Delta\varepsilon_\varphi \left(\varphi_{\text{ambient}}^{\text{nominal}} - \varphi_{\text{ambient}}^{\text{reference}} \right) \right) \cdot \left(1 + F_{\text{membrane}}' / \left(E_{\text{membrane}} \cdot d_{\text{membrane}} \right) \right) \right]^{-1}$$

$$(3.19)$$

where $\Delta\varepsilon_{th}$ and $\Delta\varepsilon_{\varphi}$ are the membrane's thermal and hygroscopic expansion coefficients, respectively, $F'_{membrane}$ is the tensile force acting on each membrane per unit concentrator length, $E_{membrane}$ is the membrane's Young's modulus, and $d_{membrane}$ is the membrane thickness. With parameters listed in Table 3-2, $w^{reference,design}_{membrane} = 4.8928$ m.

It is assumed that all membranes have negligible weight and stiffness. Hence they can only transmit tensile forces. Electrostatic and frictional forces between membranes are omitted from consideration. Consider a generic arc i of the arc-spline (composed of membranes 1 to i), bounded by nodes P_i and P_{i+1}, that is subjected to the pressure difference $\Delta p_{arc,i} = p_1 - p_{i+1}$, as shown in Figure 3-5. Force balance in z-direction is given by:

$$F'_{i,z} = F'_{i+1,z} = \frac{1}{2}\int_{-\zeta/2}^{\zeta/2} \Delta p_{arc,i} R_i \cos\zeta^* d\zeta^* = \Delta p_{arc,i} R_i \sin\zeta/2 \qquad (3.20)$$

reference ambient temperature $T^{reference}_{ambient},[K]$	293
design ambient temperature during operation $T^{nominal}_{ambient},[K]$ [1]	318
reference ambient relative humidity $\varphi^{reference}_{ambient},[\%]$	20
design ambient relative humidity during operation $\varphi^{nominal}_{ambient},[\%]$	20
thermal expansion coefficient $\Delta\varepsilon_{th},\left[m/(m\cdot K)\right]$ [21]	1.7E-5
hygroscopic expansion coefficient $\Delta\varepsilon_{\varphi},\left[m/(m\cdot\%)\right]$ [21]	0.6E-5
tensile force acting on membrane $F'_{membrane},[N/m]$	100
young's modulus $E_{membrane},\left[N/m^2\right]$	6.0E9
thickness $d_{membrane},[m]$	50E-6

Table 3-2: Parameters used to calculate the membrane width $w^{reference,design}_{membrane}$ at reference conditions ($T^{reference}_{ambient}$, $\varphi^{reference}_{ambient}$) and zero tensile forces.

---

[1] While the support membranes are assumed to be at $T_{ambient}$, the top mirror membrane temperature is estimated from an energy balance, described in Appendix D.
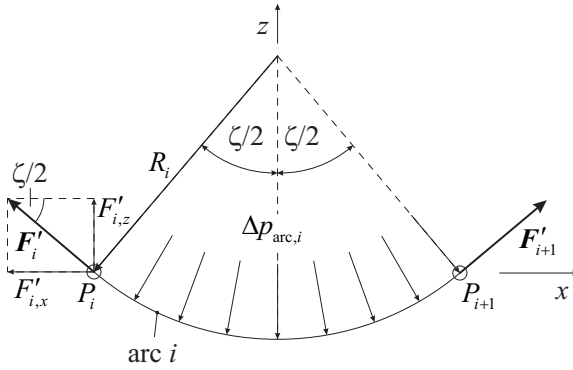
Figure 3-5: Force balance for arc i, fixed at nodes P_i and P_{i+1}, subjected to pressure difference $\Delta p_{\mathrm{arc},i} > 0$.

which yields the tensile force F_i' acting in arc i:

$$F_i' = F_{i+1}' = F_{i,z}' / \sin \zeta / 2 = \Delta p_{\mathrm{arc},i} R_i \tag{3.21}$$

Prescribing pressure p_1 and tensile force F_{membrane}', Eq. (3.21) yields:

$$p_2 = p_1 - F_{\mathrm{membrane}}' / R_1 \tag{3.22}$$

For nodes $i = 2, 3, ..., n_{\mathrm{arc}}$, F_i' is composed of two contributions: F_{i-1}' and F_{membrane}'. F_{i-1}' is transmitted by the stack of $i-1$ membranes composing arc $i-1$ of the arc-spline, while F_{membrane}' is transmitted by support membrane j via section S_j, where $j = i$ (Figure 3-2):

$$F_i' = F_{i-1}' + F_{\mathrm{membrane}}' , \quad i = 2, 3, ..., n_{\mathrm{arc}} \tag{3.23}$$

Inserting Eq. (3.21) into (3.23), pressures p_i, $i = 3, 4, ..., n_{\mathrm{arc}} + 1$, are found recursively from:

$$p_{i+1} = p_1 - \frac{1}{R_i} \left[F_{\mathrm{membrane}}' + R_{i-1} \left(p_1 - p_i \right) \right], \quad i = 2, 3, ..., n_{\mathrm{arc}} \tag{3.24}$$

For the arc-spline radii given in Table 3-1 and $F_{\mathrm{membrane}}' = 100\,\mathrm{N/m}$, the design membrane pressures p_i^{design} are calculated and listed in Table 3-1.

3.2 Parameter Study

The mirror shape that results when certain parameters are varied is found numerically by determining the set of free arc-spline parameters v via least-squares optimization. Imposed optimization criteria include:

i) Eq. (3.9) $\to 0$

ii) $\Delta p_{\text{rms},1}^2 = \sum_{i=1}^{n_{\text{arc}}+1} \left(p_i^{\text{calculated}} - p_i^{\text{prescribed}} \right)^2 \to 0$ (3.25)

with $p_i^{\text{calculated}}$, $i = 1, 2, ..., n_{\text{arc}} + 1$, calculated based on force balance Eq. (3.23),

iii) $\Delta w_{\text{rms},1}^2 = \sum_{i=1}^{n_{\text{arc}}} \left(w_{\text{membrane},i}^{\text{reference,calculated}} - w_{\text{membrane}}^{\text{reference,prescribed}} \right)^2 \to 0$ (3.26)

with $w_{\text{membrane},i}^{\text{reference,calculated}}$ calculated from membrane profile geometries and membrane elongation. $w_{\text{membrane}}^{\text{reference,prescribed}} = w_{\text{membrane}}^{\text{reference,design}} + \Delta w$, and $p_i^{\text{prescribed}} = p_i^{\text{design}} \mp \delta p$ (alternating, starting with $-$ for $i = 1$), where Δw and δp are the deviations of membrane widths and membrane pressures from the design values, respectively. The resulting radiative flux distribution at the focal plane is determined by MC ray-tracing. [15] Concentrator dimensions, mirror membrane properties, and design operating conditions are given in Table 3-1 and Table 3-2. 10^8 rays are used per simulation run. Ideal ETFE-membrane with transmittance $T_{r,\text{ETFE}} = 1$ and purely specular reflecting mirrors with reflectivity $\rho_{\text{mirror}} = 1$ are assumed throughout this section. Sunrays are incident parallel to the $y - z$-plane (Figure 3-2) and form an angle θ_{skew} with the z-axis. The sunshape model [22] is applied with circumsolar ratio $CSR = 5\%$. The radiative flux is expressed in dimensionless form by the solar concentration ratio C when normalized to the direct normal solar irradiance DNI.

3.2.1 Number of arcs

Figure 3-6 shows the C-distributions at the focal plane for optimized arc-spline concentrators with $n_{\text{arc}} = 2$ to 5 arcs per mirror wing, and for an ideal parabolic concentrator. Arc-spline profiles are optimized based on criterion (i). Peak concentrations C_{peak} increase from 83.8 for $n_{\text{arc}} = 2$ (-

64% compared to parabola) to 217.2 (-5.5%) for $n_{arc} = 5$. While the benefit of additional arcs is substantial up to 4 arcs, only a small improvement is achieved for additional arcs. This is also evident from Figure 3-7, where the average solar concentration ratio and the intercept factor are plotted as a function of the dimensionless width w_{target}/f of a rectangular target at the focal plane. Results for a 0.1m wide target are listed in Table 3-3. Geometry characteristics Δz_{rms} and $\Delta\alpha_{rms}$ of the resulting arc-splines are plotted in Figure 3-8.
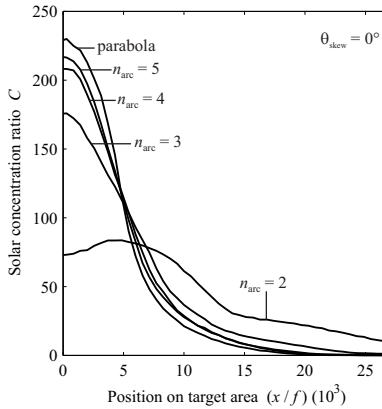

Figure 3-6: Distribution of the solar concentration ratio at the focal plane for optimized arc-spline concentrators with $n_{arc} = 2$ to 5 arcs per mirror wing, and for an ideal parabolic concentrator; distributions are symmetric to the ordinate of the graph.
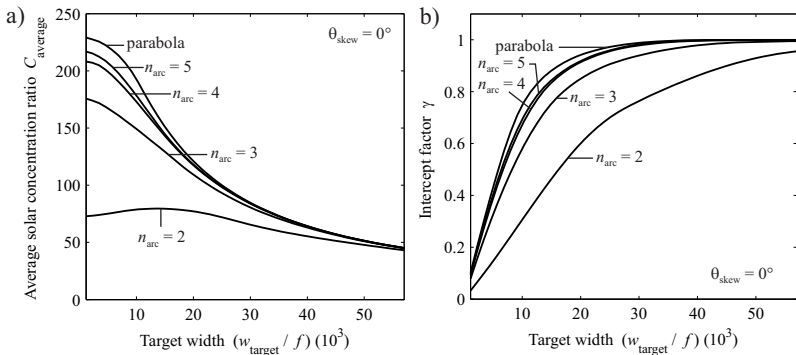

Figure 3-7: Average solar concentration ratio (a) and intercept factor (b) as functions of the dimensionless target width w_{target}/f, for optimized arc-spline concentrators with $n_{arc} = 2$ to 5 arcs per mirror wing, and for an ideal parabolic concentrator.

n_{arc}	C_{peak}	$C_{average}$	γ
2	83.8	67.3	0.748
3	175.8	83.8	0.931
4	208.1	87.6	0.974
5	217.2	88.0	0.977
parabola	229.9	88.6	0.985

Table 3-3: Peak solar concentration ratio C_{peak}, average solar concentration ratio $C_{average}$, and intercept factor γ on a 0.1m wide target, for optimized arc-spline concentrators with n_{arc} = 2 to 5 arcs per mirror wing, and for an ideal parabolic concentrator.
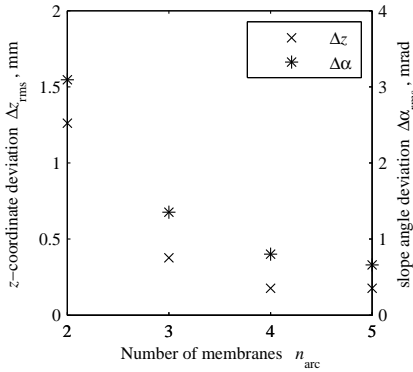

Figure 3-8: rms-z-coordinate difference Δz_{rms}, and rms-slope angle difference $\Delta\alpha_{rms}$ of the optimized arc-spline profile compared to the reference parabola, as a function of the number of arcs n_{arc} in the arc-spline.

3.2.2 Membrane pressure deviations

Figure 3-9 and Figure 3-10 show the influence of deviations δp of membrane pressures p_i, $i = 1, 2, ..., n_{arc} + 1$, from the design values p_i^{design} (given in Table 3-1) on the distribution of the solar concentration ratio at the focal plane, the average solar concentration ratio, and the intercept factor for an arc-spline with $n_{arc} = 4$. Criteria (ii) and (iii) are imposed to numerically determine the distorted arc-spline geometries. Results for a 0.1m wide target are listed in Table 3-4.
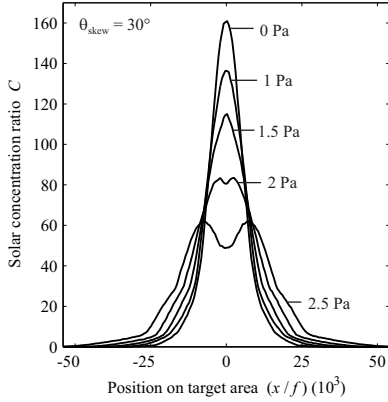
Figure 3-9: Distribution of the solar concentration ratio at the focal plane for various membrane pressure deviations δp, applied to p_i^{design} (given in Table 3-1); $\delta p = 0$ corresponds to the undistorted mirror shape.
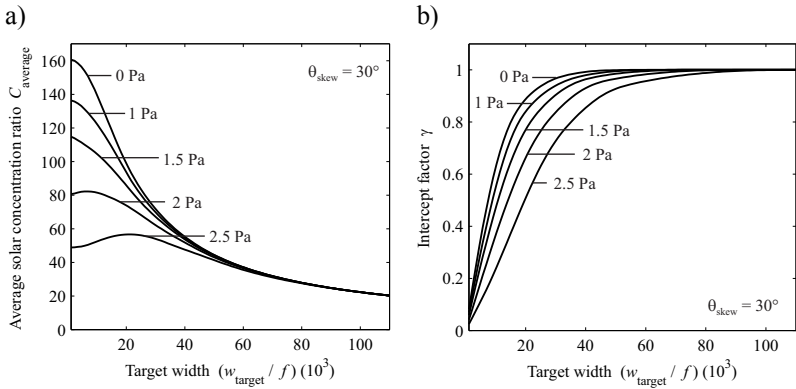

Figure 3-10: Average solar concentration ratio (a) and intercept factor (b) as functions of the dimensionless target width w_{target}/f, for various membrane pressure deviations δp, applied to p_i^{design} (given in Table 3-1); $\delta p = 0$ corresponds to the undistorted mirror shape.

$\delta p,[\mathrm{Pa}]$	C_{peak}	C_{average}	γ
0	160.9	74.8	0.960
1	136.4	72.5	0.930
1.5	115.0	69.4	0.890
2	83.5	63.9	0.819
2.5	62.2	54.7	0.702

Table 3-4: Peak solar concentration ratio C_{peak}, average solar concentration ratio C_{average}, and intercept factor γ on a 0.1m wide target for various membrane pressure deviations δp, applied to p_i^{design} (given in Table 3-1); $\delta p = 0$ corresponds to the undistorted mirror shape; $\theta_{\mathrm{skew}} = 30°$.

3.2.3 Membrane width deviations with design pressures

Figure 3-11 and Figure 3-12 show the influence of membrane width deviations Δw from the design value $w_{\mathrm{membrane}}^{\mathrm{reference,design}}$ on the distribution of the solar concentration ratio at the focal plane, the average solar concentration ratio, and the intercept factor for an arc-spline with $n_{\mathrm{arc}} = 4$. Design pressures p_i^{design} listed in Table 3-1 are applied. Distorted arc-spline geometries are found numerically by imposing criteria (ii) and (iii). Results for a 0.1m wide target are given in Table 3-5.

$\Delta w,[\mathrm{mm}]$	C_{peak}	C_{average}	γ
0	160.9	74.8	0.960
-1	133.1	66.4	0.852
-2	89.4	60.6	0.777
-3	66.1	53.2	0.683
-4	53.4	42.8	0.549
-5	40.9	32.5	0.417

Table 3-5: Peak solar concentration ratio C_{peak}, average solar concentration ratio C_{average}, and intercept factor γ on a 0.1m wide target for various membrane width deviations $\Delta w = -5 \div -1\mathrm{mm}$ from the design value $w_{\mathrm{membrane}}^{\mathrm{reference,design}}$; $\Delta w = 0$ corresponds to the undistorted mirror shape; design pressures p_i^{design} listed Table 3-1 are applied.
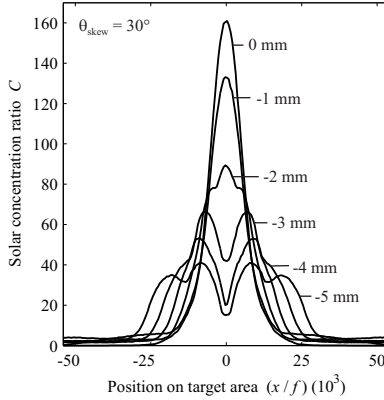
Figure 3-11: Distribution of the solar concentration ratio at the focal plane for various membrane width deviations $\Delta w = -5 \div -1\,\text{mm}$ from the design value $w_{membrane}^{reference,design}$; $\Delta w = 0$ corresponds to the undistorted mirror shape; design pressures p_i^{design} listed in Table 3-1 are applied.

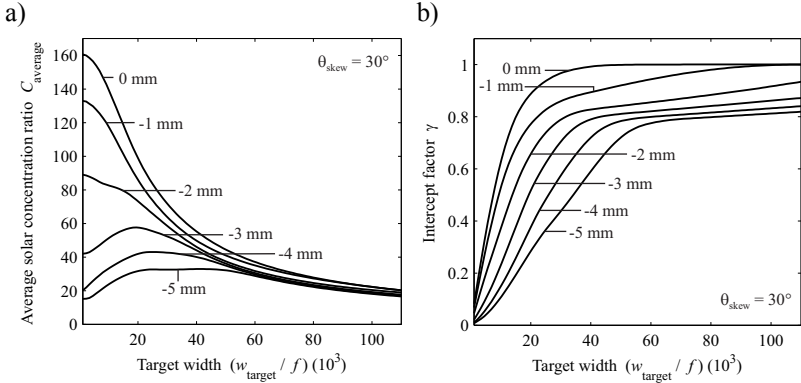a)   b)

Figure 3-12: Average solar concentration ratio (a) and intercept factor (b) as functions of the dimensionless target width w_{target}/f, for various membrane width deviations $\Delta w = -5 \div -1\,\text{mm}$ from the design value $w_{membrane}^{reference,design}$; $\Delta w = 0$ corresponds to the undistorted mirror shape; design pressures p_i^{design} listed in Table 3-1 are applied.

3.2.4 Membrane width deviations with corrected pressures

As long as $\Delta w < 1.63$ mm, the optimum arc-spline mirror geometry can be restored via adjustment of the pressure difference over each mirror membrane, thereby changing the membrane's elastic elongation. The corrected pressure difference $\Delta p_i^{\text{corrected}}$ to be applied over mirror membrane i is calculated from:

$$\Delta p_i^{\text{corrected}} = \left(p_i^{\text{corrected}} - p_{i+1}^{\text{corrected}} \right) = \Delta p_i^{\text{design}} + \ldots$$

$$\frac{E_{\text{membrane}} \cdot d_{\text{membrane}} \cdot w_{\text{membrane},i}^{\text{nominal,design}}}{R_{S,j=i}\left(1+\varepsilon_{\text{th}}\right)\cdot\left(1+\varepsilon_\varphi\right)} \left[\frac{1}{w_{\text{membrane}}^{\text{reference,design}} + \Delta w} - \frac{1}{w_{\text{membrane}}^{\text{reference,design}}} \right] \quad (3.27)$$

where ε_{th} and ε_φ are the thermal and hygroscopic membrane expansion, respectively. For $\Delta w = -5 \div +1\,\text{mm}$ the corrected membrane pressures $p_i^{\text{corrected}}$, $i = 1, 2, \ldots, n_{\text{arc}}$ ($p_5 = 0$ Pa in all cases) are plotted in Figure 3-13. For $\Delta w > 1.63$ mm the optimum arc-spline geometry cannot be restored, and criteria (i) and (iii) are imposed to numerically determine the pressures that yield the best possible arc-spline shape obtainable with the given membrane widths. Figure 3-14 and Figure 3-15 show the influence of width deviations $\Delta w = 2 \div 5\,\text{mm}$ from the design value $w_{\text{membrane}}^{\text{reference,design}}$ on the distribution of the solar concentration ratio at the focal plane, the average solar concentration ratio, and the intercept factor for an arc-spline with $n_{\text{arc}} = 4$. Results on a 0.1m wide target are listed in Table 3-6. Optimized pressures p_i applied are listed in Table 3-7.
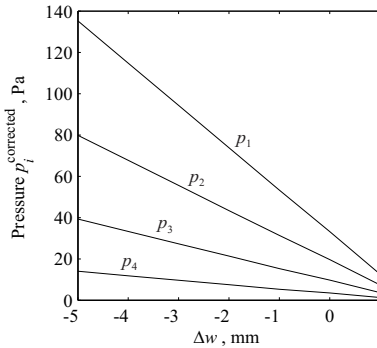

Figure 3-13: Membrane pressures $p_i^{\text{corrected}}$ to be applied in case that the width $w_{\text{membrane}}^{\text{reference}}$ of each mirror membrane deviates by $\Delta w = -5 \div 1\text{mm}$ from the design value $w_{\text{membrane}}^{\text{reference,design}}$; $p_5^{\text{corrected}} = 0$.
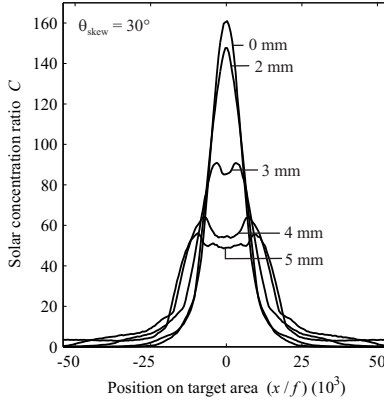
Figure 3-14: Distribution of the solar concentration ratio at the focal plane for various membrane width deviations $\Delta w = 2 \div 5 \text{mm}$ from the design value $w_{\text{membrane}}^{\text{reference,design}}$; $\Delta w = 0$ corresponds to the undistorted mirror shape; optimized pressures p_i listed in Table 3-7 are applied.
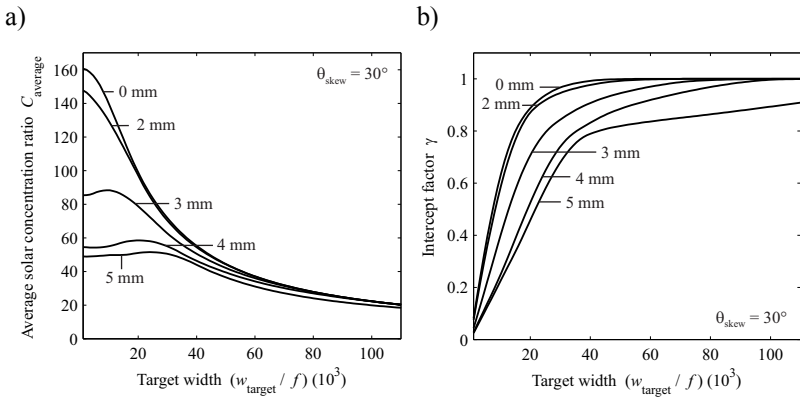
a)   b)

Figure 3-15: Average solar concentration ratio (a), and intercept factor (b) as functions of the dimensionless target width w_{target}/f, for various membrane width deviations $\Delta w = 2 \div 5 \text{mm}$ from the design value $w_{\text{membrane}}^{\text{reference,design}}$; $\Delta w = 0$ corresponds to the undistorted mirror shape; optimized pressures p_i listed in are applied.

$\Delta w, [\text{mm}]$	C_{peak}	C_{average}	γ
0	160.9	74.8	0.960
2	147.6	73.2	0.939
3	90.9	64.8	0.832
4	64.3	55.9	0.717
5	56.1	50.9	0.653

Table 3-6: Peak concentration C_{peak}, average concentration , and intercept factor γ on a 0.1m wide target for various membrane width deviations $\Delta w = 2 \div 5\text{mm}$ from the design value C_{average} $w_{\text{membrane}}^{\text{reference,design}}$; $\Delta w = 0$ corresponds to the undistorted mirror shape; optimized pressures p_i listed in Table 3-7 are applied.

$\Delta w, [\text{mm}]$	p_1	p_2	p_3	p_4
2	5.02	3.43	1.64	0.60
3	5.00	3.45	2.05	0.67
4	5.01	4.38	2.41	1.02
5	5.11	4.61	2.05	0.71

Table 3-7: Optimized membrane pressures to be applied when mirror membrane widths deviate by $\Delta w = 2 \div 5\text{mm}$ from the design value $w_{\text{membrane}}^{\text{reference,design}}$; lower limit for p_1 of 5 Pa has been imposed; pressure units: Pa.

3.2.5 Structural deformations

The longitudinal girders bend due to gravitational forces and tensile forces exerted by the spanned membranes, as shown in Figure 3-16 for one of the lateral girders. This bending causes distortion to the arc-spline shape. All forces are assumed to act at the center of gravity G of the girder profiles. Torsion is omitted from consideration. Imposing fixed-ends boundary conditions, the displacement vector $\boldsymbol{u}(y)$ of the girder's center line is described by:

$$\boldsymbol{u}(y) = \begin{cases} u_2 = \dfrac{|\boldsymbol{F}_{\text{resultant}}|}{24 l_{\text{girder}} E_{\text{concrete}} I_3} y^2 \left(l_{\text{girder}} - y\right)^2 \cdot e_{M_{\text{bending},3}} \\[2ex] u_3 = -\dfrac{|\boldsymbol{F}_{\text{resultant}}|}{24 l_{\text{girder}} E_{\text{concrete}} I_2} y^2 \left(l_{\text{girder}} - y\right)^2 \cdot e_{M_{\text{bending},2}} \end{cases} \quad \text{for } 0 \le y \le l_{\text{girder}}$$
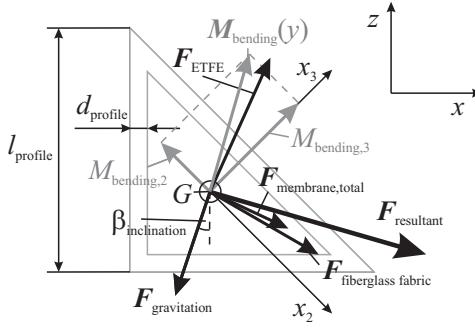
(3.28)

Figure 3-16: Forces (black) and moments (gray) acting on the lateral longitudinal girders with equilateral triangular hollow profile: F_{ETFE}: force exerted by ETFE-membrane, $F_{\text{gravitation}}$: gravitational force, $F_{\text{membrane,total}}$: force exerted by all mirror membranes, $F_{\text{fiberglass}}$: force exerted by fiberglass fabric, $F_{\text{resultant}}$: resultant force, x_2, x_3: principal directions of girder profile, M_{bending}: bending moment, $\beta_{\text{inclination}}$: concentrator inclination; G: center of gravity.

where $F_{\text{resultant}}$ is the resultant force, $\hat{e}_{M_{\text{bending}}} = \left(e_{M_{\text{bending},2}}, e_{M_{\text{bending},3}} \right)$ is the direction of bending moment M_{bending} with respect to principal directions (x_2, x_3), l_{girder} is the girder length, E_{concrete} is the Young's modulus of the concrete, and I_2 and I_3 are the moments of inertia with respect to (x_2, x_3).

Girder deflection $|u|$ is shown in Figure 3-17 as a function of the position along the girder axis, for the girder parameters of Table 3-8 and concentrator inclination $\beta_{\text{inclination}}$ = 30°. Legends "lower", "central", and "upper" refer to the positions of the longitudinal girders with respect to ground level. While weight force and membrane tensile forces tend to compensate each other in case of the lower – closer to the ground – lateral girder, they tend to add up in case of the upper girder, resulting in larger girder deformations. Maximum displacements $u_{\text{max}} = u\left(y = l_{\text{girder}}/2 \right)$ of the lateral girders are plotted in Figure 3-18a for $\beta_{\text{inclination}}$ in the range 0° to 60°. Maximum displacement $|u|_{\text{max}}$ as a function of girder length l_{girder} is plotted in Figure 3-18b for $\beta_{\text{inclination}}$ =30°. The distribution of the solar concentration ratio, the average solar concentration ratio, and the intercept factor are shown in Figure 3-19 and Figure 3-20, for the arc-spline that

45

results when clamping points P_1, $P_{1,j}$, $j = 2, 3, ..., n$, and P_{n+1} are displaced by u_{max} of the corresponding girder (calculated from Eq. (3.28) with parameters in Table 3-8). Criteria (ii) and (iii) are imposed to numerically determine the distorted arc-spline geometries. Design membrane pressures p_i^{design} are applied (Table 3-1). The parameter is the girder length $l_{girder} = 8 \div 12$ m.
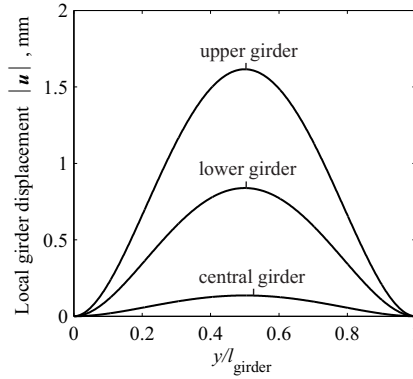

Figure 3-17: Deflection of lateral and central longitudinal girders as a function of position along the girder for $\beta_{inclination} = 30°$; girder parameters of Table 3-8 are used.

concrete density, $\left[kg/m^3 \right]$	2000
young's modulus of concrete $E_{concrete}$, $\left[N/m^2 \right]$	30E9
lateral girder profile side length, $\left[m \right]$	0.5
lateral girder profile wall thickness, $\left[m \right]$	70E-3
central girder profile side length, $\left[m \right]$	2.062
central girder profile wall thickness, $\left[m \right]$	40E-3
baseline girder length l_{girder}, $\left[m \right]$	10

Table 3-8: Girder parameters.

a)

b)
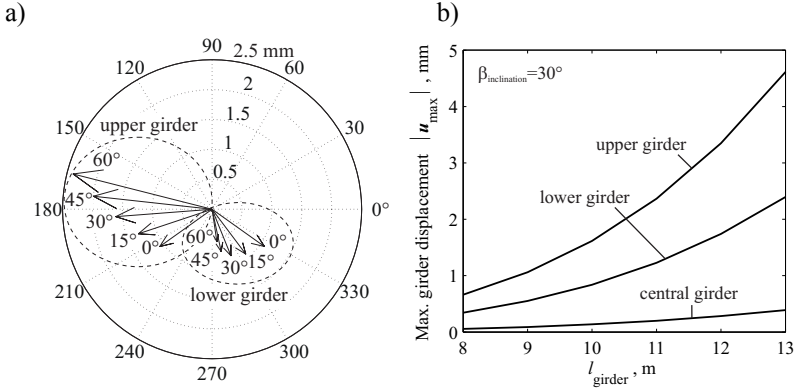
Figure 3-18: Displacement vector $\boldsymbol{u}_{\max} = \boldsymbol{u}\left(y = l_{\text{girder}}/2\right)$ of lateral longitudinal girders as a function of concentrator inclination $\beta_{\text{inclination}}$; b) maximum girder displacements $\left|\boldsymbol{u}_{\max}\right|$ as a function of girder length l_{girder} for $\beta_{\text{inclination}}$ =30°; girder parameters of Table 3-8 are used.
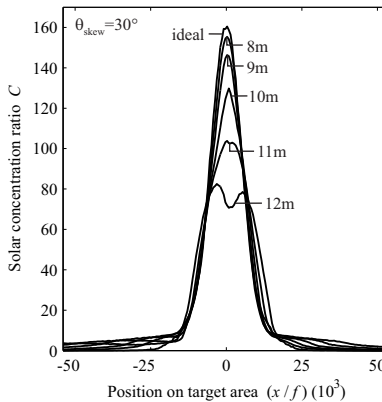

Figure 3-19: Distribution of the solar concentration ratio at the focal plane for deflections of the longitudinal girders by $\boldsymbol{u}_{\max}$, at $\beta_{\text{inclination}} = 30°$; the parameter is the girder length $l_{\text{girder}} = 8 \div 12$ m; girder parameters of Table 3-8 are used.

Figure 3-20: Average solar concentration ratio (a), and intercept factor (b) as functions of the dimensionless target width w_{target}/f, for deflections of the longitudinal girder by $\boldsymbol{u}_{\max}$, at $\beta_{\text{inclination}} = 30°$; the parameter is the girder length $l_{\text{girder}} = 8 \div 12$ m; girder parameters of Table 3-8 are used.
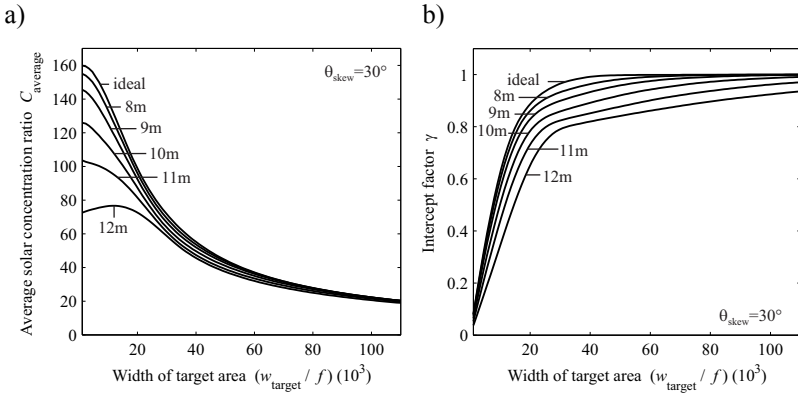
3.3 Experimental Validation

3.3.1 Parameter identification

Mirror surface points are measured on a 1.5m-long axial section of the concentrator prototype with a Leica TS30 coordinate measurement system (accuracy: 1mm). Nominal prototype dimensions are given in Table 3-1. Concentrator parameters P_1, $P_{1,j}$, $j = 2,3,...,n_{\text{arc}}$, $P_{n_{\text{arc}}+1}$, and $w_{\text{membrane},i}^{\text{reference}}$, $i = 1,2,...,n_{\text{arc}}$, are determined via least-squares optimization by simultaneously minimizing:

$$\Delta z_{\text{AS,rms}} = \frac{1}{n_{\text{cases}}} \cdot \sum_{i_{\text{cases}}=1}^{n_{\text{cases}}} \sqrt{\frac{1}{n_{\text{points}}} \cdot \sum_{i_{\text{points}}=1}^{n_{\text{points}}} \left[z_{\text{AS},i_{\text{cases}},i_{\text{points}}}^{\text{calculated}} \left(x_{i_{\text{points}}} \right) - z_{\text{AS},i_{\text{cases}},i_{\text{points}}}^{\text{measured}} \left(x_{i_{\text{points}}} \right) \right]^2}$$

(3.29)

$$\Delta p_{\text{rms,2}} = \sqrt{\frac{1}{n_{\text{cases}} \cdot (n_{\text{arc}} - 1)} \cdot \sum_{i_{\text{cases}}=1}^{n_{\text{cases}}} \sum_{i=2}^{n_{\text{arc}}} \left[p_{i,i_{\text{cases}}}^{\text{calculated}} - p_{i,i_{\text{cases}}}^{\text{measured}} \right]^2} \qquad (3.30)$$

$$\Delta w_{\text{rms,2}} = \sqrt{\frac{1}{n_{\text{cases}} \cdot n_{\text{arc}}} \cdot \sum_{i_{\text{cases}}=1}^{n_{\text{cases}}} \sum_{i=1}^{n_{\text{arc}}} \left[w_{\text{membrane},i,i_{\text{cases}}}^{\text{reference,calculated}} - w_{\text{membrane},i,\text{average}}^{\text{reference,calculated}} \right]^2} \quad (3.31)$$

48

where n_{cases} is the number of mirror measurements and n_{points} is the number of measured mirror points in each measurement ($120 \div 260$ points per set). $z_{\text{AS},i_{\text{cases}},i_{\text{points}}}^{\text{calculated}}$ is calculated from Eqs. (3.4) to (3.8), with free parameters $\boldsymbol{v}$. $p_{i,i_{\text{cases}}}^{\text{calculated}}$ are the membrane pressures calculated from Eqs. (3.22) and (3.24), and $p_{i,i_{\text{cases}}}^{\text{measured}}$, $i = 2,3,...,n_{\text{arc}}$, are the membrane pressures applied during mirror measurement i_{cases}. Average membrane widths $w_{\text{membrane},i,\text{average}}^{\text{reference,calculated}}$ are calculated from:

$$w_{\text{membrane},i,\text{average}}^{\text{reference,calculated}} = \frac{1}{n_{\text{cases}}} \sum_{i_{\text{cases}}=1}^{n_{\text{cases}}} w_{\text{membrane},i,i_{\text{cases}}}^{\text{reference,calculated}} \qquad (3.32)$$

and are considered as the "true" values. Residuals of the concentrator parameter identification are listed in Table 3-9.

	north	south
$\Delta z_{\text{AS,rms}}$, $[\text{mm}]$	1.17	1.34
$\Delta p_{\text{rms,2}}$, $[\text{Pa}]$	1.28	1.73
$\Delta w_{\text{rms,2}}$, $[\text{mm}]$	0.897	0.594

Table 3-9: Residuals of the concentrator parameter identification for north and south mirror wings; $n_{\text{cases}} = 3$; north mirror: $n_{\text{arc}} = 4$, south mirror: $n_{\text{arc}} = 3$.

3.3.2 Solar flux distribution

Solar radiative flux at the focal plane is measured as described in section 2.4. The MC simulation model is validated by comparing measured and simulated solar concentration ratio on a 50mm-long 230mm-wide region of interest (ROI) on the target, subdivided into 10mm x 5mm segments. The agreement is characterized by the standard covariance coefficient $c|_{\text{ROI}}$, and the difference in incident radiative power $\Delta Q|_{\text{ROI}}$. The mirror shapes used in the simulations are calculated based on the concentrator parameters, and the actual pressure settings and operating conditions $\left(T_{\text{ambient}}, \varphi_{\text{ambient}}\right)$ during the flux measurements. Directional spectral transmittance of the ETFE-membrane, $T'_{r,\text{ETFE},\lambda}$, is calculated for each ray based on directional spectral reflectivity $\rho'_{\text{ETFE},\lambda}$, directional spectral transmissivity $\tau'_{\text{ETFE},\lambda}$, and spectral refractive index $n_{\text{ETFE},\lambda}$. $T_{r,\text{ETFE}}$ is the fraction of incident solar power

transmitted through the ETFE-membrane, calculated by averaging $T'_{r,\text{ETFE},\lambda}$ over all rays. Experimentally determined total reflectivity of the mirror membranes is 92% (chapter 2). Validation results are shown in Figure 3-21 and quantified in Table 3-10.
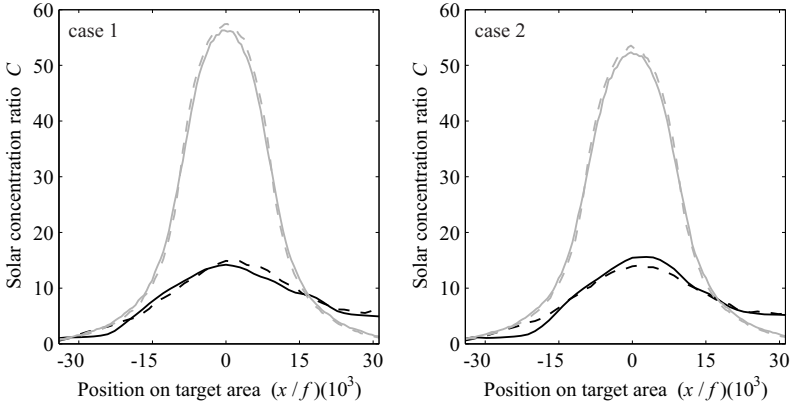

Figure 3-21: Concentrator model validation: measured (black solid curves) vs. simulated (black dashed curves) distributions of the solar concentration ratio on the target; for comparison the distributions for an ideal arc-spline concentrator with 4 arcs per mirror wing (gray solid curves) and for an ideal parabolic concentrator (gray dashed curves) are shown; $T_{r,\text{ETFE}} = 1$, $\rho_{\text{mirror}} = 1$ for the ideal cases.

case	1	2
date	10/08/10	10/08/10
local time	17:45:15	17:51:03
$DNI, \left[\text{W/m}^2 \right]$	461	455
$\theta_{\text{skew}}, [\text{deg}]$	60.0	61.2
$T_{r,\text{ETFE}}$	0.797	0.791
$c\big|_{\text{ROI}}$	0.982	0.990
$\Delta Q\big|_{\text{ROI}}, [\%]$	-4.08	0.45

Table 3-10: Validation of the Monte Carlo ray-tracing simulation model by comparing simulated and measured distributions of the solar concentration ratio at the focal plane.

3.4 Summary and Conclusions

A novel solar trough concentrator has been designed, modeled, and fabricated. The concentrator is based on a multilayer polymer mirror membrane mounted on a rotatable concrete structure. The parabolic shape of each mirror wing can be well approximated with an arc-spline consisting of 4 arcs built with 4 mirror membranes. During operation, membrane pressures should be maintained within ±1Pa of their nominal values to avoid significant broadening of the flux distribution. Without pressure correction, membrane widths should be manufactured to ±1mm accuracy (±0.02% of nominal width), and operating temperature and humidity should be kept within a few percent of their design values. If all membrane widths are smaller than the design value, the optimum mirror shape is still achievable by increasing the membrane pressures by the factor $(1 - 0.62 \cdot \Delta w [\mathrm{mm}])$ compared to the design pressures. Allowable negative membrane width deviations depend on the capacity of the blowers that span the membranes. If the mirror membrane widths are larger than the design value, the optimum arc-spline profile can generally not be achieved and optimum pressures are to be recalculated. Positive membrane width deviations should not exceed 2mm. Deflections of the longitudinal concrete girders caused by gravitational forces and forces exerted by the spanned membranes strongly increase with girder length. Maximum girder deflections should be kept below 1mm. With girder parameters in Table 3-8, this limits the allowable girder length to 9m. Increase of membrane width (nominal width: 4.89m) due to thermal and hygroscopic expansion are 0.83mm per 10°C, and 0.29mm per 10% change in relative humidity. Membranes are to be dimensioned for maximum expected operating temperature T_{ambient} and humidity $\varphi_{\mathrm{ambient}}$, and elongated elastically at lower T_{ambient} and $\varphi_{\mathrm{ambient}}$ by increasing the membrane pressures. Manufactured membrane lengths should additionally allow for creeping (slow plastic elongation of the membranes due to tensile forces). Model validation was accomplished with experimental measurements.

Highest measured peak solar flux concentration at the focal plane of a 45m-long full-scale prototype concentrator was 18.9, measured at 62.6° solar incidence angle, corresponding to 39% of the predicted value for the

ideal concentrator of 47.9. The concentrator performance is reduced by: 1) transmission and reflection losses, 2) errors of the widths of the intalled mirror membranes, and 3) inaccurate inflation pressures applied to the membranes.

4   Solar Trough Concentrators for CPV[1]

The integral methodology used in chapter 2 to derive the *SM* profile can be further applied to design concentrators that are suitable for concentrated photovoltaics (CPV). This chapter deals with the design and analysis of 1-stage and 2-stage solar trough concentrators for CPV at moderate mean solar flux concentration ratios of up to $C = 50$.

While thermal receivers primarily require high solar flux concentration to minimize heat losses, the efficiency of PV-cells strongly depends on the uniformity of the incident radiative flux. Hence, the CPV-concentrators are tailor-designed to achieve a uniform "pill-box" radiative flux distribution over a flat rectangular target area at the focal plane, to minimize Joule effect power losses in the cell. [23],[24] The exact concentrator profiles are analytically derived, and the Monte Carlo (MC) ray-tracing technique is applied to study the effect of the sunshape and mirror imperfections on the uniformity and spillage.

4.1   One-Stage CPV-Trough Concentrator

The 1-stage CPV-trough concentrator consists of two separate symmetrical linear trough mirrors and one linear flat rectangular target area. The concentrator is designed such that the right half of the target is irradiated by the right mirror wing, and the left half of the target is irradiated by the left mirror wing. Alternatively, the mirrors could be designed such that each mirror wing irradiates the entire target. The derivation of the mirror profile is done for the right half of the concentrator, shown in Figure 4-1, with symmetry axis y.

---

[1] Material in this chapter has been published in: Bader R., Steinfeld A., "A Solar Trough Concentrator for Pill-Box Flux Distribution over a CPV Panel", *ASME Journal of Solar Energy Engineering*, Vol. 132, pp. 014501, 2010.
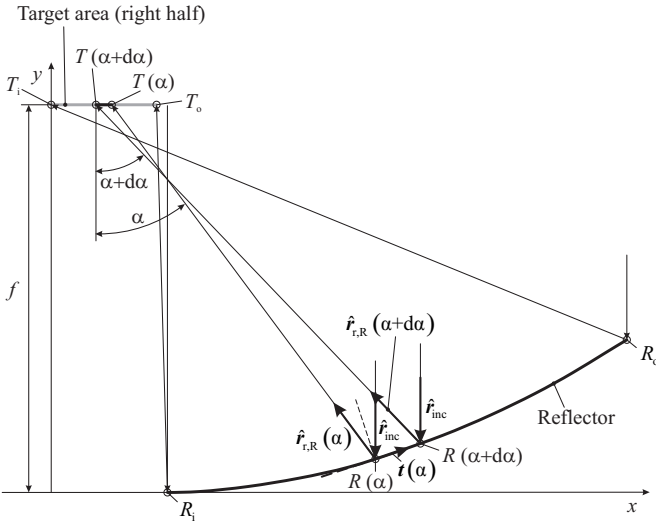
Figure 4-1: Right wing of 1-stage CPV-trough concentrator R, with boundary points R_i and R_o; right half of target area T (gray) at focal distance f, with center point T_i and boundary point T_o.

A generic ray is incident on the mirror at $R(\alpha)$. Its specular reflection strikes the target at $T(\alpha)$. Thus, the parametric equation of the mirror is given by:

$$R(\alpha) = T(\alpha) - k(\alpha) \cdot \hat{\boldsymbol{r}}_{\mathrm{r,R}} \tag{4.1}$$

where

$$\hat{\boldsymbol{r}}_{\mathrm{r,R}} = (-\sin\alpha, \cos\alpha) \tag{4.2}$$

denotes the unit vector along the direction of the reflected ray, and $k(\alpha)$ is a scalar scaling function which is to be determined. The independent variable α runs from α_i to α_o where:

$$T(\alpha_\mathrm{i}) = T_\mathrm{o} \tag{4.3}$$

is the right boundary of the target,

$$T(\alpha_\mathrm{o}) = T_\mathrm{i} \tag{4.4}$$

is the center point of the target,

$$R(\alpha_i) = R_i \tag{4.5}$$

is the inner boundary point of the mirror, and

$$R(\alpha_o) = R_o \tag{4.6}$$

is the outer boundary point of the mirror. The mirror profile $R(\alpha)$ is designed such that the solar radiation – which is incident onto the projected mirror area with uniform distribution – is transformed into a uniform (concentrated) distribution on the target. The incident sunrays are assumed to be perfectly parallel, i.e. their incidence direction is assumed to be $\hat{r}_{inc} = (0, -1)$ (real sunrays subtend a solid angle of $\theta_{sun} \cong 6.72 \cdot 10^{-5}$ sr around direction $\hat{r}_{inc}$). Uniform radiative flux on the target area is achieved if (Figure 4-1):

$$\frac{R_x(\alpha + d\alpha) - R_x(\alpha)}{T_x(\alpha) - T_x(\alpha + d\alpha)} = \frac{R_x(\alpha + d\alpha) - R_x(\alpha)}{-(T_x(\alpha + d\alpha) - T_x(\alpha))} = C = \frac{R_{o,x} - R_{i,x}}{T_{o,x} - T_{i,x}} \tag{4.7}$$

In the limit of $d\alpha \to 0$:

$$\lim_{d\alpha \to 0} \left\{ \frac{R_x(\alpha + d\alpha) - R_x(\alpha)}{-(T_x(\alpha + d\alpha) - T_x(\alpha))} \right\} = \frac{dR_x(\alpha)}{-dT_x(\alpha)} = C \tag{4.8}$$

Integrating from α_i to α ($\alpha_i < \alpha \le \alpha_o$):

$$\int_{R_{i,x}}^{R_x(\alpha)} dR_x(\alpha) = -C \cdot \int_{T_{o,x}}^{T_x(\alpha)} dT_x(\alpha) \tag{4.9}$$

yields:

$$R_x - R_{i,x} = -C(T_x - T_{o,x}) \tag{4.10}$$

or:

$$\frac{R_x - R_{i,x}}{T_x - T_{o,x}} = -C = -\frac{R_{o,x} - R_{i,x}}{T_{o,x} - T_{i,x}} \tag{4.11}$$

Rearranging and setting $T_{i,x} = 0$ yields:

$$\frac{R_x - R_{i,x}}{R_{o,x} - R_{i,x}} = -\frac{T_x - T_{o,x}}{T_{o,x}} = 1 - \frac{T_x}{T_{o,x}} \tag{4.12}$$

or:

$$\frac{T_x}{T_{o,x}} = 1 - \frac{R_x - R_{i,x}}{R_{o,x} - R_{i,x}} \tag{4.13}$$

Inserting Eqs. (4.2) and (4.13) into Eq. (4.1), setting $T_y = f$, and solving for R yields:

$$R(\alpha) = \begin{cases} R_x = \dfrac{\left(R_{o,x} - R_{i,x}\right) \cdot k(\alpha) \cdot \sin(\alpha) + T_{o,x} \cdot R_{o,x}}{R_{o,x} - R_{i,x} + T_{o,x}} \\[2ex] R_y = f - k(\alpha) \cdot \cos\alpha \end{cases} \tag{4.14}$$

Specular reflection on the concentrator requires that:

$$\hat{r}_{inc} \cdot t = \hat{r}_{r,R} \cdot t \tag{4.15}$$

where t is the tangent vector to the concentrator profile in point $R(\alpha)$:

$$t = \begin{pmatrix} t_x \\ t_y \end{pmatrix} = \frac{\partial R}{\partial \alpha} = \begin{pmatrix} \left(\dfrac{R_{o,x} - R_{i,x}}{R_{o,x} - R_{i,x} + T_{o,x}}\right)\left(k(\alpha) \cdot \cos\alpha + k'(\alpha) \cdot \sin\alpha\right) \\[2ex] k(\alpha) \cdot \sin\alpha - k'(\alpha) \cdot \cos\alpha \end{pmatrix} \tag{4.16}$$

Substituting $\hat{r}_{inc} = (0, -1)$, Eq. (4.2) and Eq. (4.16) into Eq. (4.15) yields the following first-order ordinary differential equation:

$$\frac{k'(\alpha)}{k(\alpha)} = \frac{\left(R_{o,x} - R_{i,x} + T_{o,x}(1 + \cos\alpha)\right) \cdot \tan\alpha/2}{R_{o,x} - R_{i,x} + T_{o,x} \cdot \cos\alpha} \tag{4.17}$$

Setting $R_{i,y} = 0$, and using $T_{o,y} = f$, Eq. (4.17) is subject to the initial value:

$$k(\alpha_i) = \sqrt{\Delta x^2 + f^2} \tag{4.18}$$

at

$$\alpha_i = \tan^{-1}\left(\frac{\Delta x}{f}\right) \tag{4.19}$$

where $\Delta x = R_{i,x} - T_{o,x}$ is the x-distance between target outer boundary point and mirror inner boundary point. Solving Eq. (4.17) with Eqs. (4.18) and (4.19) analytically for $k(\alpha)$ results in: [25]

$$k(\alpha) = \sqrt{\Delta x^2 + f^2} \left(\frac{-\dfrac{T_{o,x}}{\sqrt{(\Delta x/f)^2 + 1}} + R_{i,x} - R_{o,x}}{R_{i,x} - R_{o,x} - T_{o,x} \cdot \cos(\alpha)} \right)^{\frac{T_{o,x}}{T_{o,x} + R_{i,x} - R_{o,x}}} \cdots$$

$$\cdot \left(\frac{\cos\left(\dfrac{1}{2} \tan^{-1}\left(\dfrac{\Delta x}{f} \right) \right)}{\cos(\alpha/2)} \right)^{\frac{2(R_{i,x} - R_{o,x})}{T_{o,x} + R_{i,x} - R_{o,x}}} \tag{4.20}$$

Finally, substituting Eq. (4.20) into Eq. (4.14) yields the explicit parametric equations of the exact mirror profile (the free parameter is α):

$$R_x(\alpha) = \frac{1}{R_{o,x} - R_{i,x} + T_{o,x}} \cdot \Big[R_{o,x} T_{o,x} + (R_{o,x} - R_{i,x}) \cdot \sin(\alpha) \ldots$$

$$\cdot \sqrt{\Delta x^2 + f^2} \cdot \left(\frac{-\dfrac{T_{o,x}}{\sqrt{(\Delta x/f)^2 + 1}} + R_{i,x} - R_{o,x}}{R_{i,x} - R_{o,x} - T_{o,x} \cdot \cos(\alpha)} \right)^{\frac{T_{o,x}}{T_{o,x} + R_{i,x} - R_{o,x}}} \cdots \quad (4.21)$$

$$\cdot \left(\frac{\cos\left(\dfrac{1}{2} \tan^{-1}\left(\dfrac{\Delta x}{f} \right) \right)}{\cos(\alpha/2)} \right)^{\frac{2(R_{i,x} - R_{o,x})}{T_{o,x} + R_{i,x} - R_{o,x}}} \Bigg]$$

$$R_y(\alpha) = f - \cos\alpha \cdot \sqrt{\Delta x^2 + f^2} \cdots$$

$$\cdot \left(\frac{-\dfrac{T_{o,x}}{\sqrt{(\Delta x/f)^2 + 1}} + R_{i,x} - R_{o,x}}{R_{i,x} - R_{o,x} - T_{o,x} \cdot \cos(\alpha)} \right)^{\frac{T_{o,x}}{T_{o,x} + R_{i,x} - R_{o,x}}} \ldots \tag{4.22}$$

$$\cdot \left(\frac{\cos\left(\dfrac{1}{2} \tan^{-1}\left(\dfrac{\Delta x}{f} \right) \right)}{\cos(\alpha/2)} \right)^{\frac{2(R_{i,x} - R_{o,x})}{T_{o,x} + R_{i,x} - R_{o,x}}}$$

α_o is found iteratively from Eq. (4.21) by requiring that $R_x(\alpha_o) = R_{x,o}$. The mirror profile is shown in Figure 4-2a for the baseline geometrical parameters given in Table 4-1. Figure 4-2b shows the local distance in y-direction between the exact profile described by Eqs. (4.21) and (4.22), and

2nd-order and 5th-order polynomial approximations to the profile. A 5th-order polynomial curve provides an excellent fit, while a parabolic curve is able to approximate the exact profile within ± 1 mm.

The mirror profiles for focal lengths f in the range of $3-7$ m and C in the range of $3-50$ are shown in Figure 4-3a and b, respectively, with the remaining parameters set to the baseline values given in Table 4-1.
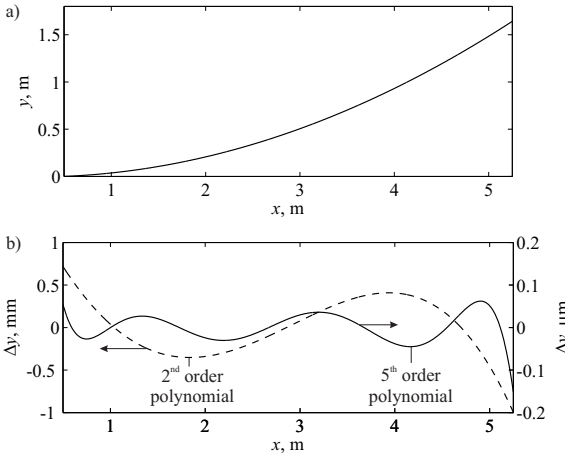

Figure 4-2: a) Exact right-wing profile of the 1-stage CPV-trough mirror for the geometrical parameters listed in Table 4-1; b) distance between exact and approximated profiles using 2nd-order and 5th-order polynomial functions.

$R_i, [\text{m}]$	$(0.5, 0)$
$R_{o,x}, [\text{m}]$	$(5.25, 1.64)$
$T_o, [\text{m}]$	$(0.173, 4)$
2nd-order curve fit	$y(x) = 6.39\text{E-}2x^2 - 2.13\text{E-}2x - 6.03\text{E-}3$
5th-order curve fit	$y(x) = 9.76\text{E-}7x^5 - 2.36\text{E-}5x^4 + 2.44\text{E-}5x^3$ $+ 6.47\text{E-}2x^2 - 2.38\text{E-}2x - 4.26\text{E-}3$

Table 4-1: Baseline geometrical parameters used in Figure 4-2, and 2nd-order and 5th-order polynomial approximations of the solar trough mirror profile.
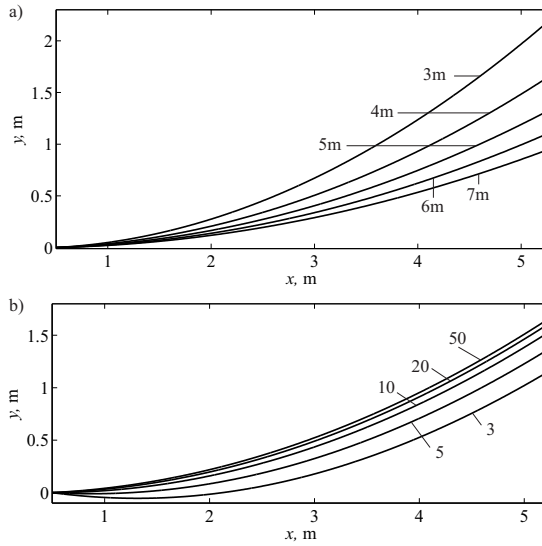
Figure 4-3: Mirror profiles for: a) focal lengths f in the range $3-7\,\text{m}$, b) solar concentration ratios C in the range 3-50. The remaining parameters are set to the baseline values of Table 4-1.

4.2 Two-Stage CPV-Trough Concentrator

Uniform radiative flux distribution on a flat rectangular target area may be obtained by combining two symmetrical circular-cylindrical primary mirrors R (e.g. obtained by spanning a mirror membrane with a differential pressure) with two symmetrical secondary mirrors S, whose custom shapes are yet to be determined. The right half of this concentrator design is shown schematically in Figure 4-4, with symmetry axis y. The concentrator is designed such that the right half of the target is irradiated by the right mirror wing, and the left half of the target is irradiated by the left mirror wing.

The secondary mirror profile can be described by:

$$S(\alpha) = \begin{pmatrix} O_x \\ O_y \end{pmatrix} + R_R \cdot \begin{pmatrix} \sin\alpha \\ -\cos\alpha \end{pmatrix} + k(\alpha) \cdot \begin{pmatrix} -\sin 2\alpha \\ \cos 2\alpha \end{pmatrix} \qquad (4.23)$$

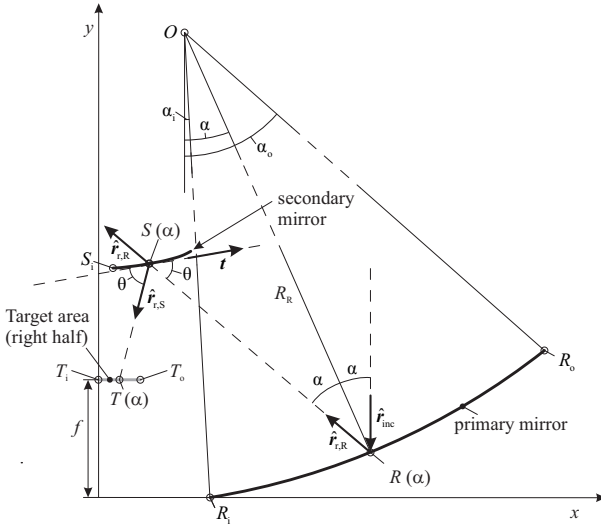where in the last term on the right-hand side:

Figure 4-4: Primary mirror R with circular profile combined with custom secondary mirror S to generate a uniform radiative flux distribution on a flat target area that is parallel to the $x-z$-plane at $y=f$; y is the axis of symmetry.

$$\hat{r}_{r,R}(\alpha) = \begin{pmatrix} -\sin 2\alpha \\ \cos 2\alpha \end{pmatrix} \tag{4.24}$$

is the ray travel direction after specular reflection in point $R(\alpha)$, and $k(\alpha)$ is a scaling function that remains to be determined. The ray travel direction between reflection point $S(\alpha)$ on the secondary mirror and incidence point $T(\alpha)$ on the target is given by:

$$\hat{r}_{r,S}(\alpha) = \frac{T(\alpha) - S(\alpha)}{\left| T(\alpha) - S(\alpha) \right|} \tag{4.25}$$

As in the case of the 1-stage CPV-concentrator (Eq. (4.11)), uniform radiative flux distribution on the target plane is achieved if:

$$\frac{dR_x(\alpha)}{dT_x(\alpha)} = -C = -\frac{R_{o,x} - R_{i,x}}{T_{o,x} - T_{i,x}} \tag{4.26}$$

for every α within α_i and $\alpha_o - d\alpha$, where C is the design concentration ratio. Integrating from α_i to α ($\alpha_i < \alpha \le \alpha_o$), setting $T_{i,x} = 0$, using $R_x(\alpha) = O_x + R_R \cdot \sin(\alpha)$, and rearranging, yields:

60

$$\frac{T_x}{T_{o,x}} = \frac{O_x + R_R \cdot \sin\alpha - R_{i,x}}{R_{o,x} - R_{i,x}} \tag{4.27}$$

Specular reflection on S is described by :

$$\hat{\boldsymbol{r}}_R \cdot \boldsymbol{t} = \hat{\boldsymbol{r}}_S \cdot \boldsymbol{t} \tag{4.28}$$

tangent vector $\boldsymbol{t}$ in point $S(\alpha)$ is found from Eq. (4.23):

$$\boldsymbol{t} = \frac{\partial S}{\partial \alpha} = R_R \begin{pmatrix} \cos\alpha \\ \sin\alpha \end{pmatrix} - 2k \begin{pmatrix} \cos 2\alpha \\ \sin 2\alpha \end{pmatrix} + k' \begin{pmatrix} -\sin 2\alpha \\ \cos 2\alpha \end{pmatrix} \tag{4.29}$$

By inserting Eq. (4.27) into Eq. (4.25), and inserting, Eq. (4.24), (4.25), and (4.29) into Eq. (4.28), the following first-order ordinary differential equation is found (sin and cos abbreviated by s and c):

$$k'(\alpha) = \frac{N}{D} \tag{4.30}$$

$$
\begin{aligned}
N = &-R_R c(2\alpha)s(\alpha) + R_R c(\alpha)s(2\alpha) + \\
&\frac{1}{C_2}\Big[R_R s(\alpha)\big(f - O_y + R_R c(\alpha) - k(\alpha)c(2\alpha)\big)\ldots \\
&-2k(\alpha)s(2\alpha)\big(f - O_y + R_R c(\alpha) - k(\alpha)c(2\alpha)\big)\ldots \\
&+R_R c(\alpha)C_1 - 2k(\alpha)c(2\alpha)C_1 \Big]
\end{aligned} \tag{4.31}
$$

$$
\begin{aligned}
D = &\; c^2(2\alpha) + s^2(2\alpha)\ldots \\
&-\frac{1}{C_2}\Big[c(2\alpha)\big(f - O_y + R_R c(\alpha) - k(\alpha)c(2\alpha)\big) + s(2\alpha)C_1 \Big]
\end{aligned} \tag{4.32}
$$

with:

$$C_1 = -O_x - R_R s(\alpha) + \frac{T_{o,x}\big(-O_x + R_{o,x} - R_R s(\alpha)\big)}{R_{o,x} - R_{i,x}} + k(\alpha)s(2\alpha) \tag{4.33}$$

and

$$C_2 = \Big[\big(f - O_y + R_R c(\alpha) - k(\alpha) \cdot c(2\alpha)\big)^2 + C_1^2\Big]^{0.5} \tag{4.34}$$

This equation can be integrated numerically from α_i to α_o, where:

$$\sin\alpha_i = \frac{R_{i,x} - O_x}{R_R} \tag{4.35}$$

and

$$\sin \alpha_{\text{o}} = \frac{R_{\text{o},x} - O_x}{R_{\text{R}}} \qquad (4.36)$$

and initial value $k(\alpha_{\text{i}}) = k_{\text{i}}$. $S_{\text{i},x}$ or $S_{\text{i},y}$ can be prescribed to calculate k_{i}. Prescribing $S_{\text{i},y}$ yields:

$$k_{\text{i}} = k(\alpha_{\text{i}}) = \frac{S_{\text{i},y} - R_{\text{i},y}}{\cos 2\alpha_{\text{i}}} \qquad (4.37)$$

where $r_{\text{r},\text{R},\text{i},y} = r_{\text{r},\text{R},y}(\alpha_{\text{i}}) = \cos(2\alpha_{\text{i}})$, and $S_{\text{i},x}$ is calculated from:

$$S_{\text{i},x} = O_x - k(\alpha_{\text{i}}) \cdot \sin 2\alpha_{\text{i}} \qquad (4.38)$$

Finally, substituting the result for $k(\alpha)$ into Eq. (4.23) yields the secondary mirror profile S shown in Figure 4-5a. Geometry parameters of the 2-stage CPV-concentrator are listed in Table 4-2. Figure 4-5b shows the y-distance of S to a linear regression line (dashed curve) and to a 5th-order polynomial curve fit (solid curve). Table 4-3 and Table 4-4 list the curve fit functions and goodness of fit statistics. [26]
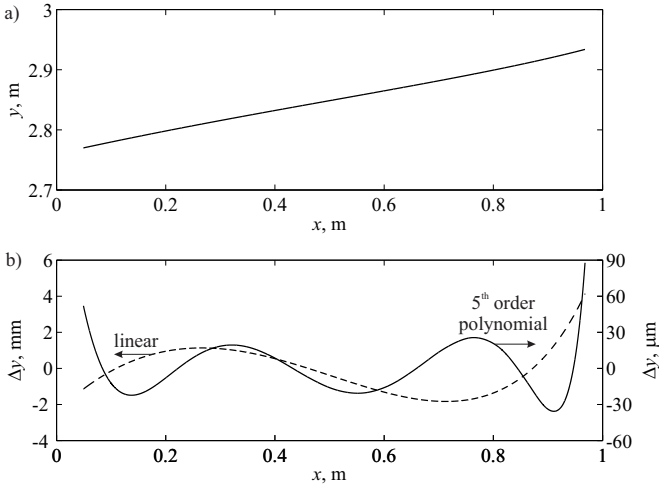

Figure 4-5: a) Profile of secondary mirror used in tandem with circular-cylindrical primary mirror to generate uniform radiative flux distribution on flat target area at $y = T_{\text{o},y}$; parameters listed in Table 4-2; b) distance between exact and approximated secondary mirror profiles, using linear and 5th-order polynomial curve fits.

R_i	(*1*; 0.1345)
R_o	(*4*; 1.235)
O	(*-0.55*; *9*)
R_R	*9*
S_i	(0.04938; *2.77*)
S_o	(0.9679, 2.934)
T_o	(*0.1; 1.5*)

Table 4-2: Parameters of the 2-stage concentrator geometry, in [mm] (values in italics are design parameters that have been prescribed).

linear curve fit	$y(x) = 1.726\text{E-}1x + 2.763$
R-square	0.9991
Adjusted R-square	0.9991

Table 4-3: Results of linear curve fit to secondary mirror profile.

5-th order polynomial curve fit	$y(x) = 5.689\text{E-}2x^5 - 9.98\text{E-}2x^4 + 1.173\text{E-}1x^3...$ $-9.956\text{E-}2x^2 + 2.065\text{E-}1x^1 + 2.76$
R-square	1
adjusted R-square	1

Table 4-4: Results of 5th-order polynomial curve fit to secondary mirror profile.

4.3 Ray-Tracing Analysis

For both 1- and 2-stage CPV-concentrators, solar radiative flux concentration $(C-)$ distributions at the target plane are investigated using the MC ray-tracing technique. Samples of 10^8 sunrays are used in each simulation run, with rays incident in $-y$-direction. Skew rays are not considered. Sunshape model [22] is used, with circumsolar ratio $CSR = 5\%$. Mirror imperfections are taken into account by Bivariate Chi Squared distributed surface orientation errors, with mode σ in the range of $2 \div 6$ mrad. [16] Ideal specular reflection is assumed, with reflectivity equal unity. The 1-stage concentrator profile is approximated in the simulations with the 5th-order polynomial curve fit given in Table 4-1. In case of the 2-

stage CPV-concentrator, Eq. (4.30) is integrated with 10^4 increments between α_i and α_o. The uniformity of the C-distributions on the target area is defined by:

$$U = \left|1 - C_{\text{peak}} / C_{\text{ave}}\right| \tag{4.39}$$

U defines the maximum allowable relative deviation of local to average flux concentration C_{ave} on the target area. Beside the uniformity, the intercept factor γ is to be optimized, defined as the ratio of radiative power incident on the target area of finite width to radiative power reflected by the (last) mirror. The width of the target area is adjusted in each case to match the region of the focal plane, where condition Eq. (4.39) is fulfilled. Radiation that misses the target area is spilled, thus lowering γ.

In Figure 4-6 the C-distributions at the target plane are plotted. In the ideal case of perfectly parallel incident radiation, pillbox distributions are obtained, verifying the correctness of the above derivations. Small artefacts in the center regions of the ideal pillbox distributions are due to the approximation of the concentrator shape with a polynomial in case of the 1-stage concentrator, and due to finite resolution of the numerically calculated secondary mirror profile in case of the 2-stage concentrator. For all real cases, C drops significantly at the center region.
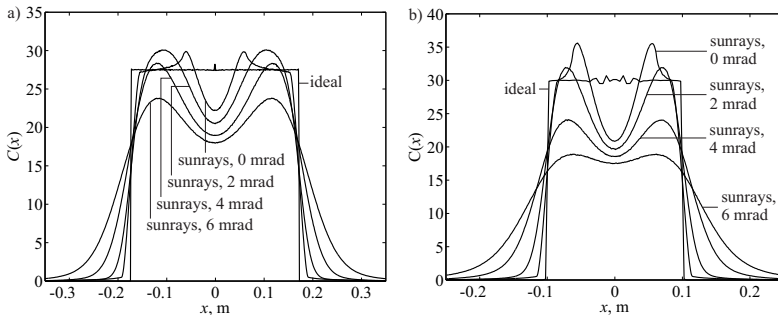

Figure 4-6: Focal flux distributions determined with MC ray-tracing for (a) 1-stage and (b) 2-stage CPV-trough concentrators, with ideal parallel incident radiation (denoted by ideal), and including the sunshape model [22] with $CSR = 5\%$ and $0 \div 6$ mrad surface errors.

To improve the uniformity at the center region of the $C-$distributions, the two concentrator sides are shifted toward each other, up to the relative position where γ becomes maximum for a prescribed value of U. Figure 4-7 shows the variation of the resulting intercept factor γ as a function of the uniformity U for the case of real sunrays and $0 \div 6$ mrad surface errors. For the ideal case of parallel rays and no surface errors, $U=1$ and $\gamma=1$. Higher intercept factors are obtained for the 1-stage than for the 2-stage concentrator, except for the case with zero surface errors, at $U<0.07$. $U<0.07$. In all cases, γ increases monotonically when the U-threshold is increased. High mirror surface quality is desirable, except at small U-values ($U<0.09$ for 1-stage, and $U<0.12$ for 2-stage concentrator), where γ deteriorates rapidly for $\sigma=0$. For the 1-stage concentrator and $\sigma=0$, $\gamma=89.1\%$ at $U=0.1$, increasing to $\gamma=97.2\%$ at $U=0.5$. With $\sigma=6$ mrad, the corresponding values are $\gamma=74.0\%$ and $\gamma=91.2\%$. For the 2-stage concentrator and $\sigma=0$, $\gamma=71.4\%$ at $U=0.1$ and $\gamma=96.3\%$ at $U=0.5$, and for $\sigma=6$ mrad, $\gamma=66.6\%$ at $U=0.1$ and $\gamma=88.3\%$ at $U=0.5$. The C-distributions at the optimum relative position of the concentrator sides are shown in Figure 4-8 for $U=0.05, 0.15$, and 0.3, and $\sigma=0, 2, 4$, and 6 mrad. Further improvements may be achieved by incorporating an optical mixer. [27]-[29]
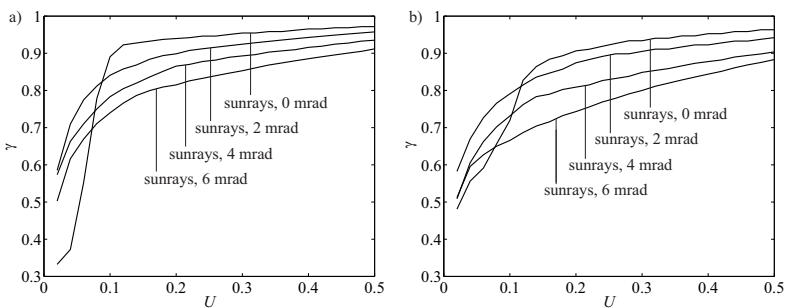

Figure 4-7: Intercept factor γ as a function of the required uniformity U, as defined by Eq. (4.39), a) for 1-stage concentrator, b) for 2-stage concentrator.
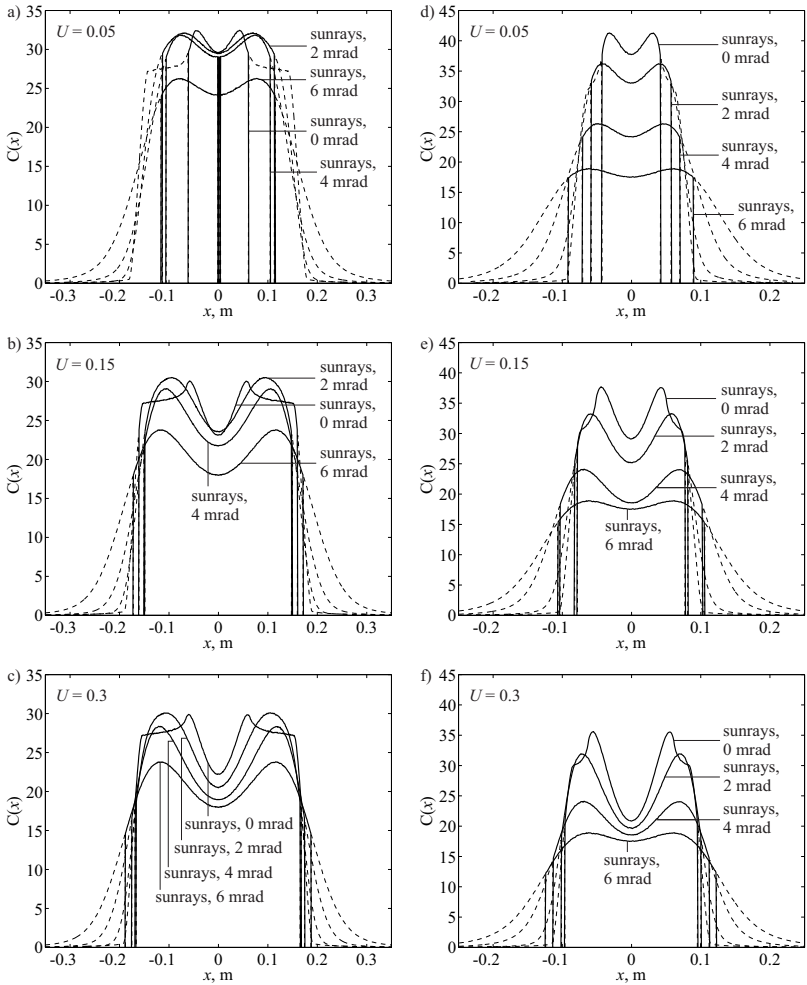
Figure 4-8: C-distributions on the target area after shifting the two reflector wings to their optimum relative position, for the real cases of sunrays (sunshape with $CSR = 5\%$) and for: $U = 0.05$, 0.15, and 0.4; curve parameter is the surface error mode (Bivariate Chi Squared distribution), $\sigma = 0$, 2, 4, and 6 mrad; a)-c): 1-stage concentrator, d)-f) 2-stage concentrator; solid curves: C-distribution intercepted by target area; dashed curves: truncated regions to fulfill the prescribed U.

5 Receiver Heat Transfer Model[1]

In this chapter, a numerical heat transfer model of an air-based cylindrical cavity-receiver is developed and applied to investigate the influence of HTF mass flow rate on outlet HTF temperature, receiver absorption efficiency, HTF pumping power requirements, and thermal losses.

5.1 Receiver Design

The cavity-receiver design is shown schematically in Figure 5-1. It consists of a cylindrical cavity containing an eccentric absorber tube.
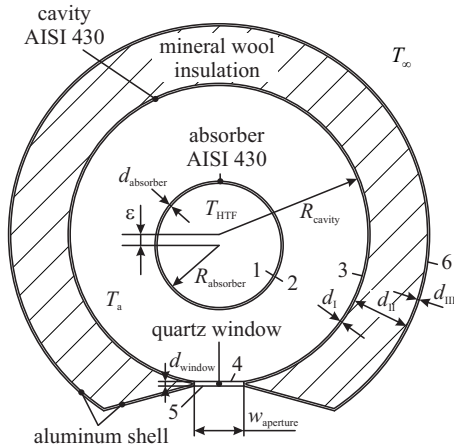

Figure 5-1: Cross-sectional view of the cavity-receiver configuration: 1-absorber inner surface, 2-absorber outer surface, 3-cavity inner surface, 4-window inner surface, 5-window outer surface, 6-shell outer surface.

Cavity and absorber are made of stainless steel, and separated by an annular air gap at ambient pressure. The cavity is lined by a layer of mineral wool insulation, encapsulated in a thin aluminum shell. The rectangular cavity aperture area matches the focal plane of the solar trough concentrator and is closed by a quartz window to reduce reradiation and convection heat losses. The receiver dimensions are listed in Table 5-1.

absorber inner radius $R_{absorber}$	0.125
cavity inner radius R_{cavity}	0.3
absorber wall thickness $d_{absorber}$	$1.5 \cdot 10^{-3}$
cavity inner wall thickness d_{I}	$1.5 \cdot 10^{-3}$
insulation thickness d_{II}	0.1
shell thickness d_{III}	$1 \cdot 10^{-3}$
cavity aperture width $w_{aperture}$	0.1
window thickness d_{window}	$5.43 \cdot 10^{-3}$
eccentricity ε	0.03

Table 5-1: Cavity-receiver dimensions shown in Figure 5-1, in [m].

5.2 Heat Transfer Model

Steady-state energy conservation is given by:

$$\gamma Q_{solar} - Q_{loss,reflection} - Q_{loss,reradiation} - Q_{loss,convection} - Q_{HTF} = 0 \qquad (5.1)$$

where Q_{solar} is the concentrated solar radiation incident on the receiver, γ is the intercept factor defined as the ratio of solar radiation intercepted by the receiver aperture to that incident on the receiver, $Q_{loss,reflection}$ is the solar radiation lost to the environment after one or multiple reflections at surfaces 2-5, $Q_{loss,reradiation}$ is the energy loss by radiation emitted by surfaces 2, 3, 5 and 6, $Q_{loss,convection}$ is the convective heat loss from surfaces 5 and 6, and Q_{HTF} is the energy gain, carried away by the heat transfer fluid.

5.2.1 Conductive heat transfer

2D steady-state energy conservation applied to the solid domains (absorber, cavity, and window) of the receiver reduces to:

$$\underline{\nabla} \cdot \left(k \underline{\nabla} T \right) = 0 \tag{5.2}$$

The boundary condition at the surfaces of the solid domains requires:

$$k \underline{\nabla} T \big|_{\text{surface}} \cdot \hat{n} = -q_{\text{surface}} \tag{5.3}$$

where $\hat{n}$ denotes the surface normal vector, and q_{surface} is the net surface energy flux by combined convection and radiation:

$$q_{\text{surface}} = q_{\text{convection}} + q_{\text{radiation}} \tag{5.4}$$

Table 5-2 lists the number of nodes for the discretization of the cavity (including insulation and shell), absorber, and window. Absorber and window temperatures are assumed constant along dimensions d_{absorber} and d_{window}, hence $n_{\text{absorber}} = n_{\text{window}} = 1$.

m_{absorber}	30
n_{absorber}	1
m_{cavity}	30
n_{cavity}	50
m_{window}	20
n_{window}	1

Table 5-2: Number of nodes for the discretization; absorber and cavity: m and n in angular and radial directions; window: m along w_{aperture} and n along d_{window}.

Discretization of Eq. (5.2) for the temperature at node (i, j) yields: [30]

$$T_{i,j} = \frac{1}{c_{\text{total}}} \left(c_{i \pm 1, j} T_{i \pm 1, j} + c_{i, j \pm 1} T_{i, j \pm 1} - q_{\text{surface}, i, j} dA_{i,j} \right) \tag{5.5}$$

where:

$$c_{\text{total}} = c_{i-1, j} + c_{i+1, j} + c_{i, j-1} + c_{i, j+1} \tag{5.6}$$

and $dA_{i,j}$ is the surface area of boundary control volume (CV) (i, j). For cavity, absorber and window, the coefficients c are given in Table 5-3.

Thermal conductivities at the CV interfaces between node (i, j) and its neighbours in $+$ and $-$ -directions are denoted by $k_{i\pm,j}$ and $k_{i,j\pm}$:

$$k_{i\pm,j} = \frac{2k_{i,j}k_{i\pm1,j}}{k_{i,j} + k_{i\pm1,j}} \tag{5.7}$$

$$k_{i,j\pm} = \frac{2k_{i,j}k_{i,j\pm1}}{k_{i,j} + k_{i,j\pm1}} \tag{5.8}$$

	cavity	absorber	window
$c_{i\pm1,j}$	$\dfrac{\Delta r k_{i\pm,j}}{r_j \Delta\theta}$	$0 \ (n_{\text{absorber}} = 1)$	$k_{i\pm,j}\dfrac{d_{\text{window}}}{\Delta w_{\text{window}}}$
$c_{i,j\pm1}$	$\dfrac{\left(r_j \pm \dfrac{\Delta r}{2}\right)\Delta\theta \cdot k_{i,j\pm}}{\Delta r}$	$\dfrac{\left(r_j \pm \dfrac{\Delta r}{2}\right)\Delta\theta \cdot k_{i,j\pm}}{\Delta r}$	$0 \ (n_{\text{window}} = 1)$

Table 5-3: Coefficients c in the discretized energy conservation equation (5.5) for cavity, absorber, and window; r_j is the radial position of node (i, j), $\Delta\theta$ and Δr are angular and radial cavity/absorber CV dimensions, Δw_{window} and d_{window} are the window CV dimensions, and $k_{i\pm,j}$ and $k_{i,j\pm}$ are thermal conductivities between node (i, j) and its neighbours in $+$ and $-$ -directions.

Temperature dependent thermal conductivities are used for AISI430 stainless steel [31], for mineral wool insulation material and fused silica [32], and for commercial aluminum alloy Al-6061-T6 [33].

5.2.2 Convective heat transfer

The convective heat transfer coefficient between fluid and wall for turbulent flow through a circular pipe is calculated using the *Nu*-correlation: [34]

$$Nu_D = \frac{\left(f_{\text{Moody}}/8\right)\left(Re_D - 1000\right)Pr}{1 + 12.7\left(f_{\text{Moody}}/8\right)^{1/2}\left(Pr^{2/3} - 1\right)} \tag{5.9}$$

valid for $0.5 < Pr < 2000$ and $3000 < Re_D < 5 \cdot 10^6$. Friction factor f_{Moody} is supplied by the Moody diagram, with surface roughness $e = 1.5 \mu m$ (drawn tubing). Natural convective heat transfer coefficient between two nested cylinders is calculated using the Nu-correlation [35] for surface 2, and for surfaces 3 and 4, respectively:

$$Nu_{D_2} = \frac{h_2 D_2}{k} = \cfrac{2}{\ln\left[1 + \cfrac{2}{\left[\left(0.5 Ra_{D_2}^{1/4} \right)^{15} + \left(0.12 Ra_{D_2}^{1/3} \right)^{15} \right]^{1/15}} \right]} \qquad (5.10)$$

$$Nu_{D_3} = \frac{h_3 D_3}{k} = -\cfrac{2}{\ln\left[1 - \cfrac{2}{\left[\left(0.5 Ra_{D_3}^{1/4} \right)^{15} + \left(0.12 Ra_{D_3}^{1/3} \right)^{15} \right]^{1/15}} \right]} \qquad (5.11)$$

with $D_2 = 2\left(R_{\text{absorber}} + d_{\text{absorber}} \right)$ and $D_3 = 2R_{\text{cavity}}$. Bulk air temperature in the annulus, T_a, is found by equating the heat transfer at surface 2, and surfaces 3 and 4:

$$\frac{T_a - \overline{T_{3+4}}}{\overline{T_2} - T_a} = \frac{h_2 A_2}{h_3 A_{3+4}} \qquad (5.12)$$

where $\overline{T}$ denotes area-averaged temperatures and A denotes areas. Because T_a is required in the calculation of Nu_{D_2} and Nu_{D_3}, it is determined iteratively. Air properties are evaluated at the film temperatures $\left(\overline{T_2} + T_a \right)/2$ and $\left(\overline{T_{3+4}} + T_a \right)/2$, using the data from [36] (Appendix C). Natural convective heat transfer coefficient for a horizontal isothermal cylinder is calculated using the Nu-correlation: [37]

$$Nu_{D_6} = \left\{ 0.60 + \frac{0.387 Ra_{D_6}^{1/6}}{\left[1 + \left(0.559/Pr \right)^{9/16} \right]^{8/27}} \right\}^2 \quad , \text{ for } Ra_{D_6} \leq 10^{12} \quad (5.13)$$

with air properties evaluated at the film temperature.

5.2.3 Radiative heat transfer

Radiative exchange results from: i) absorbed solar radiation at surfaces 2, 3 and window, and ii) net radiative heat exchange among surfaces 1-6 and the environment. Hence, the boundary heat flux by radiation is:

$$q_{radiation} = q_{reradiation} - q_{solar} \qquad (5.14)$$

Concentrated solar radiation focused onto the receiver is obtained from the arc-spline solar trough concentrator with $n_{arc} = 4$ arcs, described in chapter 3. Monte Carlo (MC) ray-tracing is applied to both the concentrator and the receiver to determine intercept factor γ, reflection losses $Q_{loss,reflection}$, and solar radiation absorbed by surfaces 2, 3, and the window. [15] Incident solar radiation missing the aperture (spillage) is assumed to be lost. Samples of $n_{ray} = 10^5$ rays are used. The energy carried by a single ray bundle is given by:

$$w_{ray} = \frac{DNI \cos\theta_{skew} A_{concentrator}}{n_{ray}} \qquad (5.15)$$

where DNI is the direct normal solar irradiance, θ_{skew} is the solar incidence angle with respect to normal incidence on the concentrator aperture, and $A_{concentrator}$ is the net concentrator aperture area. Solar energy absorbed by a receiver surface segment of area dA is:

$$q_{solar} dA = n_{absorbed} w_{ray} \qquad (5.16)$$

where $n_{absorbed}$ is the number of rays absorbed by the segment. Surfaces 1 to 3, and 6 are assumed gray-diffuse with uniform surface properties and temperature on each segment. The condition for absorption inside the receiver is:

$$\Re_1 \leq E_m \qquad (5.17)$$

where $\Re_1$ is a random number from a uniform set in the interval $(0,1)$, and E_m is the emissivity of the considered surface segment. Conditions for window transmission, reflection, and absorption are, respectively:

$$\Re_2 \leq T'_{r,\lambda} \qquad (5.18)$$

$$T'_{r,\lambda} < \Re_2 \leq T'_{r,\lambda} + R'_{e,\lambda} \qquad (5.19)$$

$$T'_{r,\lambda} + R'_{e,\lambda} < \Re_2 \qquad (5.20)$$

Spectral directional transmittance $T'_{r,\lambda}$, reflectance $R'_{e,\lambda}$ and absorptance $A'_{b,\lambda}$ of the quartz window are calculated based on spectral refractive index n_λ and extinction coefficient κ_λ: [15],[38]

$$T'_{r,\lambda} = \tau'_\lambda \frac{1-\rho'_\lambda}{1+\rho'_\lambda} \frac{1-\rho'^2_\lambda}{1-\rho'^2_\lambda \rho'^2_\lambda} \tag{5.21}$$

$$R'_{e,\lambda} = \rho'_\lambda \left[1 + \frac{\left(1-\rho'_\lambda\right)^2 \tau'^2_\lambda}{1-\rho'^2_\lambda \tau'^2_\lambda} \right] \tag{5.22}$$

$$A'_{b,\lambda} = \frac{\left(1-\rho'_\lambda\right)\left(1-\tau'_\lambda\right)}{1-\rho'_\lambda \tau'_\lambda} \tag{5.23}$$

where:

$$\rho'_\lambda = \frac{1}{2}\left[\frac{\tan^2\left(\theta-\chi\right)}{\tan^2\left(\theta+\chi\right)} + \frac{\sin^2\left(\theta-\chi\right)}{\sin^2\left(\theta+\chi\right)} \right] \tag{5.24}$$

$$\tau'_\lambda = \exp\left(-\alpha_\lambda \cdot s'_\lambda\right) \tag{5.25}$$

with:

$$\alpha_\lambda = \frac{4\pi\kappa_{\lambda,\mathrm{SiO_2}}}{\lambda} \tag{5.26}$$

θ is the ray incidence angle on the window, and s'_λ is the ray's optical path length inside the window, $s'_\lambda = d_\mathrm{w}/\cos\chi$, with angle of refraction χ calculated from Snell's law. Radiative heat exchange among surfaces 1-4 and the environment is calculated with the net radiation method for enclosures (radiosity equation) comprising semi-transparent windows, derived in Appendix A: [15]

$$\sum_{i=1}^{N} \frac{q_{\mathrm{reradiation},i}}{A_{b,i}}\left(\delta_{ki} - F_{k-i}R_{e,i}\right) = \sum_{i=1}^{N}\left(F_{k-i}\left(T_{r,i}-1\right)+\delta_{ki}\right)\frac{E_{m,i}}{A_{b,i}}\sigma T_i^4 \tag{5.27}$$

where:

$$\delta_{ki} = \begin{cases} 1, \text{if } k=i \\ \\ 0 \text{ otherwise} \end{cases} \tag{5.28}$$

and indices k and i denote surface segments on surfaces 1-4 and run from 1 to $N = 2m_\mathrm{absorber} + m_\mathrm{cavity} + m_\mathrm{window}$. F_{k-i} is the configuration factor from segment k to segment i, determined with MC ray-tracing. For opaque surface segments $T_{r,i} = 0$. Hemispherical total window transmittance T_r,

reflectance R_e, absorptance A_b, and emittance E_m used in Eq. (5.27) are calculated from directional spectral quantities by: [15]

$$c = \int_{\varphi=0}^{2\pi} \int_{\theta=0}^{\pi/2} \int_{\lambda=0}^{\infty} \frac{c'_\lambda(\lambda,\theta)e_{\lambda b}(\lambda,T)\cos\theta\sin\theta d\lambda d\theta d\varphi}{\pi\sigma T^4} \tag{5.29}$$

where c represents T_r, R_e, A_b or E_m, and $e_{\lambda b}(\lambda,T)$ is the blackbody spectral emissive power at temperature T. The area-weighted average temperature of surfaces 2, 3 and 4 is used in the calculation of T_r, R_e, and A_b, while the local window segment temperature is used in the calculation of E_m. Radiative heat losses from surfaces 5 and 6 are calculated from:

$$q_{\text{reradiation},5,6} = E_m\,\sigma\left(T^4 - T_{\text{sky}}^4\right) \tag{5.30}$$

where T is the local surface temperature. Radiative heat losses (radiosity) from surfaces 2 and 3 to the environment are calculated from (4):

$$Q'_{\text{loss,reradiation},2+3} = \Delta w_{\text{window}} \sum_{i_{\text{w}}=1}^{m_{\text{window}}} \frac{T_{r,i_{\text{w}}}}{A_{b,i_{\text{w}}}}\left(E_{m,i_{\text{w}}}\sigma T_{i_{\text{w}}}^4 - q_{\text{reradiation},i_{\text{w}}}\right) \tag{5.31}$$

where index i_{w} denotes the window CVs and $q_{\text{reradiation},i_{\text{w}}}$ is obtained from Eq. (5.27).

5.2.4 Pumping power requirement

Pressure drop Δp_{HTF} of the HTF flow between receiver inlet and outlet is calculated by numerical integration of: [32]

$$
\begin{aligned}
\Delta p_{\text{HTF}} &= \int_0^{l_{\text{receiver}}} \frac{\partial p_{\text{HTF}}}{\partial y^*} dy^* \\
&= \frac{1}{4R_{\text{absorber}}} \int_0^{l_{\text{receiver}}} f_{\text{Moody}} \cdot \rho_{\text{HTF}}\left(T_{\text{HTF}}(y^*)\right) U_{\text{HTF}}^2\left(T_{\text{HTF}}(y^*)\right) dy^*
\end{aligned}
\tag{5.32}
$$

Power requirement W_{p} for compression of the HTF from atmospheric pressure p_∞ to receiver inlet pressure $p_{\text{HTF,in}} = p_\infty + \Delta p_{\text{HTF}}$ with isentropic pump efficiency $\eta_{\text{p,s}}$ is calculated assuming ideal gas:

$$W_{\text{p}} = \frac{m_{\text{HTF}}}{\eta_{\text{p,s}}} \frac{R_{\text{HTF}} T_{\text{HTF,in}}}{\kappa_{\text{HTF}} - 1}\left[1 - \left(\frac{p_{\text{HTF,in}}}{p_\infty}\right)^{\frac{1-\kappa_{\text{HTF}}}{\kappa_{\text{HTF}}}}\right] \tag{5.33}$$

where $T_{\text{HTF,in}}$ is the HTF temperature at receiver inlet.

5.2.5 Absorption efficiency

Energy balance for an absorber section of length dy yields: [39]

$$m_{\text{HTF}} c_{p,\text{HTF}} dT_{\text{HTF}} = Q'_{\text{HTF}} dy \tag{5.34}$$

Since $Pe \gg 1$ the HTF temperature $T_{\text{HTF}}(y)$ at distance y from the receiver inlet is calculated by numerically integrating:

$$T_{\text{HTF}}(y) = T_{\text{HTF,in}} + \int_0^y \frac{Q'_{\text{HTF}}(y^*)}{m_{\text{HTF}} \cdot c_{p,\text{HTF}} \left(T_{\text{HTF}}(y^*) \right)} \tag{5.35}$$

The overall receiver absorption efficiency is defined as:

$$\eta_{\text{absorption}} = \frac{Q_{\text{HTF}}}{Q_{\text{solar}}} \tag{5.36}$$

The local receiver absorption efficiency is defined as:

$$\eta_{\text{absorption,local}} = \frac{Q'_{\text{HTF}}}{Q'_{\text{solar}}} \tag{5.37}$$

where Q'_{solar} in $\left[\text{W/m} \right]$ is the solar radiation reflected by the primary concentrator that is incident locally on the receiver, per unit receiver length.

5.3 Simulation Results

The baseline parameters are given in Table 5-4. Solar radiation incident on the receiver is $Q_{\text{solar}} = 289 \, \text{kW}$. The ideal radiative flux at the receiver aperture, shown in Figure 3-6, is reduced by 13.4% due to solar incidence angle $\theta_{\text{skew}} = 30°$, by 8.5% due to transmission losses introduced by the concentrator top membrane, and by an additional 6.3% due to reflection losses on the mirrors. Peak concentration is reduced to 135. End effects due to skew radiation and other concentrator imperfections are omitted from consideration. HTF mass flow rate is varied in the range $0.1 - 1.2$ kg/s. The integration step along the receiver axis is 1 m. Energy balance Eq. (5.1) is used as the convergence criterion in each 2D simulation step, with maximum residuum $< 1\%$.
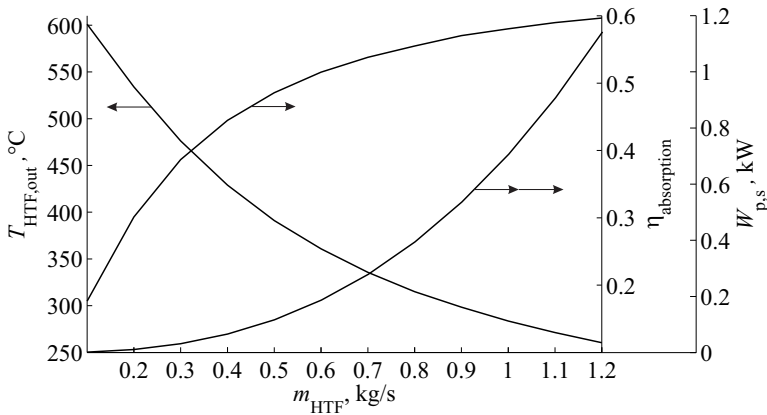
The outlet HTF temperature $T_{\text{HTF,out}}$, receiver absorption efficiency $\eta_{\text{absorption}}$, and mechanical pumping power requirement $W_{\text{p,s}}$ are shown as a function of the HTF mass flow rate m_{HTF} in Figure 5-2.

direct normal insolation DNI, $\left[\text{W}/\text{m}^2 \right]$	850
solar incidence angle θ_{skew}, $[\text{deg}]$	30
HTF inlet temperature $T_{\text{HTF,in}}$, $[\degree\text{C}]$	120
HTF inlet pressure $p_{\text{HTF,in}}$, $[\text{bar}]$	1.0
ambient air temperature T_∞, $[\degree\text{C}]$ *	60
apparent sky temperature T_{sky}, $[\degree\text{C}]$	1.85
emissivity surface 1 ε_1	0.8
emissivity surface 2 ε_2	0.9
emissivity surface 3 ε_3	0.1
emissivity surface 6 ε_6	0.1
concentrator length $l_{\text{concentrator}}$, $[\text{m}]$	50
net concentrator aperture area $A_{\text{concentrator}}$, $\left[\text{m}^2 \right]$	475

Table 5-4: Baseline parameters; * the temperature in the air tube of the concentrator that contains the receiver (Figure 3-1) is at elevated temperature.

Figure 5-2: HTF outlet temperature $T_{\text{HTF,out}}$, receiver absorption efficiency $\eta_{\text{absorption}}$, and mechanical pumping power requirement $W_{\text{p,s}}$, for HTF mass flow rates in the range $0.1 – 1.2$ kg/s.

As m_{HTF} increases from 0.1 to 1.2 kg/s, $T_{HTF,out}$ decreases from 601 to 260 °C, $\eta_{absorption}$ increases from 17.6 to 59.7%, and $W_{p,s}$ increases from 1.9 W to 1.14 kW ($W_{p,s} \propto U_{HTF}^3$). Figure 5-3 shows the thermal losses from the receiver, normalized by $Q_{solar} = 289$ kW. The white portions of the bars represent the absorption efficiency $\eta_{absorption}$. Temperature independent losses are: 8.7 % incoming radiation spilled at the aperture, 12.7 % reflection losses at the window, and 3.4 % reflection losses from surfaces 2 and 3 to the environment. As m_{HTF} is reduced from 1.2 to 0.1 kg/s, temperature dependent losses change in the following ranges: reradiation losses from surfaces 2 and 3 to the environment: 0.83 - 14.7 %, reradiation from surface 6 to the environment: 2.8 - 6.4 %, reradiation from the window to the environment: 5.5 - 15.7 %, convection losses from surface 6: 4.9 - 16.4 %, convection losses from surface 5: 1.8 - 4.2 %. Overall, the temperature dependent losses increase from 15.8 % at $m_{HTF} = 1.2$ kg/s to 57.4 % at $m_{HTF} = 0.1$ kg/s. Local thermal losses and HTF temperature vary along the receiver axis x. For $m_{HTF} = 0.4$ kg/s, local losses increase from 2524 W/m at the entrance, where $T_{HTF,in} = 120$ °C, to 3900 W/m at the receiver outlet, where $T_{HTF,out} = 429$ °C (Figure 5-4).
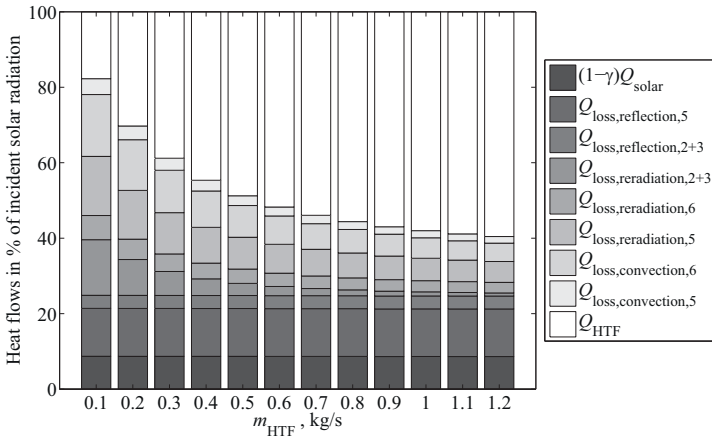

Figure 5-3: Heat flows by modes in %, normalized by the total concentrated incident solar power Q_{solar}; the diagram reports the useful energy gain and specifies the different contributions to energy losses for HTF mass flow rates in the range 0.1-1.2 kg/s.
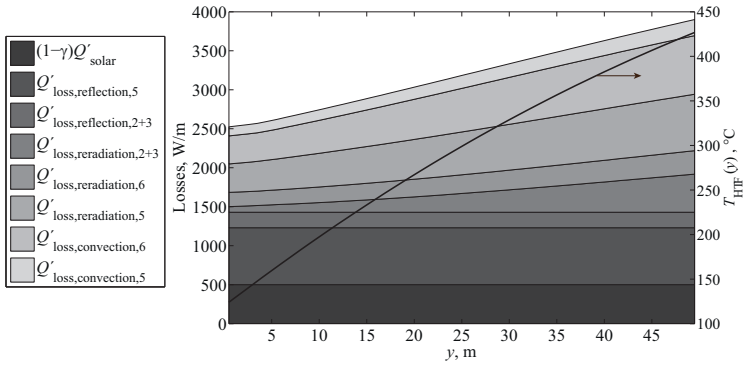
Figure 5-4: Thermal losses and HTF temperature (black curve) as a function of position along the receiver axis x, $m_{HTF} = 0.4$ kg/s.

Integrated over the receiver length, the largest heat loss sources are reflection at the window (12.7 % of Q_{solar}), convection at the receiver outer surface (9.6 % of Q_{solar}), radiation emitted by the window (9.5 % of Q_{solar}), and interception losses (8.7 % of Q_{solar}).

The local absorption efficiency $\left(\eta_{absorption,local} = Q'_{HTF}/Q'_{solar}\right)$ as a function of local HTF temperature is shown in Figure 5-5 for HTF mass flow rates in the range 0.2 – 1.2 kg/s, and compared to that of a commercial Schott PTR70 receiver. [40] The absorption efficiency of the receiver at a given HTF temperature decreases with decreasing mass flow rate due to decreasing convective heat transfer between absorber tube and HTF. $\eta_{absorption}$ is lower than that of the Schott receiver by at least 14.6 %-points at the entrance with 1.2 kg/s HTF mass flow, and by at most 48.6 %-points at the outlet with 0.2 kg/s HTF mass flow. If the concentrator module length is increased, higher HTF mass flow rate will be required in order to maintain constant HTF outlet temperature, leading to higher pumping power requirement W_p. Figure 5-6 shows W_p normalized by the estimated electricity output $W_{electric}$ associated with one module, as a function of the module length, for different absorber tube radii $R_{absorber}$. Parameters used in the calculations are listed in Table 5-5.
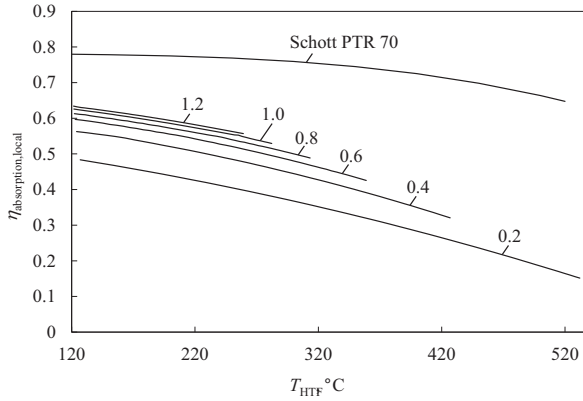
78

Figure 5-5: Local absorption efficiency as a function of the local HTF temperature; parameter is the HTF mass flow rate in kg/s; for comparison, the absorption efficiency of a commercial Schott PTR70 receiver is shown. [40]
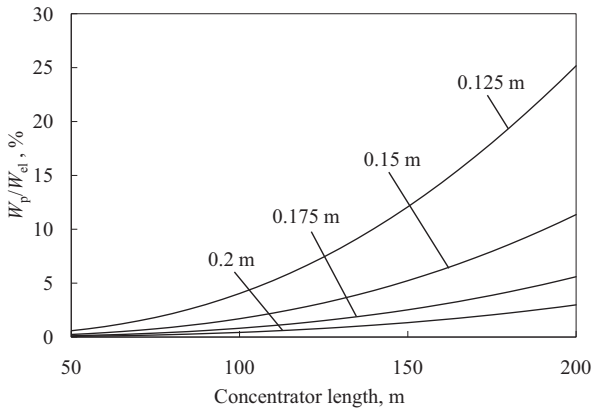

Figure 5-6: Electric pumping power requirement in % of estimated electric power output for one module of given length; parameter is the absorber tube radius.

HTF inlet temperature $T_{HTF,in}$, $[°C]$	120
HTF outlet temperature $T_{HTF,out}$, $[°C]$	400
receiver absorption efficiency $\eta_{absorption}$	0.7
isentropic pump efficiency η_p	0.9
electric generator efficiency $\eta_{generator}$	0.9
power cycle efficiency $\eta_{Rankine}$	0.3
solar power incident on receiver Q'_{solar}, $[W/m]$	5780

Table 5-5: Parameters in pumping power calculations; local receiver absorption efficiency and incident solar power are assumed constant along the receiver.

$\eta_{absorption}$ is set to 0.7, and m_{HTF} is calculated such that $T_{HTF,out}$ = 400°C throughout all cases. With the current absorber radius $R_{absorber}$ = 0.125 m, the HTF compressor would consume 25% of the produced electricity for a 200 m long module. Increasing $R_{absorber}$ to 0.2 m reduces the pumping power requirement to tolerable 3%.

5.4 Summary and Conclusions

We examined a new design of an air-based receiver for solar trough concentrators that features a tubular absorber contained in an insulated cavity, with a rectangular aperture closed by a quartz window. Numerical heat transfer simulations were conducted for a 50 m-long and 9.5 m-wide collector section, with fixed heat transfer fluid (HTF) inlet temperature 120°C. As the HTF mass flow rate was varied in the range 0.1 – 1.2 kg/s, HTF outlet temperatures decreased from 601 to 260 °C, absorption efficiencies increased from 18 to 60 %, and isentropic pumping power requirements increased from 1.9 W to 1.14 kW. Main energy losses were caused by incoming solar radiation being spilled and reflected at the receiver aperture. With decreasing mass flow rates and, consequently, increasing receiver temperatures, convection losses at the cavity outer surface and reradiation losses became predominant. Higher receiver's absorption efficiency is achievable by optimizing the receiver geometry, improving the cavity insulation, applying an antireflective coating on the

aperture window, and by incorporating a secondary concentrator at the cavity aperture. If longer modules are used, the absorber tube radius will have to be increased in order to keep the pumping power requirements to a tolerable level.

6 Prototype Receiver[1]

A 42m-long full-scale prototype receiver section has been built and tested on the solar trough concentrator described in chapter 3, located is Biasca, Switzerland . This chapter reports on the receiver testing and the heat transfer model validation.

6.1 Prototype Receiver Layout

A cross-section of the prototype receiver layout is shown in Figure 6-1a,
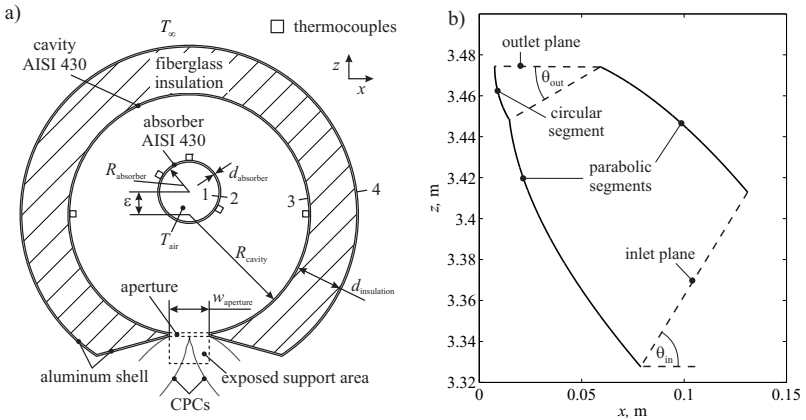

Figure 6-1: a) Receiver prototype cross-section: major changes compared to the design in Figure 5-1 are the omission of the aperture window and the inclusion of secondary concentrators at the aperture; squares indicate thermocouple locations installed at the center between receiver inlet and outlet; b) enlarged view of the right CPC secondary concentrator.

with dimensions given in Table 6-1. The receiver consists of a black-painted absorber tube, contained in an insulated cylindrical cavity to reduce radiative and convective energy losses. The design procedure of the asymmetric CPCs (Figure 6-1b) is described in [41]. CPC design parameters and key figures are given in Table 6-2. The focal line of the primary concentrator lies on the CPC inlet plane.

absorber inner radius $R_{absorber}$, $[mm]$	69.6
radius change at tube connections $\Delta R_{absorber}$, $[mm]$	10.6
absorber wall thickness $d_{absorber}$, $[mm]$	1.4
cavity inner radius R_{cavity} , $[mm]$	300
insulation thickness $d_{insulation}$, $[mm]$	92.5
cavity aperture width $w_{aperture}$, $[mm]$	109.5
absorber tube eccentricity ε	64
roughness surface 1, $[mm]$	2
emissivity surface 1	0.7
emissivity surface 2	0.85
emissivity surface 3	0.1
specular reflectivity surface 3	0.45
emissivity surface 4	0.1
receiver (axial) length, $[m]$	41.8
number of axial absorber sections	13

Table 6-1: Prototype receiver parameters.

tolerance for directional errors of incident rays δ, [mrad]	9.18
inlet angle θ_{in}, [deg]	58.7
outlet angle θ_{out}, [deg]	30.1
geometrical concentration ratio, 1st stage	44.6
geometrical concentration ratio, 2nd stage	1.94
geometrical concentration ratio of the 2-stage concentrator	86.3
specular reflectivity [42]	0.93
fraction of accepted rays (for CPC reflectivity = 1)	1.0
average number of ray reflections	0.895
CPC transmittance	0.936

Table 6-2: Design parameters and performance figures characterizing the secondary concentrator; performance figures are determined with MC ray-tracing through primary and secondary concentrator, neglecting tracking and concentrator shape errors.

A circular segment is attached to the CPC outlet to connect the CPC to the receiver aperture. The CPC accepts all sunrays that are incident from the primary concentrator (Table 6-3) with accumulated directional error (due to sunshape, tracking error, and primary concentrator shape errors) smaller than δ. Figure 6-2 shows solar flux concentration distribution (a), and angular flux distribution (b) at the right secondary concentrator outlet, determined by applying MC ray-tracing to primary and secondary concentrators.

length, [m]	43.5
total/net aperture width, [m]	10.1 / 8.9
$x-/z-$ coordinates of focal line, [m]	(0.105, 3.371)
inner rim angle, [deg]	8.27
outer rim angle, [deg]	72.4

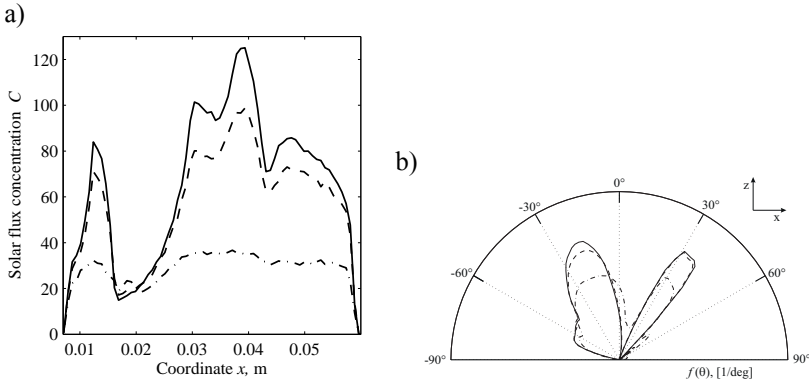Table 6-3: Primary concentrator dimensions.

a)

b)

Figure 6-2: a) Solar flux concentration distribution (a), angular flux distribution (b) at the right secondary concentrator's outlet, for solar incidence angles $\theta_{\text{skew}} = 0°$ (solid lines), $\theta_{\text{skew}} = 30°$ (dashed lines), and $\theta_{\text{skew}} = 60°$ (dash-dotted lines).

6.2   Heat Transfer Modeling

The receiver heat transfer modeling is described in chapter 5. This section addresses only those parts of the heat transfer model that have been adapted or added in order to model the prototype receiver.

6.2.1   Energy balance

Overall receiver energy balance is:

$$
\begin{aligned}
\frac{dU_{\text{receiver}}}{dt} = Q_{\text{solar}} - Q_{\text{loss,spillage}} - Q_{\text{loss,reflection}} - Q_{\text{loss,reradiation}} \cdots \\
- Q_{\text{loss,convection}} - Q_{\text{loss,conduction}} - Q_{\text{HTF}}
\end{aligned}
\tag{6.1}
$$

where U_{receiver} is the inner energy content of the receiver, Q_{solar} is the solar radiation reflected by the primary concentrator, $Q_{\text{loss,spillage}}$ is the solar radiation spilled at the receiver aperture (spillage at CPC inlets, absorption by the CPCs, spillage between CPCs and receiver aperture), $Q_{\text{loss,reflection}}$ is the solar radiation lost to the environment after one or multiple reflections at surfaces 2 and 3 inside the receiver (Figure 6-1a), $Q_{\text{loss,reradiation}}$ and $Q_{\text{loss,convection}}$ are energy losses from surfaces 2 to 4 by emitted radiation and convection, $Q_{\text{loss,conduction}}$ is the energy lost through the receiver end plates

and receiver supports by conduction, and Q_{HTF} is the energy removed from the receiver by the HTF. 2D heat conduction $\rho c\left(\partial T/\partial t\right) = \underline{\nabla}\cdot\left(k\underline{\nabla}T\right)$ inside the solid domains is calculated by finite-volume techniques, applying the fully implicit scheme. [30] The energy flux at the surfaces of the solid domains consists of convection and radiation, $q_{\text{surface}} = q_{\text{convection}} + q_{\text{radiation}}$.

6.2.2 Convective heat transfer

2D transient CFD simulations are conducted to determine the steady-state natural convective heat transfer at surfaces 2 and 3, for uniform surface temperatures T_2 and T_3. [43] Steady-state is reached within 500s in all cases. Since:

$$Ra = \left(g\beta\left(R_{\text{cavity}} - R_{\text{absorber}}\right)^3\left(T_2 - T_3\right)\right)\Big/\left(\nu\alpha\right) \le 8\cdot 10^7 \qquad (6.2)$$

for all cases, turbulence is expected only locally, and simulations are run laminar. [35] Details of the CFD simulation model are listed in Table 6-4.

mesh	tetrahedral with prism boundary layers at surfaces 2 and 3 baseline mesh: 578'436 elements / 124'357 nodes fine mesh: 3'243'093 elements / 642'926 nodes coarse mesh: 126'462 elements / 29'606 nodes
domain size	1.4x0.1x1.2m^3 (enlarged: 1.8x0.5x1.6m^3)
flow regime	laminar, transient
fluid model	air, real gas, reference pressure: 1atm
boundary conditions	$x-z$-planes: free slip, adiabatic all other boundary planes: opening with entrainment, static temperature: 318.15K receiver surfaces: no-slip, adiabatic
initialization	initial temperature in fluid domain: 318.15K
convergence criteria	max-residual for mass, momentum, and energy equations below 1E-3 in each time step

Table 6-4: Details of the CFD-simulations to determine the convective heat transfer at surfaces 2 and 3.

The influence of mesh cell size and calculation domain size on the simulation results $Q_{\text{convection.2}}$ and $Q_{\text{convection.3}}$ have been analyzed. The results of this analysis are plotted in Figure 6-3, with cell sizes and domain sizes given in Table 6-5. The relative mesh cell size is calculated from:

$$\frac{l_{\text{cell}}^{\text{coarse}}}{l_{\text{cell}}^{\text{baseline}}} = \sqrt[3]{\frac{n_{\text{cell}}^{\text{baseline}}}{n_{\text{cell}}^{\text{coarse}}}} \quad \text{and} \quad \frac{l_{\text{cell}}^{\text{fine}}}{l_{\text{cell}}^{\text{baseline}}} = \sqrt[3]{\frac{n_{\text{cell}}^{\text{baseline}}}{n_{\text{cell}}^{\text{fine}}}} \tag{6.3}$$

where n_{cell} is the number of cells the calculation domain consists of.

run	rel. cell size	domain size
1	0.56 (fine)	1.4x0.1x1.2m^3
2	1 (baseline)	1.4x0.1x1.2m^3
3	1.66 (coarse)	1.4x0.1x1.2m^3
4	1	1.8x0.5x1.6m^3

Table 6-5: Parameter settings to study the influence of mesh cell size and calculation domain size on the simulation results for $Q_{\text{convection.2}}$ and $Q_{\text{convection.3}}$; $T_2 = 664\text{K}$, $T_3 = 406\text{K}$, and $\beta_{\text{inclination}} = 30°$ in all runs.
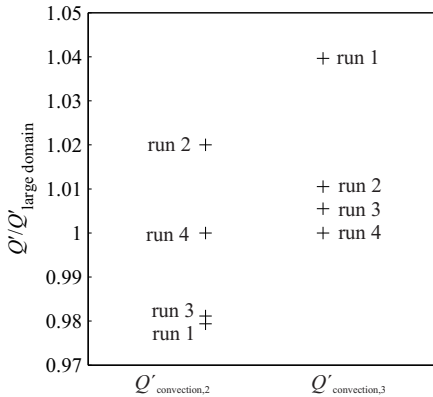

Figure 6-3: Influence of mesh cell size and calculation domain size on the normalized simulation results $Q_{\text{convection.2}} / Q_{\text{convection,2}}^{\text{large domain}}$ and $Q_{\text{convection,3}} / Q_{\text{convection,3}}^{\text{large domain}}$; $Q_{\text{convection,2}}^{\text{large domain}}$ and $Q_{\text{convection,3}}^{\text{large domain}}$ are the results of run 4; parameter settings as given in Table 6-5.

A parametric study is performed to determine the coefficients of second-order models that correlate average convective heat transfer rates at surfaces 2 and 3, $Q'_{\text{convection,2}}$, $Q'_{\text{convection,3}}$, to T_2 and T_3, with the receiver aperture in horizontal (downward facing) position, and $T_\infty = 45°C$. A D-optimal design is established with 9 data points, imposing $T_2 \geq T_3$. [44] In Figure 6-4 the CFD simulation results (+) and the resulting empirical correlations for $Q'_{\text{convection,2}}(T_2, T_3)$ and $Q'_{\text{convection,3}}(T_2, T_3)$ (solid curves) are plotted. The correlation fits the data points well. For comparison, the results obtained with Nu-correlation [35] for convective heat transfer between nested cylinders is shown as dashed curves. For the considered temperature ranges $323K \leq T_2 \leq 723K$, and $323K \leq T_3 \leq 653K$, the heat loss through the aperture $Q'_{\text{aperture}} = Q'_{\text{convection,2}} + Q'_{\text{convection,3}}$ is <33 W/m, hence correlation [35] describes the CFD simulation results well. Analogously, empirical models for $Q'_{\text{convection,2}}$ and $Q'_{\text{convection,3}}$ have been established, based on 17 data points, for a tilted receiver aperture with tilt angle $\beta_{\text{inclination}} = 0 \div 60°$.
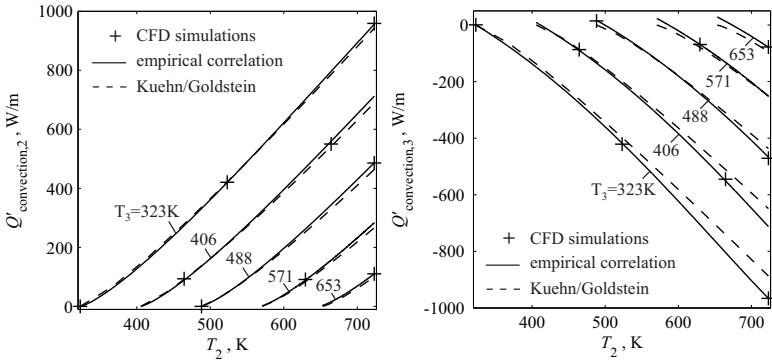

Figure 6-4: Convective heat transfer at surfaces 2 and 3, $Q'_{\text{convection,2}}$, $Q'_{\text{convection,3}}$, as functions of uniform surface temperatures T_2 and T_3, with horizontal downward facing receiver aperture ($\beta_{\text{inclination}} = 0°$); shown are the CFD simulation results (+), the empirical correlation fitted to the simulation data points (solid curves), and the results obtained with correlation [35] for convective heat transfer between nested cylinders (dashed curves); the CFD-data points correspond to the solid curve on which they lie.

6.2.3 Radiative heat transfer

The distribution of absorbed solar radiation on surfaces 2 and 3 is determined by applying MC ray-tracing to primary concentrator and receiver. The primary concentrator part of the MC model has been described and validated in chapter 3. Surface 2 is modeled gray-diffuse, surface 3 is modeled partially specular. Radiative heat exchange among surfaces 2, 3, and the cavity aperture is modeled with the radiosity equation for enclosures that involve partially specular gray surfaces: [45]

$$\sum_{i=1}^{N}\left[\delta_{ki}-\left(1-\rho_i^s\right)F_{k-i}^s\right]\sigma T_i^4 = \sum_{i=1}^{N}\left(\frac{\delta_{ki}}{\varepsilon_i}-\frac{\rho_i^d}{\varepsilon_i}F_{k-i}^s\right)q_{\text{radiation},i} \qquad (6.4)$$

where N is the total number of surface segments involved, and the reflectivity ρ is split into specular and diffuse parts, $\rho = \rho^s + \rho^d$. The specular view factors F_{k-i}^s are determined with MC ray-tracing. At surface 4:

$$q_{\text{radiation},4} = \varepsilon_4\left(\sigma\left(T_4^4 - T_{\text{sky}}^4\right) - q_{\text{solar},4}\right) \qquad (6.5)$$

where T_{sky} is the effective sky temperature, and $q_{\text{solar},4}$ is the solar flux incident on surface 4. [46]

6.2.4 Minor heat losses

Conductive heat losses through the 14 receiver supports is calculated from: [47]

$$Q_{\text{support}} = \bar{h}A_{\text{support}}\left(T_{\text{support}} - T_{\infty}\right) \qquad (6.6)$$

assuming the temperature of each support, T_{support}, to be uniform and equal to T_3 next to the aperture. A_{support} is the support's surface area exposed to the surrounding air (Figure 6-1a).

Heat losses through the insulated receiver end plates is calculated from 1D energy balances, assuming the end plate inner surface temperatures to be equal to the average temperature of their surroundings.

6.2.5 Heat transfer fluid flow

The HTF flow through the absorber pipe is assumed to be fully developed turbulent throughout the measurement section. The flow profile is described by: [48]

$$\frac{u_{\mathrm{HTF}}(r)}{u^*} = 2.5\ln\left[\frac{3(1+r/R_{\mathrm{absorber}})}{2\left[1+2(r/R_{\mathrm{absorber}})^2\right]}\frac{(R_{\mathrm{absorber}}-r)u^*}{v}\right]+5.5 \quad (6.7)$$

where r is the radial coordinate from the pipe center. The HTF mass flow rate is calculated by numerical integration of Eq. (6.7), after determination of u^* using the measured $u_{\mathrm{HTF}}(r=0)$.

The pressure drop in the air flow is caused by wall friction and local losses at the interconnections of the absorber tube sections:

$$\Delta p_{\mathrm{HTF}} = \int_0^{l_{\mathrm{receiver}}} \frac{f_{\mathrm{Moody}}\rho_{\mathrm{HTF}}U_{\mathrm{HTF}}^2}{4R_{\mathrm{absorber}}}dy^* + \sum_{i=1}^{n_{\mathrm{connection}}} \Delta p_{\mathrm{HTF,connection},i} \quad (6.8)$$

with pressure drop at each interconnection i calculated from:

$$\Delta p_{\mathrm{HTF,connection},i} = 0.5\cdot K_{\mathrm{connection}}\cdot\rho_{\mathrm{HTF}}(y_i)\cdot U_{\mathrm{HTF}}^2(y_i) \quad (6.9)$$

where the loss coefficient $K_{\mathrm{connection}}$ is calculated assuming a sudden pipe contraction by $\Delta R_{\mathrm{absorber}}$ (Table 6-1) at the interconnection. [49] The isentropic pumping power requirement associated with the HTF flow through the receiver is calculated from (ideal gas):

$$W_{\mathrm{pump,s}} = \frac{m_{\mathrm{HTF}}R_{\mathrm{HTF}}T_{\mathrm{HTF,in}}}{\kappa_{\mathrm{HTF}}-1}\left[1-\left(\frac{p_{\mathrm{HTF,in}}}{p_{\mathrm{HTF,in}}-\Delta p_{\mathrm{HTF}}}\right)^{\frac{1-\kappa_{\mathrm{HTF}}}{\kappa_{\mathrm{HTF}}}}\right] \quad (6.10)$$

6.2.6 Numerical solution

The solid domains (absorber and cavity) are discretized along the cylindrical coordinates with uniform grids. Their temperature distributions are determined iteratively with the Jacobi method. Convergence of the temperature distributions is assumed to be reached after iteration step k if:

$$\left|\frac{T_{i,j}^k - T_{i,j}^{k-1}}{T_{i,j}^k}\right| < 10^{-3} \quad (6.11)$$

is fulfilled by each node (i, j), and

$$\frac{1}{m \cdot n} \sum_{i=1}^{m} \sum_{j=1}^{n} \left| \frac{T_{i,j}^{k} - T_{i,j}^{k-1}}{T_{i,j}^{k}} \right| < 10^{-5} \tag{6.12}$$

is fulfilled by the sum of all nodes. The energy balance has converged if:

$$\left| Q'_{\text{solar}} - Q'_{\text{loss,spillage}} - Q'_{\text{loss,reflection}} - Q'_{\text{loss,reradiation}} - Q'_{\text{loss,convection}} \cdots \right.$$
$$\left. - Q'_{\text{loss,conduction}} - Q'_{\text{HTF}} - \frac{dU_{\text{receiver}}}{dt} \right| < 1\,\text{W/m} \tag{6.13}$$

The results of a grid convergence study, using the HTF temperature at the receiver outlet, $T_{\text{HTF,out}}$, as the reference quantity, are shown in Figure 6-5. Normalized grid spacing of 2 corresponds to the final grid parameters, which are listed in Table 6-6 together with the grid convergence indexes. The number of rays emitted from each receiver surface segment to determine the specular view factors F_{i-j}^{s} is set to 10^{5}, based on a sensitivity analysis.
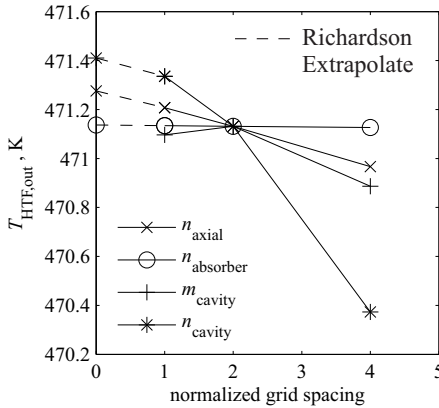

Figure 6-5: a) Influence of grid spacing on HTF outlet temperature $T_{\text{HTF,out}}$; numbers of nodes: n_{axial}: axial direction (both absorber and cavity); n_{absorber}: absorber tube circumference; m_{cavity}: cavity thickness; n_{cavity}: cavity circumference.

grid parameter	no. of nodes	grid convergence index [%]
receiver, axial n_{axial}	418	9.24E-2
absorber, radial $m_{absorber}$	1	-
absorber, circumferencial $n_{absorber}$	50	3.65E-3
cavity, radial m_{cavity}	50	-
cavity, circumferencial n_{cavity}	100	1.78E-1

Table 6-6: Number of nodes in the discretization of the receiver's solid domains; grid convergence indexes are calculated for the reference quantity $T_{HTF,out}$ with safety factor of 3. [50]

6.3 Receiver Test Facility

The receiver test facility is shown in Figure 6-6. The HTF is fed to the receiver by a MVF/Seipee blower ($W_{pump,max} = 7.5\,\text{kW}$, $\Delta p_{max} = 62\text{mbar}$, $V_{max} = 2700\,\text{m}^3/\text{h}$) via a 50kW electric heater. The design of the primary concentrator is described in chapter 3.
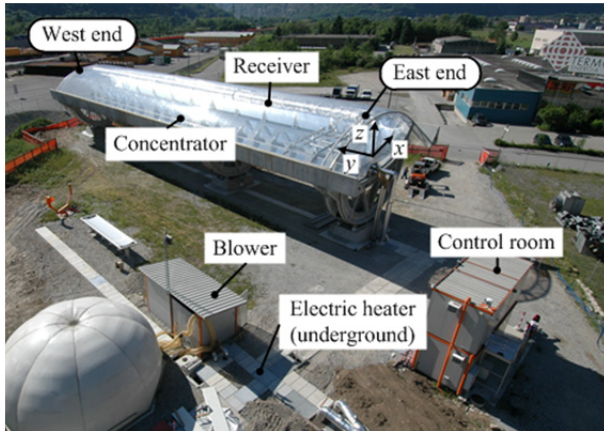

Figure 6-6: Receiver prototype test facility in Biasca/CH (source: Airlight Energy SA).

The concentrator semi-profile consists of an array of 4 adjacent circular arcs that approach the parabolic profile with an rms-slope angle deviation of 0.8 mrad (design value). Concentrator orientation is E-W.

Direct normal solar irradiance (DNI) is measured with a Kipp and Zonen CHP1 pyrheliometer (acceptance angle: 5°, response time: 5s, nonlinearity: $\pm 0.2\%$). HTF velocities at the centerline of the receiver inlet and outlet pipes are measured with a Dwyer 641-6 velocity transmitter (accuracy: 3% FS). HTF temperature at receiver inlet and outlet is measured in-situ with K-type mantle thermocouples (Transmetra). The measurement error due to radiative heat transfer between mantle and absorber tube (up to 3.3% in the receiver heat loss results presented in the following section) is corrected, based on a heat transfer model of the thermocouple, described in Appendix B, using the simulated tube wall temperature distributions surrounding the thermocouples. K-type thermocouples are further used to measure receiver surface temperatures at the center between receiver inlet and outlet at the positions indicated in Figure 6-1a. HTF pressure drop between receiver inlet and outlet is measured with a Sensortechnics BTEM50070D4A differential pressure transmitter (range: $0\div 70$mbar, nonlinearity: $\pm 0.2\%$ FS). Air temperature around the receiver is measured with a Rotronic HC2-S probe (accuracy: ± 0.1K).

6.4 Model Validation

6.4.1 Pressure loss

Measured and simulated pressure drops Δp_{HTF} in the HTF flow between receiver inlet and outlet are compared in Figure 6-7, for m_{HTF} in the range $0.039 \div 0.48$ kg/s. All runs are conducted off sun with $T_{\mathrm{HTF}} = T_{\infty} \cong 10°\mathrm{C}$.
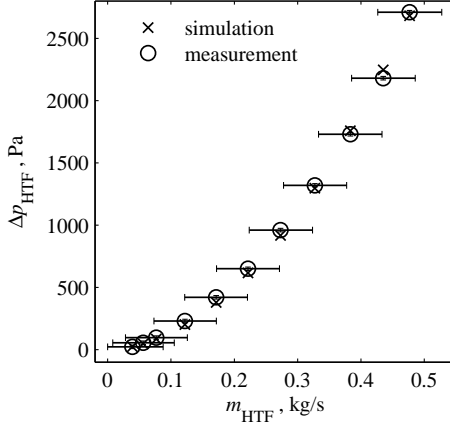
Figure 6-7: Comparison of measured and simulated pressure drops in the HTF flow between receiver inlet and outlet.

6.4.2 Heat loss tests

Defocussed steady-state receiver heat loss tests are performed with the collector in horizontal position (except for case 4 with $\beta_{\text{inclination}} = 19°$), $T_{\text{HTF,in}} = 185 \div 542°C$, and $m_{\text{HTF}} = 0.03 \div 0.23 \,\text{kg/s}$. Steady-state was considered to be reached after a period of 30min within which HTF inlet and outlet temperatures varied by less than 1%. Figure 6-8a compares measured and simulated HTF outlet temperatures. Figure 6-8b shows the ratios of simulated and measured receiver surface temperatures at the measurement locations indicated in Figure 6-1a, for the 14 test cases in Figure 6-8a. The total thermal heat loss rate from the receiver

$$Q_{\text{loss,thermal}} = m_{\text{HTF}} \int_{T_{\text{HTF,in}}}^{T_{\text{HTF,out}}} c_{p,\text{HTF}} \left(T_{\text{HTF}} \right) dT_{\text{HTF}} \tag{6.14}$$
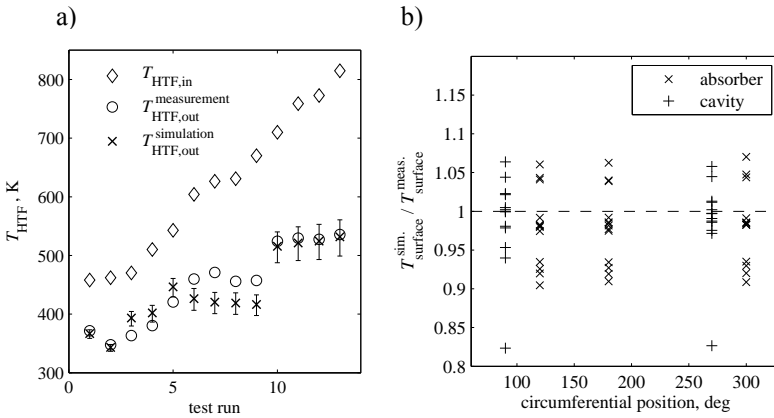
is plotted in Figure 6-9.

Figure 6-8: Receiver heat transfer model validation via defocussed receiver heat loss tests: a) measured HTF inlet and outlet temperatures, and simulated HTF outlet temperatures; rms-difference of $\Delta T_{\mathrm{HTF}} = T_{\mathrm{HTF,in}} - T_{\mathrm{HTF,out}}$ between simulations and measurements is 18.8%; b) ratios of simulated to measured receiver surface temperatures for the 14 heat loss tests shown in a), at the 5 measurement locations indicated in Figure 6-1a; x-axis: circumferential position of measurement location, clockwise, 0° corresponding to $-z$-direction; rms-difference is 5.5%.
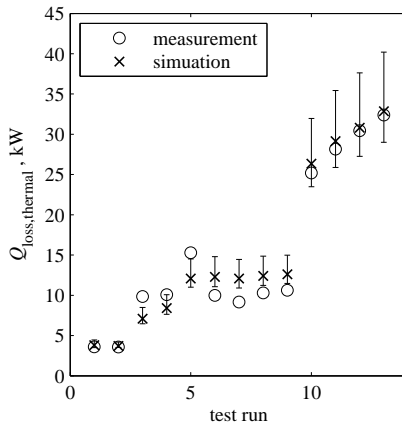

Figure 6-9: Receiver heat transfer model validation via defocussed receiver heat loss tests: thermal heat losses from the receiver; overall rms-difference between measurements and simulations is 19%.

6.4.3 On-sun tests

The measurement and simulation results of a transient on-sun receiver test are plotted in Figure 6-10. Simulation time step is 800s, the MC simulation is repeated every 1600s with 5E6 rays.
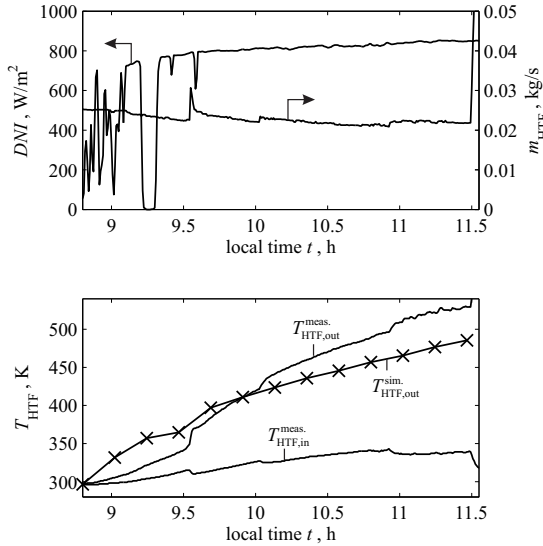

Figure 6-10: On-sun receiver test results with focused concentrator: a) measured direct normal solar irradiance and mass flow rate (calculated from the measured air velocity) that are input to the simulation; b) measured HTF temperatures at receiver inlet and outlet, and simulated HTF outlet temperature.

6.5 Performance Predictions

The steady-state prototype receiver performance is predicted with the validated heat transfer model. HTF inlet temperature is kept constant at $T_{HTF,in} = 120°C$ in all cases. Figure 6-11 and Figure 6-12 show the receiver absorption efficiency, the pressure drop in the HTF flow through the receiver, and the isentropic HTF pumping power requirement, at the days spring equinox and summer solstice, for HTF mass flow rate varying in the range $m_{HTF} = 0.1 \div 1 \, kg/s$. Time dependent parameters are listed in Table

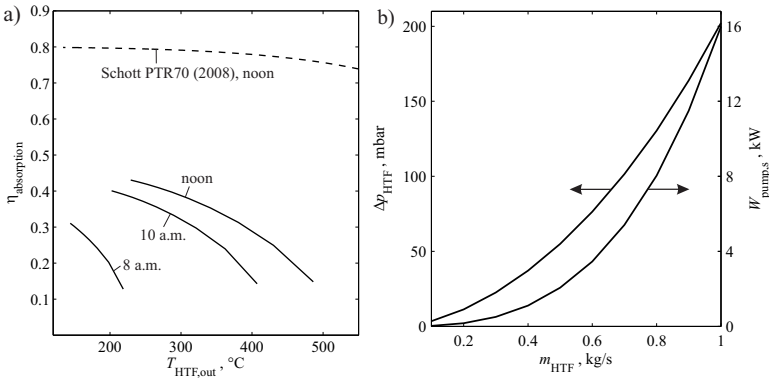6-7. For comparison, absorption efficiency predictions for the Schott PTR70 (2008) receiver are shown. [40]

Figure 6-11: a) Absorption efficiency of the prototype receiver at spring equinox, determined with the validated heat transfer model; curve parameter is the solar time; time-dependent parameters are given in Table 6-7; for comparison the absorption efficiency of the Schott PTR70 (2008) receiver at solar noon is shown; b) pressure drop inside the receiver and isentropic HTF pumping power requirement at solar noon.
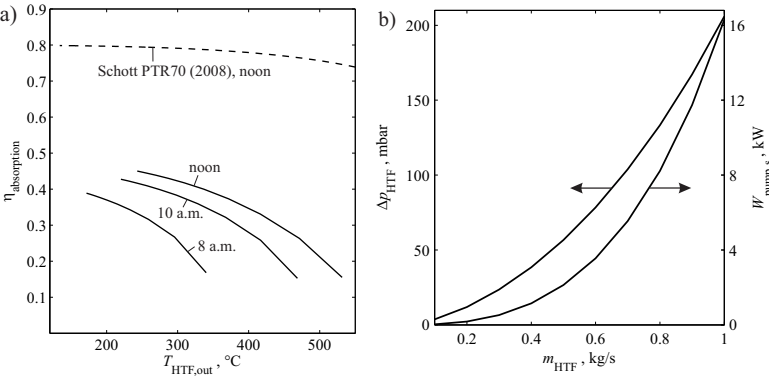

Figure 6-12: Absorption efficiency of the prototype receiver at summer solstice, determined with the validated heat transfer model; curve parameter is the solar time; time-dependent parameters are given in Table 6-7; for comparison the absorption efficiency of the Schott PTR70 (2008) receiver at solar noon is shown; b) pressure drop inside the receiver and isentropic HTF pumping power requirement at solar noon.

98

	spring equinox			summer solstice		
	8 a.m.	10 a.m.	noon	8 a.m.	10 a.m.	noon
DNI , $\left[W/m^2 \right]$	557	755	801	739	839	865
solar incidence angle, $\left[deg \right]$	60	30	0	52.6	27.3	0
concentrator tilt, $\left[deg \right]$	47.2	46.8	46.8	5.4	19.8	22.9

Table 6-7: Simulation parameters that are functions of date and solar time; DNI is estimated with [51].

Figure 6-13 and Figure 6-14 show the different types of heat losses by the receiver as functions of the HTF outlet temperature $T_{\text{HTF,out}}$ in the range 250÷450°C, and the associated HTF pumping power requirement (which varies due to the varying m_{HTF}).

Radiation spillage is due to mismatching receiver and concentrator lengths (3.9% of Q_{solar}), solar radiation absorbed by the CPCs (6.2%), rejected radiation due to mismatching CPC exit area and receiver aperture area (6.1%), and partial shading of the receiver aperture by the CPC mounting (4.2%). Reflection losses (11.7%) are due to radiation that enters the receiver, undergoes multiple reflections at surfaces 2 and 3, and leaves through the aperture. Convective heat losses consist of comparable contributions by surfaces 2/3 and 4, respectively, while reradiation losses predominantly occur at surfaces 2 and 3. Lower total heat losses occur at summer solstice than at spring equinox, due to the lower convective heat losses from surfaces 2 and 3 at the lower concentrator tilt angle.
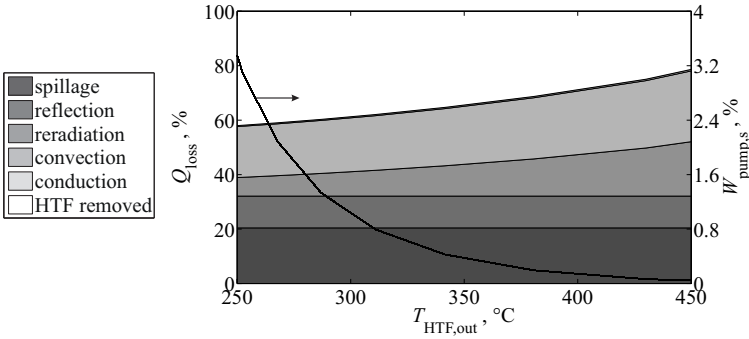
Figure 6-13: Heat losses by the prototype receiver (gray areas), and energy gain by the HTF (white area) as functions of the HTF outlet temperature, for spring equinox, solar noon; all values are normalized by the solar power incident from the primary concentrator, Q_{solar}; conductive losses are <1%; black line: HTF pumping power requirement.
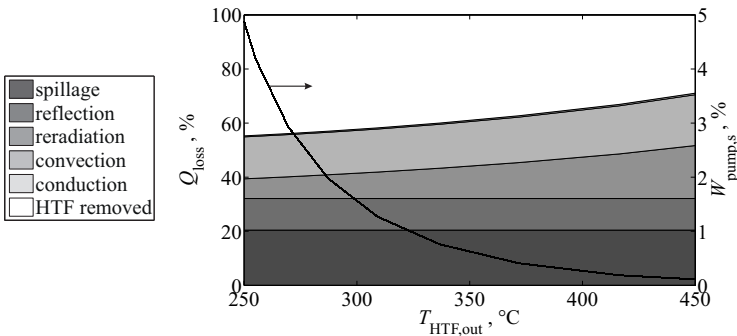

Figure 6-14: Heat losses by the prototype receiver (gray areas), and energy gain by the HTF (white area) as functions of the HTF outlet temperature, for summer solstice, solar noon; all values are normalized by the solar power incident from the primary concentrator, Q_{solar}; conductive losses are <1%; black line: HTF pumping power requirement.

6.6 Conclusions

A 42m-long full-scale prototype of an air-based cylindrical cavity-receiver for parabolic trough collectors has been built and tested. A heat transfer model of the prototype receiver has been established and validated by comparing simulated and measured HTF and receiver temperatures, and HTF pressure drops. Performance predictions for this generic prototype receiver design have been determined with the validated receiver model. For constant receiver inlet temperture $T_{\text{HTF,in}}$ =120°, and $T_{\text{HTF,out}}$ in the range $250 \div 450°C$, the predicted energy losses from the receiver, the heat gain by the HTF, and the receiver's absorption efficiency are summarized in Table 6-8.

	spring equinox, solar noon	summer solstice, solar noon
$Q_{\text{loss,spillage}}$, [%]	20.4	20.4
$Q_{\text{loss,reflection}}$, [%]	11.7	11.7
$Q_{\text{loss,reradiation}}$, [%]	$6.8 \div 20.0$	$7.3 \div 19.6$
$Q_{\text{loss,convection}}$, [%]	$18.7 \div 26.0$	$15.5 \div 18.8$
$Q_{\text{loss,conduction}}$, [%]	$0.3 \div 0.6$	$0.4 \div 0.6$
Q_{HTF} , [%]	$42.0 \div 21.4$	$44.7 \div 29.0$
$\eta_{\text{absorption}}$	$0.420 \div 0.214$	$0.447 \div 0.290$

Table 6-8. Ranges of variation of the heat losses by the receiver, the energy gain by the HTF, and the receiver absorption efficiency, as the HTF outlet temperature $T_{\text{HTF,out}}$ varies from 250 to 450°C (due to changing HTF mass flow rate); $T_{\text{HTF,in}}$ =120°C; Q_{loss} and Q_{HTF} are in % of the solar radiation reflected by the primary concentrator, Q_{solar} .

7 Summary and Outlook

Solar trough collectors, based on pneumatic membrane structures on rotatable concrete frames, have been designed, built, modeled, and tested. Based on the parametric studies of chapters 2 and 3, the concept is expected to be feasible from a technical point of view, given that:

i)   mirror membranes are manufactured with accuracy of ±1mm

ii) mirror membrane clamping point positions deviate by at most ±1mm

iii) mirror membrane pressures deviate by at most ±1Pa from the nominal pressures during concentrator operation

iv) temperature and humidity inside the concentrator air tube deviate by at most ±10°C and ±10% relative humidity from their design values

v)   the mirror membrane inflation pressures are actively controlled and readjusted during operation, to correct for temperature and humidity variations inside the air tube, and deformations of the support structure.

The proposed receiver concept has been successfully demonstrated with the prototype. As expected, the absorption efficiency of the generic prototype receiver design has not reached the level of state-of-the-art receivers yet. Based on the insights obtained from the results in chapters 5 and 6, significantly improved efficiency is expected with the modified cavity-receiver design shown in Figure 7-1. The absorber tube is omitted and the cavity serves as absorber and air duct. The reduced cavity diameter allows for increased insulation thickness, thus minimizing reradiation and convection losses from the insulation surface. The corrugated duct wall improves the convective heat transfer to the HTF. A low-emissivity spectral absorber surface creates high directional apparent absorptivity for incident radiation (due to multiple reflections in the corrugations), at low apparent emissivity (due to the low emissivity of the surface), thus reducing reflection and reradiation losses at the cavity inner walls. A double-glazed

aperture window with heat mirror coating on the inner surface of the outer window and antireflective coatings on the outer surfaces of both windows will minimize reradiative and convective heat losses from the aperture, at acceptably low reflection losses of incoming solar radiation.
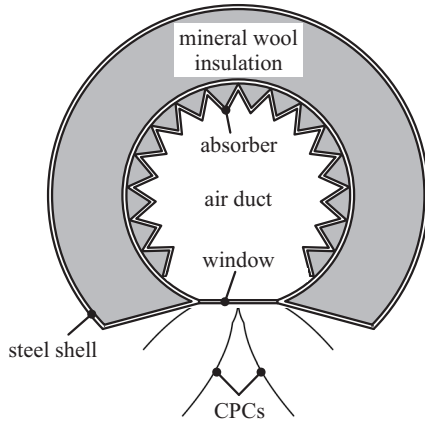

Figure 7-1: Enhanced receiver design with corrugated specular low-emissivity absorber surface and double-glazed aperture window with heat mirror and antireflective coatings; improved insulation.

Appendix A Derivation of Radiosity Equation

The following derivation of Eq. (5.27) follows the lines described in [15], chapter 18.3. Rather than assuming the window to be gray, here separate values for the window's absorptance and emittance are used. The window absorptance A_b (as well as the window transmittance and reflectance) is calculated for the average temperature of the surfaces surrounding the window (inside the enclosure), while the window emittance E_m is calculated at the (local) window temperature. All aforementioned properties are calculated with Eq. (5.29). Radiation incident onto the window is assumed to be diffuse.

Figure A.1 depicts an enclosure consisting of N partially transparent surface segments with segment transmittance $T_{r,i}$, $i = 1, 2, ..., N$, in the range $(0,1)$ (0: opaque segment, 1: fully transparent segment). Defining q_k as the net energy supplied to segment k by other means than thermal radiation, the overall energy balance for segment k reads:

$$q_k = q_{o,k} - q_{i,k} + q_{1,k} \qquad (A.1)$$

where:

$$q_{1,k} = T_{r,k} q_{i,k} \qquad (A.2)$$

is the radiative flux leaving the enclosure through segment k. $q_{i,k}$ and $q_{o,k}$ are incoming and outgoing radiative fluxes at the inner surface of segment k.
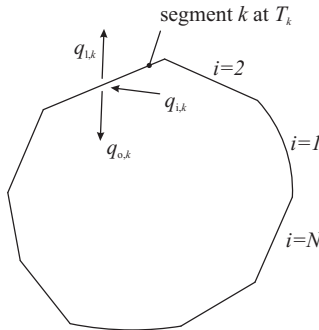

Figure A.1: Enclosure with partially transparent window.

No externally incident radiative fluxes are considered. Radiation emitted at the outer surface of a transparent segment k towards the environment is treated separately. Combining (A.1) and (A.2):

$$q_k = q_{o,k} + (T_{r,k} - 1) q_{i,k} \tag{A.3}$$

Radiation leaving at the inner surface of segment k consists of emitted and reflected incoming radiation:

$$q_{o,k} = E_{m,k} \sigma T_k^4 + R_{e,k} q_{i,k} \tag{A.4}$$

Solving for $q_{i,k}$ yields:

$$q_{i,k} = \frac{1}{R_{e,k}} \left(q_{o,k} - E_{m,k} \sigma T_k^4 \right) \tag{A.5}$$

Combining Eqs. (A.3) and (A.5) yields:

$$q_k = q_{o,k} + (T_{r,k} - 1) \frac{1}{R_{e,k}} \left(q_{o,k} - E_{m,k} \sigma T_k^4 \right) \tag{A.6}$$

Solving (A.6) for $q_{o,k}$, and using $A_b + R_e + T_r = 1$, yields:

$$q_{o,k} = -\frac{R_{e,k}}{A_{b,k}} \left(q_k + (T_{r,k} - 1) \frac{E_{m,k}}{R_{e,k}} \sigma T_k^4 \right) \tag{A.7}$$

or in terms of index i:

$$q_{o,i} = -\frac{R_{e,i}}{A_{b,i}} \left(q_i + (T_{r,i} - 1) \frac{E_{m,i}}{R_{e,i}} \sigma T_i^4 \right) \tag{A.8}$$

$q_{i,k}$ can also be written in terms of outgoing fluxes at surface segments i, $i = 1, 2, ..., N$, and configuration factors from segments k to segment i, F_{k-i} (applying configuration factor reciprocity):

$$q_{i,k} = \sum_{i=1}^{N} F_{k-i} \, q_{o,i} \tag{A.9}$$

Combining Eqs. (A.3) and (A.9) yields:

$$q_k = q_{o,k} + (T_{r,k} - 1) \sum_{i=1}^{N} \left[F_{k-i} \, q_{o,i} \right] \tag{A.10}$$

Including $q_{o,k}$ into the summation yields:

$$q_k = \left(T_{r,k} - 1\right) \sum_{i=1}^{N} \left[F_{k-i} \left(q_{o,i} + \frac{q_{o,k}}{\left(T_{r,k} - 1\right)} \right) \right] \qquad \text{(A.11)}$$

Inserting Eqs. (A.7) and (A.8) into Eq. (A.11), and rearranging yields (Eq. (A.12) to Eq. (A.15) are a sequence of algebraic transformations):

$$\frac{q_k}{T_{r,k} - 1} + \sum_{i=1}^{N} F_{k-i} \frac{R_{e,i}}{A_{b,i}} q_i + \sum_{i=1}^{N} F_{k-i} \frac{R_{e,k}}{\left(T_{r,k} - 1\right) A_{b,k}} q_k$$
$$= -\sum_{i=1}^{N} F_{k-i} \frac{E_{m,i} \left(T_{r,i} - 1\right)}{A_{b,i}} \sigma T_i^4 - \sum_{i=1}^{N} F_{k-i} \frac{E_{m,k}}{A_{b,k}} \sigma T_k^4 \qquad \text{(A.12)}$$

$$-\frac{q_k}{A_{b,k}} + \sum_{i=1}^{N} F_{k-i} \frac{R_{e,i}}{A_{b,i}} q_i = -\sum_{i=1}^{N} F_{k-i} \frac{E_{m,i} \left(T_{r,i} - 1\right)}{A_{b,i}} \sigma T_i^4 - \sum_{i=1}^{N} F_{k-i} \frac{E_{m,k}}{A_{b,k}} \sigma T_k^4 \qquad \text{(A.13)}$$

$$\sum_{i=1}^{N} \left[\delta_{ki} \frac{q_i}{A_{b,i}} - F_{k-i} \frac{R_{e,i}}{A_{b,i}} q_i \right] = \sum_{i=1}^{N} \left[F_{k-i} \frac{E_{m,i} \left(T_{r,i} - 1\right)}{A_{b,i}} \sigma T_i^4 + \delta_{ki} \frac{E_{m,i}}{A_{b,i}} \sigma T_i^4 \right] \qquad \text{(A.14)}$$

$$\sum_{i=1}^{N} \left(\delta_{ki} - F_{k-i} R_{e,i}\right) \frac{q_i}{A_{b,i}} = \sum_{i=1}^{N} \left(F_{k-i} \left(T_{r,i} - 1\right) + \delta_{ki}\right) \frac{E_{m,i}}{A_{b,i}} \sigma T_i^4 \qquad \text{(A.15)}$$

with:

$$\delta_{ki} = \begin{cases} 1, \text{ if } k = i \\ 0 \text{ otherwise} \end{cases} \qquad \text{(A.16)}$$

Eq. (A.15) describes a set of N simultaneous equations, which can be solved for vector q_i.

In the situation of Figure 5-1, radiation losses from surfaces 2 and 3 to the environment can be calculated from:

$$Q'_{\text{rerad},2+3} = \Delta w_\text{w} \sum_{i_\text{w}=1}^{m_\text{w}} \left[T_{r,i_\text{w}} q_{1,i_\text{w}} \right] \qquad \text{(A.17)}$$

where Δw_w denotes the window CV width, $\Delta w_\text{w} = w_{\text{aperture}} / m_\text{w}$, T_{r,i_w} is the transmittance of window CV i_w, $i_\text{w} = 1, 2, ..., m_\text{w}$, and m_w is the number of window CVs. Radiative flux incident onto window segment i_w from within the enclosure, q_{1,i_w}, is found from:

$$q_{i_w} = q_{o,i_w} - q_{i,i_w} + q_{1,i_w} = E_{m,i_w} \sigma T_{i_w}^4 + R_{e,i_w} q_{i,i_w} - q_{i,i_w} + T_{r,i_w} q_{i,i_w}$$

$$= E_{m,i_w} \sigma T_{i_w}^4 + q_{i,i_w} \left(R_{e,i_w} + T_{r,i_w} - 1 \right) = E_{m,i_w} \sigma T_{i_w}^4 - A_{b,i_w} q_{i,i_w} \qquad \text{(A.18)}$$

where q_{i_w} is the net energy flux provided to segment i_w by other means than radiation, and A_{b,i_w}, E_{m,i_w}, R_{e,i_w} and T_{r,i_w} denote window segment absorptance, emittance, reflectance, and transmittance. A_{b,i_w} and E_{m,i_w} are evaluated for blackbody radiation at the average cavity temperature, and local window segment temperature, respectively; therefore, $A_{b,i_w} \neq E_{m,i_w}$. Solving (A.18) for q_{i,i_w} and substituting the result into (A.17) yields the energy loss by radiation from surfaces 2 and 3 to the environment:

$$Q'_{\text{rerad},2+3} = \Delta w_w \sum_{i_w=1}^{m_w} \frac{T_{r,i_w}}{A_{b,i_w}} \left(E_{m,i_w} \sigma T_{i_w}^4 - q_{i_w} \right) \qquad \text{(A.19)}$$

Appendix B Correction of Air Temperature Measurement

Gas temperature measurements with thermocouples (TC) in highly radiative environments (e.g. hot tube wall, cold gas) require a correction for the radiative heat transfer between TC and surroundings. A heat transfer model is established for the TCs that measure the HTF temperatures inside the absorber tube at the receiver inlet and outlet, to extract the correct gas temperature from the TC measurements. The TCs are installed perpendicularly to the absorber tube axis, as shown in Figure B.1. The sensing wires of the TC are contained in an Inconel Alloy 600 protective mantle, and their junction is in thermal contact with the tip of the mantle. Hence the thermocouple measures the temperature at the tip of the mantle. The mantle temperature is assumed to vary only along x. Mantle dimensions and properties are indicated in Figure B.1 and listed in Table B.1. Indexes 1 and 2 refer to mantle surface and surroundings, respectively.
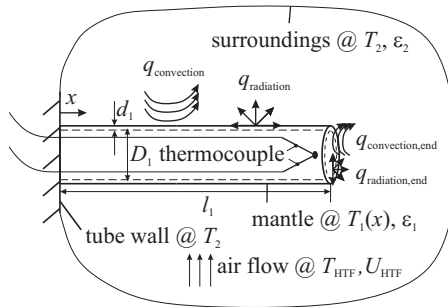

Figure B.1: Thermocouple installed in absorber tube, subject to HTF cross flow and radiative surroundings.

TC mantle outer diameter D_1, $[\text{mm}]$	6
TC mantle wall thickness d_1, $[\text{mm}]$	0.5
length of TC mantle l_1, $[\text{mm}]$	100
emissivity surface 1 ε_1	0.2
emissivity surroundings ε_2	0.8
thermal conductivity of mantle, $\left[\text{W}/(\text{m}\cdot\text{K})\right]$ [52]	14.9

Table B.1: Properties of thermocouple (TC, index 1) and surroundings (index 2).

1D energy balance of an axial control volume of the thermocouple, extending from x to $x + \Delta x$, reads:

$$\pi D_1 d_1 \Delta q_{\text{conduction}} + P \Delta x q_{\text{surface}} = 0 \tag{B.1}$$

where:

$$\Delta q_{\text{conduction}} = k\left(\frac{dT}{dx}(x) - \frac{dT}{dx}(x + \Delta x)\right) \tag{B.2}$$

and q_{surface} is the heat flux over the outer mantle surface by combined convection and radiation. Since $A_2/A_1 \gg 1$, $q_{\text{radiation}} \cong \varepsilon_1 \sigma\left(T_1^4 - T_2^4\right)$. For a cylinder in an air cross flow: [53]

$$\overline{Nu_D} = \frac{\overline{h}D}{k} = C\,Re_D^m\,Pr^n\left(\frac{Pr}{Pr_{\text{surface}}}\right)^{1/4} \tag{B.3}$$

where $D = D_1$, $C = 0.26$, and $m = 0.6$, valid within $1E3 \le Re_D = UD/v \le 2E5$. All air properties are evaluated at T_{air}, except for Pr_{surface} evaluated at the surface temperature. At the tip of the mantle:

$$\overline{Nu_L} = \frac{\overline{h}L}{k} = 0.664\,Re_L^{1/2}\,Pr^{1/3} \tag{B.4}$$

where $L = D_1$, valid for $Re_L = UL/v \le 1E5$ and air properties are evaluated at the film temperature.

The TC is divided into 100 axial segments, and Eq. (B.1) is solved iteratively to determine $T_1(x)$ and T_{air}, applying the boundary conditions

$T_1(x=0) = T_2$ and $T_1(x=l_1) = T_{TC}$. Wall temperature T_2 is known either from measurements, or from the receiver simulation, and T_{TC} is the temperature reading of the thermocouple. Figure B.2 shows the error of the measured air temperature, $T_{TC} - T_{air}$, as a function of the temperature difference between surroundings (2) and TC, $T_2 - T_{TC}$. In all cases shown, air velocity $U_{air} = 10$ m/s, and parameters in Table B.1 apply.
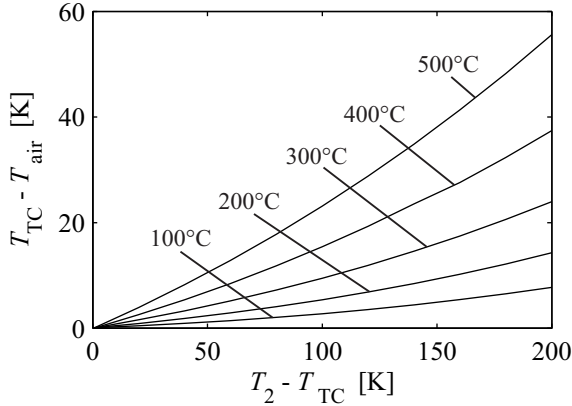

Figure B.2: Calculated difference between measured and actual air temperature, $T_{TC} - T_{air}$, as a function of the temperature difference between surroundings and TC, $T_2 - T_{TC}$; curve parameter is the measured temperature T_{TC}.

Appendix C Air Properties

Dry air consists of a mixture of N_2 (mole fraction: 78.08%), O_2 (20.95%), Ar (0.93%), CO_2 (0.03%), and Neon, Helium, Methane and others (0.01%). [54] Molecular weight of air is 28.96 g/mol. [36] Air is assumed to be an ideal gas throughout the present work, i.e.:

$$\frac{pv}{R_{\text{air}}T} = Z = 1 \tag{C.1}$$

where the specific gas constant of air is $R_{\text{air}} = 287.1 \, \text{J}/(\text{kg} \cdot \text{K})$. Air properties at ambient pressure are found in [36] and [55] to [59]. The data are compared in Figure C.1a-d. The data given by [36] are used in the present work.

Within the considered temperature range, the influence of pressure changes on the air properties is small. c_p changes by <0.2% as the pressure increases from 1bar to 2bar, μ changes by <0.5% as the pressure changes from 1bar to 10bar, and k changes by 5.3% as pressure changes from 1bar to 50bar. Air pressure in the receiver remains around ±0.2bar of ambient pressure. Hence, air properties at 1bar are used in the model. Influence of pressure on density ρ is calculated from Eq. (C.1).

The influence of the (variable) water steam content of the air is taken into account in the calculation of the heat capacity c_p. Measured state variables of the ambient air are total pressure p, temperature T, and relative humidity φ, which is defined as:

$$\varphi = p_{\text{steam}} / p_{\text{steam}}^{\text{sat}}(T) \tag{C.2}$$

where p_{steam} and $p_{\text{steam}}^{\text{sat}}(T)$ are the actual steam partial pressure in air and the saturation partial pressure of steam in air, respectively. The saturation partial pressure of steam is set equal to the vapor pressure of water at the temperature T of the moist air [60], given by [61]:

$$\ln\left(\frac{p_{steam}^{sat}}{p_{critical,water}}\right) = \frac{T_{critical,water}}{T}\left[a_1\tau + a_2\tau^{1.5} + a_3\tau^3 + a_4\tau^{3.5} + a_5\tau^4 + a_6\tau^{7.5}\right]$$

(C.3)

where $p_{critical,water} = 22.064\,\text{MPa}$ and $T_{crititcal,water} = 647.096\,\text{K}$ are the critical pressure and temperature of water, and $\tau = 1 - T/T_{critical,water}$. Parameters a_i are listed in Table C.1.
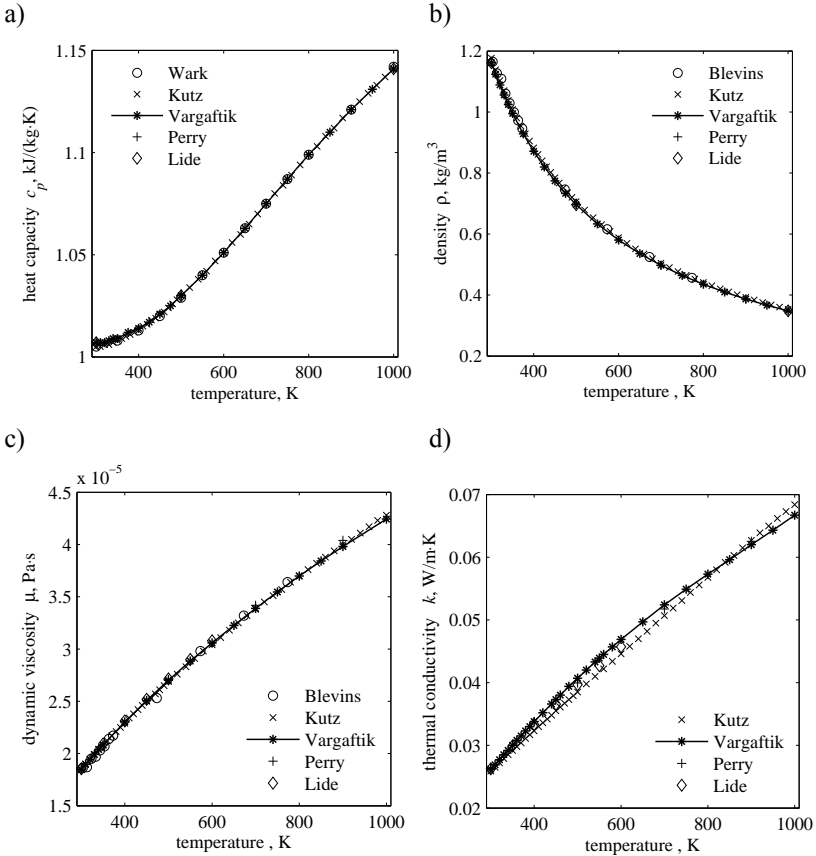
a) b)

c) d)

Figure C.1: Air properties for temperatures in the range 300 to 1000K, at 1bar (or 1atm) pressure.

a_1	-7.85951783
a_2	1.84408259
a_3	-11.7866497
a_4	22.6807411
a_5	-15.9618719
a_6	1.80122502

Table C.1: Coefficients in Eq. (C.3).

The heat capacity of moist air is calculated as the mass-weighted average of the heat capacities of dry air and steam: [54]

$$c_{p,\text{air}}(T) = \frac{(1-x_{\text{steam}})M_{\text{air,dry}}}{(1-x_{\text{steam}})M_{\text{air,dry}} + x_{\text{steam}}M_{\text{H}_2\text{O}}} c_{p,\text{air,dry}}(T) \dots$$

$$+ \frac{x_{\text{steam}}M_{\text{H}_2\text{O}}}{(1-x_{\text{steam}})M_{\text{air,dry}} + x_{\text{steam}}M_{\text{H}_2\text{O}}} c_{p,\text{steam}}(T) \tag{C.4}$$

with $c_{p,\text{steam}}(T)$ from [62].

Appendix D Top Mirror Membrane Temperature

While the support membranes are assumed to be in thermal equilibrium with the surrounding air at T_{ambient}, the aluminized top mirror membrane is in radiative exchange with the sun and the sky, and therefore $T_{\text{membrane,1}} \neq T_{\text{ambient}}$. A 2D steady-state energy balance for the top membrane is established to estimate the temperature difference between the top membrane and the air surrounding it. The following assumptions are made: concentrator in horizontal position, flat (instead of curved) top mirror membrane (approximated with regression line), uniform membrane temperature, no heat conduction between membrane and clamping, membrane emissivity $\varepsilon_{\text{membrane,1}} = 1 - \rho_{\text{mirror}} = 0.08$, apparent sky temperature $T_{\text{sky}} = 275\text{K}$, solar irradiance $I_{\text{sun}} = 800\,\text{W}/\text{m}^2$, solar incidence angle $\theta_{\text{skew}} = 30°$, ETFE-membrane transmittance equal to 1. The energy balance for the top mirror membrane reads:

$$Q_{\text{sky,absorbed}} + Q_{\text{solar,absorbed}} + Q_{\text{convection,upper}} + Q_{\text{convection,lower}} \cdots$$
$$-Q_{\text{emitted,upper}} - Q_{\text{emitted,lower}} + Q_{\text{absorbed,down}} = 0 \tag{D.1}$$

where $Q_{\text{sky,absorbed}}$ is the absorbed sky radiation, $Q_{\text{solar,absorbed}}$ is the absorbed direct solar radiation, $Q_{\text{convection,upper}}$ and $Q_{\text{convection,lower}}$ are the convective heat transfer between membrane and surrounding air, $Q_{\text{emitted,upper}}$ and $Q_{\text{emitted,lower}}$ are the radiative energy emitted by the membrane, and $Q_{\text{inc,down,absorbed}}$ is the radiative energy emitted by the surrounding and absorbed by the top membrane's lower surface. Inserting the expression for each contribution yields:

$$A_{\text{mirror}} \Big[\varepsilon_{\text{membrane,1}} \left(\sigma T_{\text{sky}}^4 + I_{\text{sun}} \cos\theta_{\text{skew}} - 2\sigma T_{\text{membrane,1}}^4 + \sigma T_{\text{ambient}}^4 \right) \cdots$$
$$- \left(h_{\text{membrane,1,upper}} + h_{\text{membrane,1,lower}} \right)\left(T_{\text{membrane,1}} - T_{\text{ambient}} \right) \Big] \tag{D.2}$$

where $A_{\text{mirror}} = 4.8\,\text{m}^2/\text{m}$ is the membrane surface area, and $h_{\text{membrane,1,upper}}$ and $h_{\text{membrane,1,lower}}$ are the convective heat transfer coefficients at the upper and lower membrane surfaces, given by [63]. Eq. (D.2) is solved iteratively for $T_{\text{membrane,1}}$. For T_{ambient} in the range of 273K÷333K the temperature

difference between top membrane and surrounding air, $T_{\mathrm{membrane},1} - T_{\mathrm{ambient}}$ is plotted in Figure D.1.
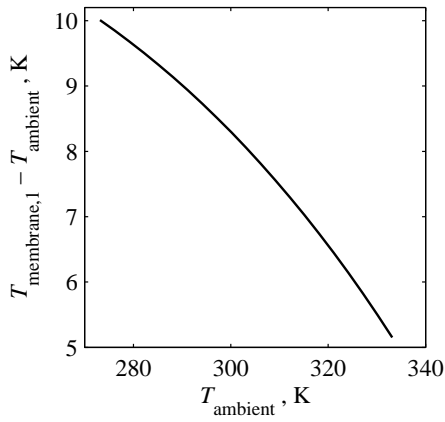

Figure D.1: Difference between top membrane temperature $T_{\mathrm{membrane},1}$ and surrounding air temperature T_{ambient}, as a function of T_{ambient}.

Bibliography

[1]   www.nrel.gov, last checked April 7, 2011.

[2]   www.schott.com, last checked May 5, 2011.

[3]   www.solarpaces.org, last checked May 5, 2011.

[4]   Richter C., Blanco J., Heller P., Mehos M., Meier A., Meyer R., *Solarpaces Annual Report*, 2009.

[5]   Bean J.R., Diver R.B., "Technical Status of the Dish/Stirling Joint Venture Program", IECEC paper no. 95-202, 1995.

[6]   Alpert D.J., Houser R.M., Heckes A.A., Erdman W.W., "The Development of Stretched-Membrane Heliostats in the United-States", *Solar Energy Materials*, Vol. 21, pp. 131-150, 1990.

[7]   www.heliovis.com, last checked April 7, 2011.

[8]   Davenport R., Taylor R., "Low Cost Glass-Reinforced Concrete Heliostats", *Proc. Solarpaces int. conference*, Berlin, 2009.

[9]   Hänchen M., Brückner S., Steinfeld A., "High-Temperature Thermal Storage using a Packed Bed of Rocks - Heat Transfer Analysis and Experimental Validation", *Applied Thermal Engineering*, Vol. 31, pp. 1798-1806, 2011.

[10]   Boyd D.A., Gajewski R., Swift R., "A Cylindrical Blackbody Solar Energy Receiver", *Solar Energy*, Vol. 18, pp. 395-401, 1976.

[11]   Melchior T., Steinfeld A., "Radiative Transfer within a Cylindrical Cavity with Diffusely/Specularly Reflecting Inner Walls Containing an Array of Tubular Absorbers", *ASME J. Solar Energy Engineering*, Vol. 130, pp. 021013, 2008.

[12]   Melchior T., Perkins C., Weimer A.W., Steinfeld A., "A Cavity-Receiver Containing a Tubular Absorber for High-Temperature Thermochemical Processing Using Concentrated Solar Energy, *Int. J. Thermal Sciences*, Vol. 47, pp. 1496-1503, 2008.

[13]   Barra O.A., Franceschi L., "The Parabolic Trough Plants Using Black Body Receivers: Experimental and Theoretical Analyses", *Solar Energy*, Vol. 28, pp. 163-171, 1982.

[14]   Duffie J.A. and Beckman W.A., *Solar Engineering of Thermal Processes*, 3rd ed., John Wiley & Sons, New York, 2006.

[15]   Siegel R. and Howell J.R., *Thermal radiation heat transfer*, 4th ed., Hemisphere Publishing Corp., New York, 2002.

[16]   Johnston G., "On the Analysis of Surface Error Distributions on Concentrated Solar Collectors", *ASME J. Solar Energy Engineering*, Vol. 117, pp. 294-296, 1995.

[17]   Rabl A., Bendt P., Gaul H.W., "Optimization of Parabolic Trough Solar Concentrators", *Solar Energy*, Vol. 29, pp. 407-417, 1982.

[18]   Rabl A., *Active Solar Collectors and Their Applications*, Oxford University Press, New York, 1985.

[19]   ASTM 173-03 reference solar spectrum, http://rredc.nrel.gov/solar/spectra/am1.5/, last checked April 13, 2011.

[20]   D'Errico J., "Bound Constrained Optimization Using fminsearch", http://www.mathworks.com/matlabcentral/fileexchange/8277-fminsearchbnd, MATLAB Central File Exchange, retrieved January 12, 2010.

[21]   DuPont Teijin Films, Mylar Polyester Film Physical-Thermal Properties, Hopewell, VA, 2003.

[22]   Buie D., Monger A.G., Dey C.J., "Sunshape Distributions for Terrestrial Solar Simulations", *Solar Energy*, Vol. 74, pp. 113-122, 2003.

[23]   Winston R., Miñano J.C., Benítez P., *Nonimaging Optics*, Elsevier Academic Press, Amsterdam, 2005.

[24]   Benítez P. and Miñano J.C., "Concentrator Optics for Next Generation Photovoltaics", in: *Next Generation Photovoltaics* (Martí A. and Luque A., eds.), Institute of Physics, London, 2003.

[25] Wolfram Research, Inc., Mathematica, Version 6.0, Champaign, IL, 2007.

[26] MATLAB, Version 7.10.0, The MathWorks Inc., Natick, MA, 2010.

[27] Feuermann D., Gordon J.M., "High-Concentration Photovoltaic Designs based on Miniature Parabolic Dishes", Proc. SPIE, Vol. 4446, pp. 43-51, 2002.

[28] Jenkins D.G., "High-Uniformity Solar Concentrators for Photovoltaics Systems", Proc. SPIE, Vol. 4446, pp. 80-87, 2002.

[29] O'Gallagher J.J., Winston R., "Nonimaging Solar Concentrator with Near Uniform Irradiance for Photovoltaic Arrays", Proc. SPIE, Vol. 4446, pp. 52-56, 2002.

[30] Patankar S.V., *Numerical Heat Transfer and Fluid Flow*, Hemisphere Publishing Corp., Washington, 1980.

[31] http://www.trafilix.com/en_pdf/AISI430.pdf, last checked April 13, 2011.

[32] Incropera F.P., and DeWitt D.P., *Fundamentals of Heat and Mass Transfer*, 5th ed., John Wiley & Sons, Inc., Hoboken, NJ, 2002.

[33] Mills K.C., *Recommended Values of Thermophysical Properties for Selected Commercial Alloys*, Woodhead Publishing Ltd, Cambridge, 2002.

[34] Gnielinski V., "New Equations for Heat and Mass-Transfer in Turbulent Pipe and Channel Flow", *Int. Chemical Engineering*, Vol. 16, pp. 359-368, 1976.

[35] Kuehn T.H., and Goldstein R.J., "An Experimental Study of Natural Convection Heat Transfer in Concentric and Eccentric Horizontal Cylindrical Annuli", *J. Heat Transfer*, Vol. 100, pp. 635-640, 1978.

[36] Vargaftik N.B., *Handbook of physical properties of liquids and gases*, 2nd ed., Hemisphere Publishing Corp., Washington, 1975.

[37] Churchill S.W. and Chu H.H.S., "Correlating Equations for Laminar and Turbulent Free Convection from a Horizontal Cylinder, *Int. J. Heat Mass Transfer*, Vol. 18, pp. 1049-1053, 1975.

[38]   Palik E.D., *Handbook of Optical Constants of Solids*, Academic Press, San Diego, 1998.

[39]   Munson B.R., Young D.F., Okiishi T.H., *Fundamentals of Fluid Mechanics*, 2nd ed., John Wiley & Sons, Inc., Hoboken, NJ, 1994.

[40]   Burkholder F., Kutscher C., "Heat Loss Testing of Schott's 2008 PTR70 Parabolic Trough Receiver", Tech. Report NREL/TP-550-45633, 2009.

[41]   Collares-Pereira M., Gordon J.M., Rabl A., Winston R., "High Concentration Two-Stage Optics for Parabolic Trough Solar Collectors with Tubular Absorber and Large Rim Angle", *Solar Energy*, Vol. 47, pp. 457-466, 1991.

[42]   Almeco Tinox, Vega SP198, www.almeco-tinox.com, last checked April 13, 2011.

[43]   ANSYS CFX 12.1, ANSYS, Inc., 2009.

[44]   Design-Expert 7, Stat-Ease, Inc., Minneapolis, MN, 2004.

[45]   Modest M.F., *Radiative Heat Transfer*, 2nd ed., Academic Press, Amsterdam, 2003.

[46]   Berdahl P., Martin M., "Emissivity of Clear Skies", *Solar Energy*, Vol. 32, pp. 663-664, 1984.

[47]   Churchill S.T. and Chu H.S., "Correlating Equations for Laminar and Turbulent Free convection from a Vertical Plate", *Int. J. Heat Mass Transfer*, Vol. 18, pp. 1323-1329, 1975.

[48]   Reichardt H., „Die Grundlagen des turbulenten Waermeueberganges", *Archiv gesamte Waermetechnik*, Vol. 2, pp. 129–142, 1951.

[49]   White F.M., *Fluid Mechanics*, 7th ed., McGraw-Hill, New York, 2011.

[50]   Roache P.J., *Verification and Validation in Computational Science and Engineering*,   Hermosa Publishers, Albuquerque, 1998.

[51] Hottel H.C., "A Simple Model for Estimating the Transmittance of Direct Solar Radiation Through Clear Atmospheres", *Solar Energy*, Vol. 18, pp. 129-134, 1976.

[52] http://www.bibusmetals.ch/produkte/nickel/ni_werkstoffe/600.htm, retrieved December 8, 2010.

[53] Zukauskas A., "Heat Transfer from Tubes in Cross Flow", in: *Advances in Heat Transfer* (Hartnett J.P. and Irvine T.F., Jr., eds.), Vol. 8, Academic Press, New York, 1972 (retrieved from [32]).

[54] Wong G.S.K., Embleton T.F.W., "Variation of Specific Heats and Specific Heat Ratio in Air with Humidity", *J. Acoustical Society America*, Vol. 76, pp. 555-559, 1984.

[55] Wark K., *Thermodynamics*, 4th ed., McGraw-Hill, New Nork, 1983.

[56] Blevins R.D., *Applied Fluid Dynamics Handbook*, Van Nostrand Reinhold Co., Inc., New York, 1984.

[57] Kutz M., *Mechanical Engineers' Handbook - Energy and Power*, 3rd ed., John Wiley & Sons, Inc., Hoboken, NJ, 2006.

[58] Perry R.H., *Perry's Chemical Engineers' Handbook*, 8th ed., McGraw-Hill, New York, 2008.

[59] Lide D.R., Kehiaian H.V., *CRC Handbook of Thermophysical and Thermochemical Data*, CRC Press, Inc., Boca Raton, 1994.

[60] Baehr H.D., *Thermodynamik*, 13th ed., Springer-Verlag, Berlin, 2006.

[61] Wagner W., Pruss A., "International Equations for the Saturation Properties of Ordinary Water Substances. Revised According to the International Temperature Scale of 1990. Addendum to J. Phys. Chem. Ref. Data 16, 893 (1987)", *J. Phys. Chem. Ref. Data*, Vol. 22, pp. 783-787, 1993.

[62] Rowley R.L., Wilding W.V., Oscarson J.L.,Yang Y., Giles N.F., DIPPR® Data Compilation of Pure Chemical Properties, Design Institute for Physical Properties, AIChE, New York, NY, 2010.

[63] Fujii T., Imura H., "Natural-Convection Heat Transfer from a Plate with Arbitrary Inclination", *Int. J. Heat Mass Transfer*, Vol. 15, pp. 755-767, 1972.

Curriculum Vitae

Name: Roman Bader

Nationality: Swiss

Citizen of: Basel (BS)

Date of birth: June 28, 1983

2008-2011   Doctoral studies at the Professorship of Renewable Energy Carriers, ETH Zurich; supervision: Prof. Dr. Aldo Steinfeld

2002-2008   Bachelor and Master studies in Mechanical Engineering at ETH Zurich; focus on renewable energy technologies

2006   Internship at Hilti AG, Schaan, Liechtenstein

2005   Internship at PUC Minas university, Belo Horizonte, Brasil

2002   Maturität, Gymnasium Kirschgarten, Basel

Publications

Bader R., Haueter P., Pedretti A., Steinfeld A., "Optical Design of a Novel Two-Stage Solar Trough Concentrator based on Pneumatic Polymeric Structures", *ASME Journal of Solar Energy Engineering (JSEE)*, Vol. 131, pp. 031007, 2009.

Bader R., Steinfeld A., "A Solar Trough Concentrator for Pill-Box Flux Distribution over a CPV Panel", *JSEE*, Vol. 132, pp. 014501, 2010.

Bader R., Barbato M., Pedretti A., Steinfeld A., "An Air-Based Cavity-Receiver for Solar Trough Concentrators", *JSEE*, Vol. 132, pp. 031017, 2010.

Bader R., Pedretti A., Steinfeld A., "A 9m-Aperture Solar Parabolic Trough Concentrator Based on a Multilayer Polymer Mirror Membrane Mounted on a Concrete Structure", *JSEE*, Vol. 133, pp. 031016, 2011.

Bader R., Pedretti A., Steinfeld A., "Experimental and Numerical Heat Transfer Analysis of an Air-Based Cavity-Receiver for Solar Trough Concentrators", *JSEE*, in press.

Zanganeh G., Bader R., Pedretti A., Pedretti M., Steinfeld A., "Solar Dish Concentrator Based on Ellipsoidal Polyester Membrane Facets", *Solar Energy*, in press.

Conference presentations

Bader R., Haueter P., Pedretti A., Steinfeld A., "Optical Design of a Novel 2-stage Solar Trough Concentrator based on Pneumatic Polymeric Structures", *Solarpaces conference 2009*, Berlin (Germany).

Bader R., Barbato M., Pedretti A., Steinfeld A., "An Air-Based Cavity-Receiver for Solar Trough Concentrators", *ASME Energy Sustainability conference 2010*, Phoenix (AZ).

Bader R., Barbato M., Pedretti A., Steinfeld A., An Air-Based Cavity-Receiver for Solar Trough Concentrators", *Solarpaces conference 2010*, Perpignan (France).

126